THE UNIVERSITY *of* EDINBURGH

Low-Dimensional Models of the Transition to Turbulence

Stuart Thomson

Doctor of Philosophy
The University of Edinburgh
December 2018

ABSTRACT

The transition to turbulence in shear flows such as pressure driven pipe flow or plane Couette flow presents an interesting theoretical problem: how do we understand the existence of chaos when the laminar flow is stable to infinitesimal perturbations? A number of approaches to the problem have been used in recent years and a great deal of progress has been made towards understanding the transition, often utilising low-dimensional models to generate hypotheses.

In the first part of this thesis I study the behaviour of a system of partial differential equations based on the damped Kuramoto-Sivashinsky equation which exhibit a subcritical transition to turbulence as a control parameter is varied. Typical lifetimes of the system are measured and align with the scenario for shear flows; they have an exponential distribution for a given value of the control parameter, and the typical lifetime scale superexponentially with that parameter. Coherent structures are found numerically and the linear stability measured to create a bifurcation diagram which is reminiscent of the ones found in shear flows.

In the second part of the thesis a link is drawn between the apparent dynamical role of the lower branch states of the extended KS equation and the current understanding of transitional turbulence as belonging to the universality class of Directed Percolation (DP). A novel DP model is introduced which has a third state which represents the behaviour of the lower branches and the critical exponents of the system are measured and found to agree with the expected exponents for 1+1 dimensional DP. A non-universal parameter is found which varies with the strength of the bouncing behaviour, although it is unclear if it is possible to measure this parameter in a meaningful way for a real flow.

Finally, in the third part of the thesis the extended KS equation is studied in an extended spatial domain, to confirm the hypothesis that this system also belongs to the DP universality class. Critical exponents are measured and found to agree with 1+1 DP. This confirms that the system has a transition which reproduces many of the important features subcritical fluid flows like pressure driven pipe flow, or plane Couette flow.

DECLARATION

I declare that this thesis was composed by myself, that the work contained herein is my own except where explicitly stated otherwise in the text, and that this work has not been submitted for any other degree or professional qualification except as specified.

(*Stuart Thomson, December 2018*)

ACKNOWLEDGEMENTS

First of all I would like to thank my supervisor Alexander Morozov for the years of advice, guidance, and patience involved in getting here. Thanks also to Martin Evans and Richard Blythe for their support and thoughtful suggestions.

I would also like to thank Roseanne, without whom I would never have managed to do this.

And of course thank you to my parents, for everything.

CONTENTS

LIST OF FIGURES

LIST OF TABLES

1 INTRODUCTION

Chaos & order seem like terms which permit no misunderstanding. As if they could be used to neatly categorise the world into two groups of systems, those that evolve in a noisy, random, and unpredictable way compared to the other group of systems, which behave in a regimented and smooth manner. The truth is more complicated than that, never more so than for a class of hydrodynamic flows, the *parallel shear flows* which allow for the startling coexistence of chaos and order in one system. They are also fascinating for the way they allow us to see the rich structure and beauty hidden within the chaos. Combined with the evident practical applications related to them, these flows present an interesting and rewarding class of problems to study.

I will begin this Thesis with a brief overview of the methods by which transitional turbulence has been understood. First I will give a description of the types of turbulent systems we will be concerned with, and how the linear stability of the laminar flow makes the position (and even existence) of the critical point a vexed question. I will then discuss two different approaches to understanding the transition: as a non-equilibrium statistical transition, and as a bifurcating dynamical system. Finally, I will spend some time discussing the Kuramoto-Sivashinsky equation, which will serve as the basis of a model to be studied in chapter 2.

1.1 SUBCRITICAL TURBULENCE

This Thesis is concerned with modelling the transition from non-turbulent (laminar) to turbulent dynamics in parallel shear flow systems where this transition is *subcritical*. The first study of such a system was undertaken by Reynolds in 1883 [1] by attempting to find what would induce the water flowing through a pipe to behave in an orderly or chaotic manner. In his investigations he used a dimensionless quantity to quantify the flow and this quantity later came to bear his name: the Reynolds number, Re[1]. The Reynolds number characterises the relative importance of inertial

[1] Although popularized by Reynolds the quantity was in fact first introduced by George Stokes, making this a perfect example of Stigler's law of eponymy! [2]

and viscous forces meaning that it in some sense captures the idea of the rate of flow of the fluid and can be used to compare the behaviour different fluids in different settings to find similarities between them, and allow experiments to come to more general conclusions than would otherwise be the case if they could not be compared so directly using Re. In his study, Reynold attempted to find a critical value of the Reynolds number above which turbulent behaviour would occur and below which laminar flow would occur.

As it turned out, there is an important property of the flow in a pipe which makes this question a complex one; namely, that the laminar flow is linearly stable [3, 4]. For pipe flow this is true for arbitrarily high Re, but any flow which exhibits turbulent behaviour at Re with a linearly stable laminar flow is said to be 'subcritical'. Another flow for which we know there is a linearly stable base flow for all Re is plane Couette flow [5], and taken together these two flows are the paradigmatic cases of subcritical turbulence transition. In this introduction I will discuss only these two flows, although it should be noted that there are other systems which appear to belong to this same category, including systems as diverse as magnetohydrodynamics [6, 7], forced isotropic turbulence [8], tokamak turbulence [9], Kolmogorov flow [10] and possibly epileptic seizures [11]. There are even many parallels between subcritical turbulence and the glass transition [12]. These more exotic systems have significantly less research than pressure driven pipe flow and plane Couette flow, so this introduction will concern itself with these two primarily, with the understanding that there could be a large number of systems which have similar behaviour. It's also worth noting that the development of ideas in these two paradigmatic cases is linked but separate, and I will attempt to summarise the findings in each at the same even when they did not occur contemporaneously. It is also not always clear how much can be learned about one system from findings in the other, but I will try to paint a more or less united picture of the flows.

1.1.1 PERTURBATION THRESHOLD

The fact that the laminar flow is stable means that only perturbations large enough to take the system far enough away from the base flow such that the linearisation is invalid (and nonlinear terms can come into play) can make the system exhibit chaotic dynamics. There is the complication that the eigenvalues of the linearised operator can indicate decay even when some growth is possible because of the phenomenon of non-normal growth [13].

So what size of perturbation is sufficient to trigger chaos? We should expect that increasing Re will decrease the required perturbation size and we can characterise

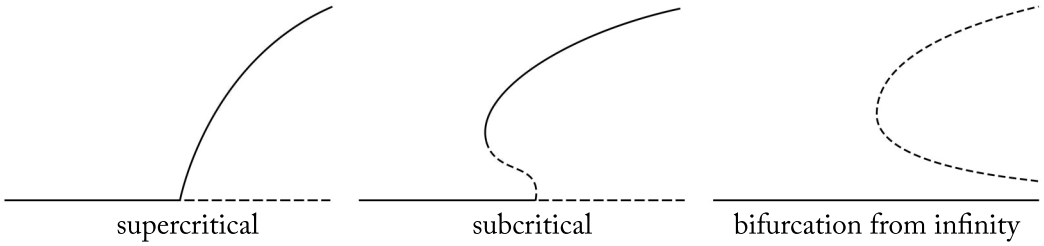

Figure 1.1: Cartoon bifurcation diagrams showing the different kinds of transition scenario. Moving from left to right within a figure represents increasing the control parameter (typically the Reynolds number for a hydrodynamic flow). The horizontal line represents the laminar flow; stable and unstable lines are solid and dashed respectively. On the left is shown a supercritical transition, where a linear instability in the base flow causes an increasing degree of turbulent behaviour from the point of the instability onwards. The diagrams in the middle and on the right both show subcritical transitions, namely there are regions where turbulent and laminar behaviour can coexist. The difference is that in figure **b** the laminar flow becomes unstable at some value of the control parameter whereas figure **c** shows a bifurcation 'from infinity'. The rightmost figure is the closest to the situation we have for pipe flow and plane Couette flow.

the scaling of the amplitude with a simple expression [14]:

$$A_c \sim Re^{\gamma}\,, \tag{1.1}$$

where A_c is the critical perturbation amplitude and γ is a constant. Hof *et al.* conducted experiments in pipe flow using injected fluid to cause the perturbation and found that the scaling has $\gamma = -1$ [15]. This scaling law for injection was replicated by Peixinho & Mullin [16] but they found that different perturbations have different scaling laws, and that push-pull disturbances had a steeper decline, decaying approximately as $Re^{-1.4}$; this finding is in good agreement with numerical simulations [14]. The picture for plane Couette flow does not seem to be currently as clear, although there is an upper bound of $\gamma = -1$ [17] and numerical calculations have found a value of $\gamma = -2.7$ [18]. The decreasing distance between turbulent and laminar regions means that the question of the 'critical point' of the flow is partly a question of which perturbations will trigger turbulence at a given Re [19].

We will return to the question of minimal perturbations later in this chapter once we have an understanding of the flow from the dynamical systems point of view.

1.1.2 FINITE LIFETIMES

Once turbulence has been triggered by one of these sufficient perturbations, what happens next? As it turns out, the turbulence can decay back to the laminar state. As early as 1989 it was suggested by Brosa [20] that turbulent flow in a pipe was always

transient in one of the first numerical investigations of Navier-Stokes turbulence. The lifetimes of turbulent puffs in pipe flow at a given Re has been shown to be exponentially distributed in both numerical simulations [21–24] and experiments [16, 25–28]. The exponential statistics imply that the chance for the puff to decay is a constant in time: a memoryless process. The same process has also been seen in plane Couette flow [29, 30]. The question facing the research community was to find a value of the Reynolds number above which this lifetime would diverge, and thus be the critical point between transient and sustained turbulence.

In 2006, Hof *et al.* published a paper with a radical new proposal - that there is no Reynolds number at which the lifetime of a puff diverges [26]. They came to this conclusion after utilising an experimental setup with a pipe that was very long compared to its diameter, allowing effective observation times which were ten times longer than previous experiments or simulations. The experimental setup made it easier to change the Reynolds number than the observation time and so the measured curves were not probability vs. time for a fixed Re, but probability vs. Re for a fixed observation time. The basic idea is that if there is a critical Re for which lifetimes diverge, we should expect to see a certain profile to these curves but that is not what was observed; the probability of death only approached 1 asymptotically. The authors propose that what they observed was the turbulent lifetimes scaling exponentially with Re although later studies would show that this is not the correct scaling behaviour, due in large part to the still relatively small range of Reynolds numbers tested. Using a similar setup but with some improvements (most notably the ability to more accurately control the temperature of the water, and therefore its viscosity) in 2008 Hof *et al.* increased the observation time and confirmed the transience of turbulence as high as $Re = 2050$, but the scaling obtained was super-exponential. More evidence of this super-exponential scaling has been found in experiments [31] and numerical simulations of pipe flow as well as plane Couette flow [30, 32].

The origin and exact form of the scaling are still open questions, although one solution has been proposed by Goldenfeld *et al.* [33]. The authors argue that if turbulence relaminarises when the largest fluctuation in velocity is below some threshold value, then the probability of this event can be computed using extreme distribution theory, where the relevant distribution is the cumulative Gumbel distribution:

$$F(X) = \exp\{-\exp[-(X-\mu)/\beta]\}\,, \tag{1.2}$$

where $F(X)$ is the probability that the maximum velocity fluctuation is below

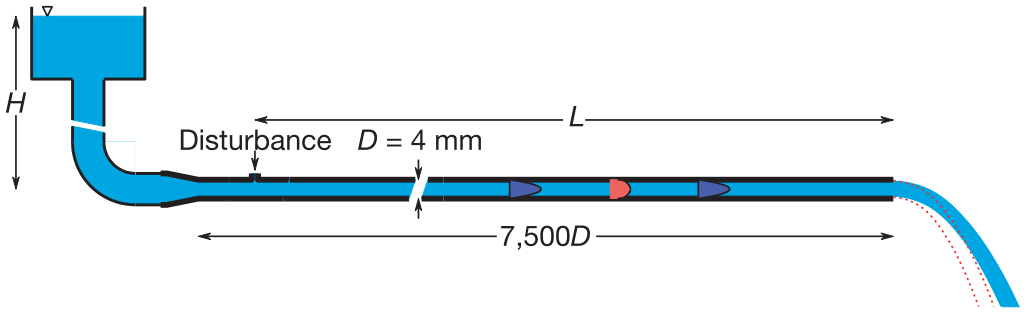

Figure 1.2: A schematic of the apparatus used by Hof *et al.* to measure turbulent lifetimes, reproduced from [26]. The water is driven by a constant pressure head and disturbance were made by injecting fluid into the pipe. Turbulent puffs show up as dips in the exit angle of the fluid and it is therefore possible to measure if the puff has decayed or not.

X, μ is just a variable which sets the centre of the distribution and β scales the distribution. So if X is a minimum threshold amplitude for turbulence then this will give the rate for the system to transition to the laminar state (for a discussion on the difference between transitioning *to* and transitioning *from* turbulence in Couette flows, see [34]). However, as there is no known functional form for the Re dependence of the threshold a Taylor expansion was used and thus the derived scaling of lifetimes with Re is only valid over a small range of Re so we cannot infer from this the scaling of lifetimes at large Re [12]. However, at these larger values of Re, the phenomenon of puff splitting becomes increasingly important, and the lifetime of individual puffs less important, and even less easy to define.

1.1.3 INTERMITTENCY & DIRECTED PERCOLATION

It has been known for quite some time that as well as decaying, turbulent puffs can also split [36–38]. This leads to sections of fluid which are turbulent and sections which are laminar, a phenomenon known as intermittency. This is a route to chaos known from a type of model known as coupled map lattices [39]. Interestingly, one early paper of the spatiotemporal intermittency route to chaos was a study on the damped Kuramoto-Sivashinsky equation (of which more later) [40].

Due to this splitting there is a competition between two processes - puff splitting tends to increase the amount of turbulent fluid whereas the ever present possibility for decay tends to decrease it. This is very reminiscent of a universality class from nonequilibrium statistical physics known as Directed Percolation (DP). This analogy was first noted by Pomeau in 1986 [41] and has more recently gained prominence as a complementary alternative to the dynamical systems approach to understanding

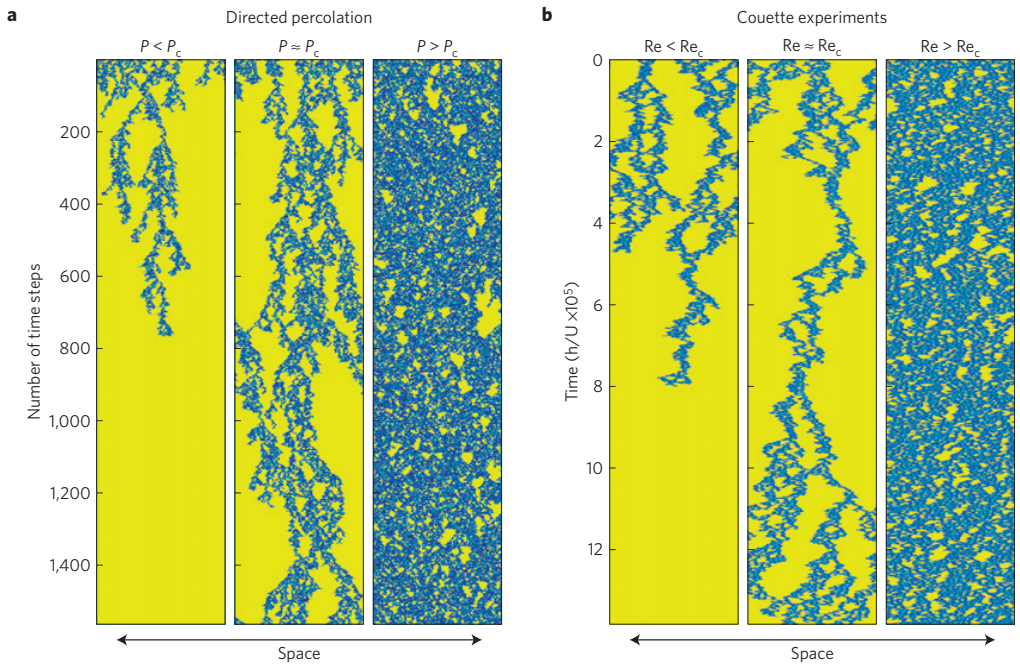

Figure 1.3: The striking similarity between shear flows and Directed Percolation, reproduced from [35]. The critical exponents measured in this experiment showed that (at least some) shear flows belong to the DP universality class.

the transition. Directed Percolation allows a system to experience a transition to sustained turbulence even when the individual elements of the system can always decay; this is one way to settle the question of if and how the subcritical systems transition to a chaotic attractor.

Spatiotemporal intermittency was studied experimentally for pCF in a pair of 1998 papers by Bottin *et al.* and included the first experimentally determined bifurcation diagram for Couette flow [29] and a discussion of the phenomenological similarity between pCF and DP [42]; there was also an early attempt made to simulate pCF with a simplified model and numerically look for DP-type behaviour.

A more hydrodynamically realistic model was later studied by Manneville where it was pointed out that coupled map lattices lack the ability to represent possible long-range interactions due to pressure [43].

An interesting experiment of Prigent & Dauchot has indicated that the intermittency in Couette flow takes a different form depending on from which direction the critical point is passed [34], i.e. if it is a transition *to* turbulence or a transition *from* turbulence.

Directed Percolation has also been proposed as the route to sustained turbulence in pipe flow in [44–46] where experiments on the rate of splitting of puffs found another superexponential scaling; the probability for a puff to split is also

superexponentially dependent on Re. A DP model was studied in [47], where a 3+1 dimensional DP system was studied numerically in pipe geometry. It was also argued that the DP model can account for the superexponential scaling of turbulent lifetimes, again using extreme-value statistics but this time on the length of the longest turbulent cluster.

In 2016 two papers came out measuring the DP critical exponents in two different flow geometries; one of these studies had a 1+1D Taylor-Couette flow [35] and the other studied a 2+1D plane Poiseuille flow [48]. Both of these experiments confirmed that the universal critical exponents are those one would expect from 1+1D and 2+1D DP, respectively (although it has been argued that the study by Sano & Tamai did not have a long enough observation time to allow the flow to equilibriate: see Mukund & Hof [49]). These experiments are a striking confirmation of Pomeau's original hypothesis.

Clear confirmation of the universality class in pipe flow has taken slightly longer to appear, probably due to the complication of the downstream flow of the fluid requiring such long time scales (meaning a long pipe) to equilibriate. A recent experiment of Mukund & Hof proposed a novel method for resolving this difficulty by measuring puffs as they leave the pipe and then reestablishing puff sequence at the head of the pipe, thus creating a kind of artificial periodic boundary condition which allows for arbitrarily long observation times [49]. It is not clear how precisely the recreation of the puffs can be - for example, if there are "nonlocal hydrodynamic effects to due pressure" [43] then it is not clear that these would carry over after the recreation of the puffs. The study has not measured the critical exponents for the flow but it should be possible to do so in the future. A 2010 study by Moxey & Barkley [44] suggests that there are indeed large scale correlations in pipe flow,[2] beginning at $Re \approx 2600$, however, this is also near the point where they propose the flow changes from an intermittent one with DP type behaviour to one of uniform turbulence. Therefore, the method of Mukund & Hof seems to be reasonable provided Re is not increased too far - their study focussed on $Re < 2100$. The critical point for DP was suggested to be near $Re \approx 2040$ by Avila *et al.* [45] which was found to be in agreement with the range suggested by the Mukund & Hof study, namely $2020 < Re_c < 2040$.

As well as pipe flow and Couette flow, recent numerical simulations of a flow similar to plane Couette flow - Waleffe flow - also indicate the presence of a $2+1D$ DP transition [51].

There is an interesting question of what happens to the intermittency as Re is

[2] These types of large scale flows have been seen in plane Couette flow [50].

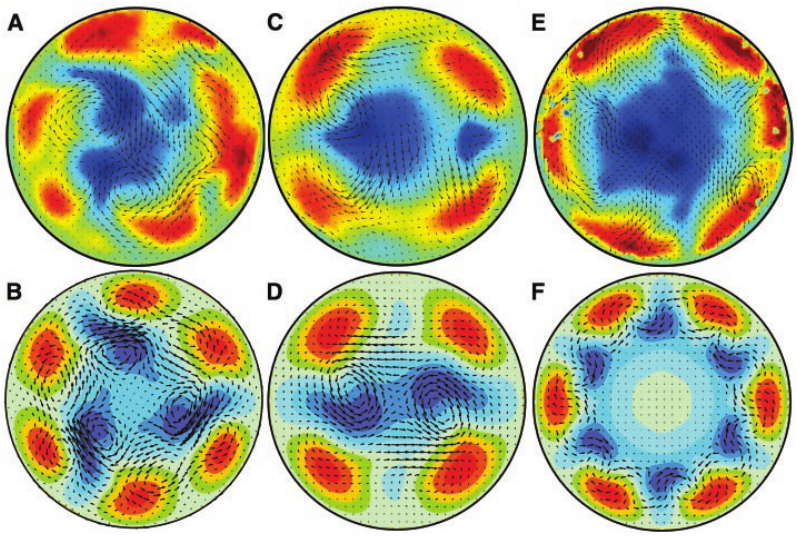

Figure 1.4: Comparison of numerically derived exact coherent structures and experimentally observed flows, reproduced from [56]. The circles are cross sections in a pipe, and the color represents velocity along the pipe (blue is slower, red is faster). The real system passes near the coherent structures but does not land exactly on them because they are linearly unstable.

increased beyond the transitional regime. In a 2013 paper Avila & Hof argue that there is no 'fully turbulent' flow and that intermittency is inherent to shear flows in general. The connection between moderate and high Re turbulence was studied further in [52] although a discussion of the 'fully turbulent flow' is beyond the scope of this thesis, which is concerned primarily with the transitional regime.

1.2 DYNAMICAL SYSTEMS

As well as understanding the transition as a stochastic, non-equilibrium statistical system a great deal of work has gone into understanding the transition as dynamical system [53–55]. The difference is in treating the problem with a more fundamentally deterministic outlook, and given that the Navier-Stokes equations are deterministic, there should be some method of understanding the problem in this way. One of the main features of the transition to receive attention is that of the existence of *coherent structures* in the transitional regime.

1.2.1 EXACT COHERENT STRUCTURES

Coherent Structures are non-laminar solutions to the equations of motion (e.g. the Navier-Stokes equation) which for shear flows often take the form of travelling wave solutions for pipe flow, and steady state solutions in plane Couette flow [57]; importantly, they also can take the form of unstable periodic orbits. The existence

and behaviour of these solutions was fundamental to the development of the theory of the self-sustaining process [58].

Plane Couette Flow. Steady state solutions were first found numerically in plane Couette Flow by Nagata in 1990, by utilising a homotopy from Taylor vortex flow [59]. The method of homotopy indicates that there is a close relationship between different plane shear flows, and has also been used to calculate steady state and travelling wave solutions for plane Poiseuille [60] and channel flow [61]. The other method which has been used to calculate coherent structures is to use a direct numerical simulation to search for behaviour which looks as if it might be close to a coherent structure, and then using some kind of Newton method to try to find the structure. As well as steady state solutions, travelling wave solutions and unstable periodic orbits have also been found [62–65] and a database of the solutions can be found at `channelflow.org`, the website of the Channelflow software used in many of these studies to find solutions [66].

The coherent structures for plane Couette flow differ in an interesting way from those observed for pipe flow, the coherent structures can arrange themselves in such a way to create large scale regular patterns of bands [67]. This behaviour suggests there is a state somewhere intermediate between the purely laminar and purely turbulent states.

Pipe Flow. In pipe flow the constant downstream flux necessitates that the coherent structures are travelling waves rather than steady states. The similarity in the dynamics of Couette flow and pipe flow had led to speculation that there were also coherent structures for pipe flow, and this was shown to be true in 2003 by Faisst & Eckhardt [68] when they identified a family of three-dimensional travelling waves. There has since been a number of studies numerically finding travelling waves [69, 70] although an analysis by Kerswell & Tutty [71] argued that travelling wave solutions alone would not be enough to characterise mean flow properties, and that relative periodic orbits would be needed. Relative periodic orbits for pipe flow have indeed now been found [72–74].

The unstable nature of the coherent structures means that they are not exactly observable in an experiment; however, it *is* possible to observe close approaches to the states as was done in a striking experiment in 2004 by Hof *et al.* [56]. The fact that this is possible is due to the fact that the system can be expected to spend a large proportion of its time in the vicinity of the coherent structures; a statistical analysis of the flow found that it was $\approx$ 20 percent of the time [22].

The bifurcations undergone by travelling waves in pipe flow was studied in great depth in a 2011 paper by Mellibovsky & Eckhardt where a double-zero (Takens-

Bogdanov) bifurcation was explored used a pseudo-arclength continuation method [75]. This study revealed the beautiful and complex structure created by the coherent structures in a system which might seem at first glance to be nothing more than stochastic noise.

Dynamical Role. The fact that we do not typically see the system persist in one of these states indicates that they are unstable and this is indeed the case. As Re is increased coherent structures are created via saddle-node bifurcations 'from infinity' [76], similarly to the cartoon presented in figure 1.1. Despite their instability, the coherent structures play an important role in organising the dynamics of the turbulent flow. The close approaches observed by Hof *et al.* [56] are then proceeded by the system falling away from the vicinity of the coherent structure in an unstable direction which it then follows until it comes into the vicinity of another coherent structure; thus the system evolves in a 'ping pong' fashion, bouncing from state to state, and heteroclinic connections between coherent structures have been calculated in plane Couette flow [77] and pipe flow [78].

It has been known for some time that it is possible to use periodic orbits of the flow to predict the statistical properties of the system, using a perturbative method [79, 80], although full description of a real fluid flow using this method has not yet been completed. However, this technique was used by Chandler & Kerswell to study a two-dimensional Kolmogorov flow[81]. A recent study by Budanur *et al.* [74] found a number of relative periodic orbits in pipe flow, and if these types of searches continue we might expect to be able to use the periodic orbit theory to describe pipe flow and plane Couette flow in the future.

1.2.2 UPPER & LOWER BRANCHES

The fact that the coherent structures are created in saddle node bifurcations with concomitant upper and lower branches presents the interesting question of how the two states relate to one another, and if they play different roles in the transition scenario. To see the difference between them it is instructive to consider their comparative linear stability.

In a 2007 paper, Wang *et al.* found lower branch coherent states in Couette flow using a Newton method and found that the lower branch states only had a single unstable eigenvalue [82] and this remained the case as Re number was increased to as high as $Re = 12000$. The fact that there is only one unstable eigenvalue implies that the state space in the vicinity of the coherent state can be split in two by the stable manifold of that state, and it was found that states on one side of the divide would decay to laminar flow, whereas states on the other side would

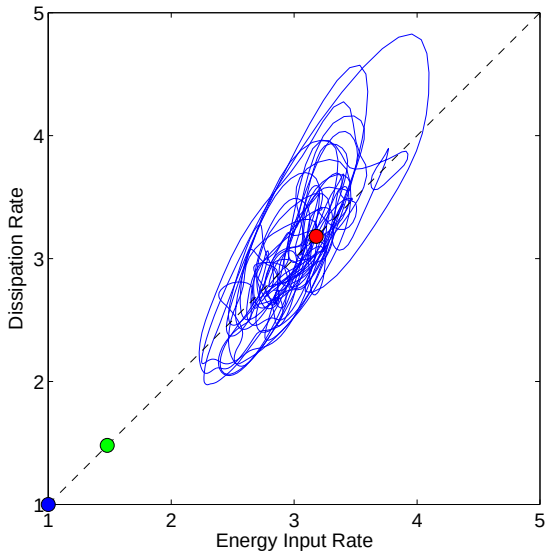

Figure 1.5: The differing dynamical roles of the three types of states, illustrated with an example reproduced from [57]. The red dot is the location of an upper branch state, the green dot a lower branch state, and the blue dot the laminar state. The upper branch state acts as an 'organising centre' while the lower branch state separates phase space into turbulent and relaminarising regions.

exhibit turbulent behaviour. The stable manifold of the lower branches seems to play an important role in partitioning the state space into turbulent and non-turbulent regions. Interestingly, the lower branch states become less unstable as Re increases, a finding replicated in a related 2008 study by Viswanath [83] wherein a similar picture for the dynamical role of the stable manifold of the lower branch is painted.

The upper branches appear to play a different dynamical role, being the 'organising centres' of the turbulent flow - as depicted in figure 1.5.

The situation appears to be similar in pipe flow [73, 84] although it appears that the lower branch has more than a single unstable mode.

The Edge of Chaos. The partitioning role of the lower branch states naturally leads to the question of what the boundary between turbulent and non-turbulent regions of phase space is like. In a 2006 study of a low-diemsional model, Skufca *et al.* introduced the concept of the *edge of chaos* to describe this structure and also described a method by which it can be computed [85]. An interesting question raised by the authors is that of how it is possible for the system to relaminarise through the edge at all, and they conjecture that it is due to the fractal nature of the edge.

A similar edge tracking method was used to calculate the edge of chaos in a pipe [86] and found within the edge the so called *edge state* - an invariant state on the edge of chaos which is attractive to states confined to the edge. This process was repeated for plane Couette flow [87] and it was found that the edge tracking algorithm finds

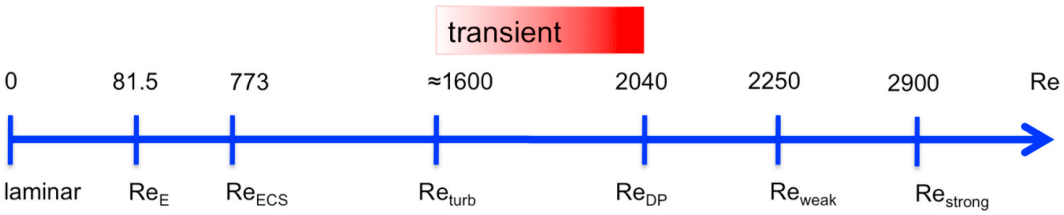

Figure 1.6: Summary of our current understanding of the transition to turbulence for pipe flow, reproduced from [90]. Coherent structures are produced before turbulence is exhibited, at Reynolds number approximately 773. Transient turbulence, characterised by finite lifetimes of puffs is between $Re \approx 1600$ and somewhere near $Re = 2040$, at which point there is a statistical transition to infinitely sustained turbulence (in the thermodynamic limit). As Reynolds number increases even further we reach the domains of first weak and then strong turbulence, but theses types of behaviours have not been studied in this thesis. We will be focussing our attention on the region between Re_{ECS} and Re_{DP}.

that the edge state is the same as the lower branch with one unstable eigenvalue discussed above. In a further paper about the dynamics at the edge in pipe flow a modification of the edge tracking algorithm is used, due to the fact that the pipe flow edge state has more than one unstable direction, and has unstable directions *within* the edge[88].

A 2009 paper by Viswanath & Cvitanović [84] propose a method by which perturbations can be found which lie on a given lower branch state, which has obvious applications to the study of the edge of chaos. A general strategy for determining minimal perturbations which evolve into turbulence is proposed in [89], which is related to the edge of chaos, but also related to the minimal threshold scaling as discussed in section 1.1.1. This allows us to see the connection between the coherent structures and quantities which have always been of interest in studies of the transition, and is an example of the way which dynamical systems theory can illuminate quite practical aspects of the system.

1.3 SUMMARY OF OUR UNDERSTANDING

The above discussions can make Reynolds' initial question seem like a daunting one, and it's true that he probably could not have imagined the degree of complexity of the answers we currently have to it. The situation can be summarised for pipe flow in figure 1.6, reproduced from a review by Eckhardt [90]. As we increase the Reynolds number we see the emergence of the first coherent structures at approximately $Re = 773$, although this by itself is not enough to sustain turbulence. The state space increases in complexity via the creation of further coherent structures (and the bifurcation of existing ones) until a chaotic saddle has formed, at roughly

$Re = 1600$, the minimum value for which turbulence is observed. We then have the transitional region which is characterised by increasing lifetime of turbulent puffs, as well as increasing chance for the puffs to split. This culminates in a DP style transition to sustained turbulence near $Re = 2040$. Above $Re \approx 2250$ we see a decreasing amount of intermittency, eventually leading to strong turbulence. This Thesis will focus on the transitional region, so a detailed discussion of weak and strong turbulence is not required.

The situation for plane Couette flow is not quite as accurately mapped out, although we know that the original coherent structure reported by *Nagata* was followed to $Re = 125.7$. Statistical analysis has suggested an $Re_{turb} \approx 310$ and $Re_{DP} \approx 325$ [42]. Featureless turbulence is observed above $Re = 415$ [17].

1.4 SIMPLE MODELS

A partial differential equation like the Navier-Stokes equation is by nature an infinite dimensional problem. However, the discovery of the self-sustaining process [58] and coherent structures suggests that there is a lower-dimensional way of thinking about transitional turbulence [91]. Many attempts to reduce the dimensionality of the problem use the Galerkin method with the number of modes truncated using symmetry arguments or some physically motivated reasoning. These models have been quite successful in capturing many of the features of the transition [65], including coherent structures [92], exponential lifetime statistics (with superexponential scaling) [93, 94] and laminar-turbulent patterning [95]. In some cases these models were instrumental in originally developing hypotheses which could be tested for higher dimensional numerical studies or experiments; e.g. a Galerkin model was used to understand the edge state [85].

Other methods used to construct simplified models are often coming at the problem via the intermittency route to chaos, motivated by the analogy with DP[3] and have included fairly straightforward applications of DP type dynamics [47, 96], predator-prey ecological models [33, 97], and thinking of the fluid as being a kind of bistable medium [46, 98].

The simple models presented here all share something in common; they are trying (to greater or lesser degree) to actually model a physical fluid flow. There is an alternative route: instead of trying to directly model the systems in question, we could instead look for (or create) simple toy systems which appear to have many of the properties we are looking for. The fact that there is a class of shear flows

[3] DP can itself be thought of as a low dimensional model of the transition

which share so many features suggests that there could be some kind of 'dynamical universality class' to which they belong. Perhaps all subcritically chaotic systems share some degree of structure and behaviour? To that end, I am now going to introduce one candidate for such a toy, the Kuramoto-Sivashinsky equation.

1.4.1 THE KURAMOTO-SIVASHINSKY EQUATION

The Kuramoto-Sivashinsky equation was introduced in the 1970s on two separate occasions; once by KURAMOTO *et al.* to describe turbulence in reaction-diffusion systems of interest in chemistry [99, 100], and again by SIVASHINSKY to describe an instability in flames [101]. It can be written as follows [102]:

$$\partial_t u = -\partial_x^4 u - \partial_x^2 u + u\partial_x u, \quad x \in [0, L] \tag{1.3}$$

Simplicity. In a 2009 paper, BRUMMIT & SPROTT conducted an exhaustive search of partial differential equations in an attempt to find the simplest chaotic partial differential equation (with a quadratic or cubic nonlinearity and periodic boundary conditions) with 'complexity' defined by a metric which they introduced. Only PDEs with 'complexity' less than that of the KS equation were tested, and the presence of chaos was determined by measuring the largest Lyapunov exponent for a range of values of the parameters and initial conditions. None of these simpler PDEs were found to have a positive Lyapunov exponent (and be well formed). This makes the KS equation a good place to start looking for novel low-dimensional models of the transition.

Rich Behaviour. Equation 1.3 as it stands has only one controllable parameter, the domain size L, but simple as it is, the KS equation is known to exhibit a large variety of rich spatiotemporal dynamics[4]. Turbulent states with a finite lifetime have been observed (where there are many different stable solutions which the turbulence 'decays' to) [103] with lifetime increasing with L. In this paper the author states that "The nontrivial behavior of the KS equation stems from the linear instability of the laminar, $u = const$, solution" which is a way in which the standard KS equation is not analogous to a subcritical transition such as pipe flow or PCF because those flows are linearly stable. It also highlights another way in which the equation are not akin to the real transition in that there is a continuum of laminar flows. Spontaneously decaying spatiotemporal chaos was also reported in another study of the KS equation [104], but the linear instability of the laminar flow means that the laminar flow is also transient, and can spontaneously 'burst' back to life.

[4]Coefficients are sometimes added to each of the terms to change the properties of the system.

The KS equation has also been shown to behave as a low dimensional system of ordinary differential equations, with a complex series of bifurcations [105] which 'bridges the gap' between PDEs and dynamical systems.

Coherent structures of various kinds have also been found for the KS equations, including steady states and travelling waves [106], modulated travelling waves [107], and unstable periodic orbits [102, 108, 109]. The unstable periodic orbits have also been related to a crisis bifurcation [110–112], reminiscent of one known to be present in plane Couette flow.

An eight-mode Galerkin representation of KSE is enough to produce an incredibly rich bifurcation scenario, as shown in [113] and [114], along with some very interesting visualisations of unstable manifolds of fixed points.

1.4.2 THE DAMPED KS EQUATION

The KS equation - once supplemented with a damping term - is closely related to the Swift-Hohenberg equation [115] (albeit with a different nonlinearity than is normally used there). The addition of the damping term is done as follows:

$$\partial_t u = -(1-\epsilon)u - \partial_x^4 u - 2\partial_x^2 u + u\partial_x u\,, \tag{1.4}$$

where ϵ is a control parameter which controls the amount of damping. This equation is known as the stabilised or damped KS equation. This equation also has a rich dynamics, exhibiting spatiotemporal chaos [116, 117].

Of particular interest in this thesis is that the equation was used by Chaté & Manneville in one of the earliest examples of the intermittency route to chaos for a PDE [40], very soon after Pomeau's suggestion of the link between DP and subcritical chaos. Like many studies of KS dynamics domain size is used as control parameter and as it increases, the transition first goes to a periodic state, and then a quasiperiodic state before finally reaching the regime of spatiotemporal chaos. The analogy to DP was noted but no attempt was made to measure the critical exponents or in some way verify the universality class of the system although it seems likely that this model does indeed belong to the DP class. More recent work on the damped KS equations with 2D geometry and a 3D domain has shown again that there is qualitative agreement with DP experiments [118].

A detailed analysis of the bifurcations for the damped KS equation shows that it undergoes a series of bifurcations to a chaotic *attractor* [117] which again is not the kind of system we are interested in when modelling the transition to turbulence for pipe flow or PCF where the evidence suggests we have a chaotic saddle.

1.5 THESIS STRUCTURE

The thesis will proceed as follows. Firstly, I will discuss a model system of partial differential equations (based on the damped KS equation) which has bears a striking resemblance to the paradigmatic hydrodynamic flows discussed in this introduction.

Motivated by behaviour seen in this model (and by knowledge of the dynamical roles played the coherent structures in pipe and Couette flow) I will then turn my attention to a novel directed percolation type system, featuring three state types instead of two.

Lastly, I will come back to the extended KS model and examine its behaviour in a spatially extended domain.

2 A SUBCRITICAL EXTENSION OF THE KURAMOTO-SIVASHINSKY EQUATION

2.1 INTRODUCTION

The subcritical transition in pressure driven pipe flow and plane Couette flow seems to belong to some kind of family of related flows, characterised by a few notable features, including: linearly stable laminar flow, transient spatiotemporal chaos with memoryless decay, super-exponential scaling of the typical lifetimes, the existence of coherent structures to organise the chaotic region of phase space, a directed percolation transition in extended domains. In this chapter I will study a model system of partial differential equations and argue that it too belongs to this same family, and the fact that it is related to a partial differential equation known to be one of the simplest to exhibit spatiotemporal chaos (the Kuramoto-Sivashinsky equation) [119] suggests that it may be one of the simplest members of this family of systems.

The model examined in this research is based on the *damped* Kuramoto-Sivashinsky equation and was introduced by Becherer *et al.* in the paper *Probing a subcritical instability with an amplitude expansion: An exploration of how far one can get* [120] where it was constructed to exhibit a subcritical bifurcation to a chaotic state. The model is not a direct model of any real fluid flow - it is a system of partial differential equations that shares many characteristics of those flows, but values of the fields do not represent any physical quantity. We will now give a sketch of the system, and motivate why it has the form it does.

2.2 THE MODEL

The damped KSE is used as the base of the system, and it a well known example of a system with chaotic dynamics [105]. It can be written:

$$\partial_t u = -\partial_x^4 u - 2\partial_x^2 u - (1-\epsilon)u + u\partial_x u \tag{2.1}$$

This equation exhibits a transition to spatiotemporal chaos, but the transition does not exhibit the exact behaviour we want. The damped KSE transitions to spatiotemporal chaos via quasiperiodicity and temporal chaos [104]. Once the system has undergone this transition a chaotic attractor is formed [117] which is not analogous to the apparently always finite-time behaviour of pipe-flow turbulence. The parameter ϵ acts as control parameter for the system, values of ϵ below around 0.7 show a supercritical bifurcation to a regular pattern, and for ϵ above this value the patterns become unstable and allow for chaos to emerge.

Becherer *et al.* propose coupling a second scalar field to u with behaviour constructed to allow a linearly stable laminar state and spatiotemporal chaos for some perturbations. The field is coupled in the following way:

$$\partial_t u = -\partial_x^4 u - 2\partial_x^2 u - (1-\epsilon)(u - f(v)u) + u\partial_x u\,, \tag{2.2}$$

for some function $f(v)$. It is worth noting here that although this system has two fields, u and v it is not a two-dimensional system, there is only one spatial coordinate, x. In fact, in many calculations the fields u and v are simply appended to one another and the calculations are performed on this combined vector. The trivial $u(x) = v(x) = 0$ solution is to be a stable, absorbing state to which any turbulence can decay. From this point forward we will refer to this state as the 'laminar' state, because it will play the same role for this system that the laminar state does for the real flows. For small values of v we want $f(v)$ to act against any perturbation in u, but for large enough values of v we want it to drive the system away from the laminar state. A suitable candidate for $f(v)$ was found to be $f(v) = av - bv^2$, which should give the desired behaviour, provided the variables a and b are chosen correctly.

The time evolution of the field v was also defined with a view to producing the desired behaviour. We wish v to increase if u is perturbed, in order to drive the system, but when $u = 0$ we wish $v = 0$ to be stable. A form which satisfies this is $\partial_t v = D\partial_x^2 v - v + Ru^2$. The diffusion term causes the driving from v to apply more or less to the whole system equally, depending on the choice of D. The term Ru^2 is the term which causes a perturbation of u to increase v and drive the system away from laminar; therefore the coefficient R in some sense characterises the system's propensity for chaos and the size of perturbations required to trigger the turbulent behaviour. This is a similar role to that played by the Reynolds number in shear flows and we will be using R as a control parameter for much of this paper, analogously

Coefficient	Value
D	40
a	0.125
b	0.004
ϵ	-0.1

Table 2.1: The values of the coefficients used, taken from Becherer *et al.* [120] where they were shown to allow the extended KSE to exhibit a subcritical transition to transient spatiotemporal chaos.

to how the Reynolds number is often used in hydrodynamic experiments. We will use the same coefficients used by Becherer *et al.* which can be seen in table 2.1. The full system of PDEs (which from now on we will call the extended Kuramoto-Sivashinsky equation or eKSE) is:

$$\partial_t u = -\partial_x^4 u - 2\partial_x^2 u - (1-\epsilon)(u - f(v)u) + u\partial_x u \tag{2.3a}$$

$$f(v) = av - bv^2 \tag{2.3b}$$

$$\partial_t v = D\partial_x^2 v - v + Ru^2 \tag{2.3c}$$

2.3 TIME ITERATION METHOD

Space Discretisation. Space is discretised using periodic boundary conditions and a pseudospectral method[121] spatial derivatives are done in Fourier space while multiplication is done in real space. Pseudospectral methods have the advantage that for smooth function the spatial derivatives are very accurate and easy to calculate, as well as allowing a smaller number of lattice sites than would be required by using a finite-difference method [122]. Calculating a straighforward multiplication is more computationally taxing in Fourier space than in real space and so this is done in real space, given that transforming between Fourier space and real space can be done very efficiently using a fast Fourier Transform (FFT). Transforming between Fourier space and real space is done using a FFT algorithm implemented by the FFTW3 library [123].

Time Discretisation. Time is discretised using a split-step method, which allows a numerically stable implicit method to be used for the linear terms but without the computational cost which comes from trying to do the same with the nonlinear terms. Therefore we will separate the equations of motion into their linear and

nonlinear terms as follows:

$$\partial_t u = L.u + g(u, v) \tag{2.4a}$$
$$\partial_t v = K.v + h(u, v)\,, \tag{2.4b}$$

where L and K are linear operators (represented as matrices in our discretisation) and $g(u, v)$ and $h(u, v)$ are functions represented the nonlinear terms of the equations. Specifically this means that the operators and functions have the following values:

$$L = -\partial_x^4 - 2\partial_x^2 - 1 + \epsilon \tag{2.5a}$$
$$K = D\partial_x^2 - 1 \tag{2.5b}$$
$$g(u, v) = (1 - \epsilon)uf(v) + u\partial_x u \tag{2.5c}$$
$$h(u, v) = Ru^2 \tag{2.5d}$$

Notice that there is no nonlinear term for the time evolution of v which is a function of v, so we have $h(u, v) \equiv h(u)$. For the nonlinear terms the two-step Adams-Bashforth method has been used, to generate an intermediate state to feed to the implicit method:

$$u_n^* = u_n + \frac{3\delta t}{2} g(u_n, v_n) - \frac{\delta t}{2} g(u_{n-1}, v_{n-1}) \tag{2.6a}$$
$$v_n^* = v_n + \frac{3\delta t}{2} h(u_n) - \frac{\delta t}{2} h(u_{n-1})\,, \tag{2.6b}$$

where δt is the size of the desired time-step, the subscripts on u and v represent the number of the time-step, and the starred vectors are intermediate vectors to which we will apply the linear operators. In order to use a two step method like this we need to have the value of g and h and a previous time iteration, so for the very first time-step of the run we cannot use this method and instead use the one step Euler's method.

For the linear terms the Crank-Nicolson method is used, as follows:

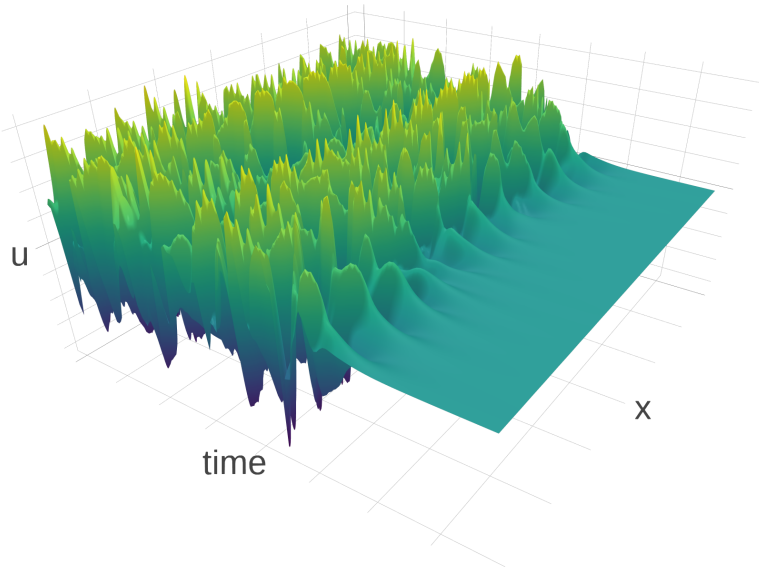

Figure 2.1: Example of the evolution of the field u for a random initial condition. Exhibits transient chaos then decay.

$$u_{n+1} = \left(L - \frac{2}{\delta t} I\right)^{-1} \left(L + \frac{2}{\delta t} I\right) u_n^* \tag{2.7a}$$

$$v_{n+1} = \left(K - \frac{2}{\delta t} I\right)^{-1} \left(K + \frac{2}{\delta t} I\right) v_n^* \,, \tag{2.7b}$$

where I is the identity matrix. The advantage of using the split-step now makes itself apparent - the linearity of the operators means that the inversion only has to be done once because the matrices representing them do not depend on the value of any time dependent quantity. In fact, in Fourier space the operators are represented by diagonal matrices, meaning that the inverse is just the reciprocal of the diagonal elements.

2.4 PHENOMENOLOGY OF THE MODEL

Using the numerical method outlined above and appropriate initial conditions the system exhibits transient spatiotemporal chaos, as shown in figure 2.1. Typically, u is an approximately trigonometric function of x, while v tends to be closer to a

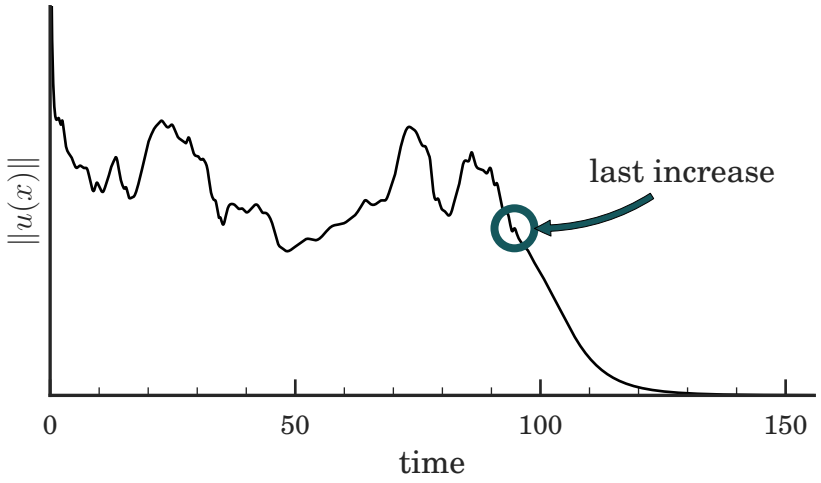

Figure 2.2: Only the norm of $u(x)$ is used to determine the moment of relaminarisation. Turbulence is deemed to have ended at the last time the norm increases.

constant positive value. Once in the laminar state the system does not spontaneously come back to life or exhibit the 'bursty' behaviour as reported in the damped KS equation by Rempel *et al.* [104] (which is due to the merging of a chaotic saddle and a spatially regular attractor).

2.4.1 TYPICAL LIFETIMES

An example of the typical behaviour of the system can be seen in Fig. 2.1. We perturb the system by starting the run at some vector away from the laminar state. It will then exhibit chaotic behaviour before eventually decaying to the laminar state. This behaviour is similar to the transient turbulent states seen in the real flows.

For the real flows, the relaminarisation process is memoryless, which causes the survival probability curve to have an exponential profile. To see if this is true for our system we have to define what we mean by the relaminarisation time; the decay is usually relatively slow and smooth during relaminarisation so it is not particularly clear how to choose a well-defined time to use for this measure. Our choice is based on the observation that the behaviour of the norm of u can be split into two sections: there is initially chaos but during the relaminarisation process we observe a monotonic decrease in the norm. This suggests using the last time at which the norm of u increases as the time at which the chaos dies, as shown in figure 2.2.

The system has a linearly stable 'laminar' state at $u(x) = v(x) = 0$ and so finite-sized perturbations are requried to initiate spatiotemporal chaos. Initial perturbations are created in the following way:

$$u(x) = A_c \cos(k_c x) + A_s \sin(k_s x)$$
$$v(x) = 0\,, \tag{2.8}$$

with $8 < A < 12$ and $0.9 < k < 1.1$. These initial conditions have been observed to always cause chaos, provided R is large enough to be in the chaotic regime. The system is then evolved until death 10,000 times (with unique initial conditions) for each of a range of values of R = $0.65, 0.7 ... 1.05$. We expect for a chaotic saddle that these lifetimes will be exponentially distributed [124] and this appears to hold for our system too, as can be seen in figure 2.3a where survival probability curves have been plotted on a semilog plot. The typical lifetime is calculated by noting that the maximum likelihood estimator for the decay rate in Poisson distribution is simply given by the mean of the values [125]; the typical lifetime for a given R is therefore just the mean of the death-time for all runs at that R. The error in the lifetime is given by the standard deviation of the mean:

$$\tau = \frac{1}{N} \sum_{i}^{N} d_i\,, \tag{2.9}$$
$$\sigma_\tau = \frac{\sigma_d}{\sqrt{N-1}}\,, \tag{2.10}$$

where d represents a death time and σ_x is the standard deviation of the quantity x. For R smaller than about 0.8 the distribution no longer appears to be a Poisson distribution, so this method will not be a fair measure. The convergence of the typical lifetimes has been used to find the spatial and temporal resolutions to conduct the simulations at; the typical lifetimes were calculated for a range of temporal and spatial resolutions and convergence was found at 50 Fourier modes and a timestep of 0.001.

In the real flows it has been found that increasing the Reynolds number causes the typical lifetime of the turbulent state to increase at a rate which is faster than exponential (super-exponential). We suspected that the parameter R in this system could play a similar role to that played by the Reynolds number in the real flows, and so might expect this super-exponential scaling to be replicated. This is indeed the case, as can be seen in figure 2.3b. We only include points for $R > 0.8$ because when R is too low we observe different behaviour, as will be outlined in the next section. The data is fitted with an exponential of an exponential using Scientific

Python's `curve_fit` which yields the following expression for the lifetimes:

$$\tau \approx 0.00039 \exp\left(\exp\left(\frac{R - 0.027}{0.38}\right)\right) + 1.57. \tag{2.11}$$

2.5 LOW R REGION

At lower values of R (below around 0.8) we see a survival probability curve which is not a straightforward exponential, indicating that the system does not have a constant rate of decay at these values of R. The survival probability curve for $R = 0.65$ is shown in figure 2.5a and appears to show the sum of two different exponentials. We see different (but still constant) rates of decay depending on if the system is long-lived or short-lived which suggests that there are two different types of behaviour. In order to see what these behaviours are, it is instructive to plot the norm of u against time, as can also be seen (for a small sample of runs) in figure 2.4. What we see is that the vast majority of runs relaminarise nearly immediately. These runs show a limited amount of turbulent motion, as they die so quickly that we see a nearly monotonic decrease towards the laminar state; this behaviour is the cause of the short-time exponential seen in the survival probability graph. These runs do not usually last long enough to exhibit much fully fledged turbulent behaviour. The combination of very long lifetimes and two different exponentials in the survival probability curve is reminiscent of a boundary crisis observed in pipe flow [126] but in this scenario there does not seem to be a chaotic attractor, merely a non chaotic attractor.

The other behaviour observed is a long-lived non-turbulent state which has a nearly constant value of the norm of u in time. Figure 2.5b shows an example of one of these runs. The long lived states are unstable periodic orbits and all of the runs correspond to the same orbit. The non exponential survival probability curve is caused by the existence of this unstable orbit which disappears at higher values of R.

Neither of these behaviours is a fully-fledged turbulent state, and it seems that at such low values of R the phase space does not yet have the complexity required to allow turbulence. It might be tempting to suspect that this long-lived state is related to the edge of chaos but in fact this is does not seem to be the case, because it appears to be in the vicinity of upper branch coherent structures (which we will discuss in the next section) not lower branch solutions, so the dynamical role of this state must be different than that of the edge state.

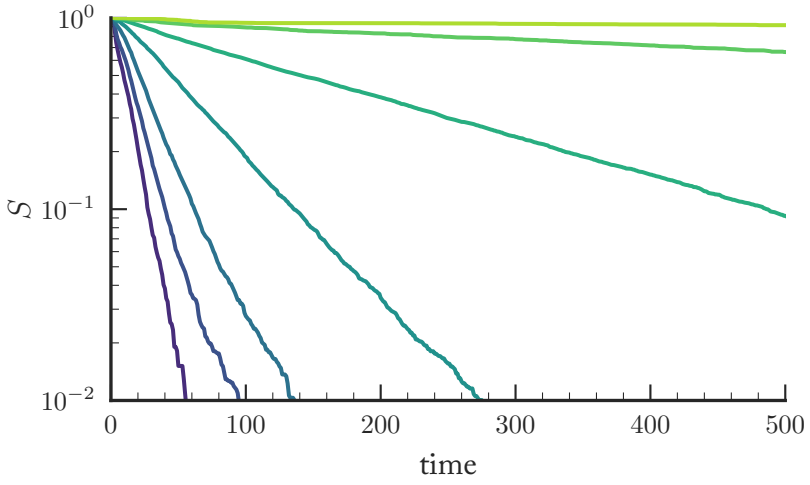

(a) Survival probability curves for $R = 0.8, 0.85...1.1$ on a semi-log plot. Straight lines indicate an exponential distribution of lifetimes.

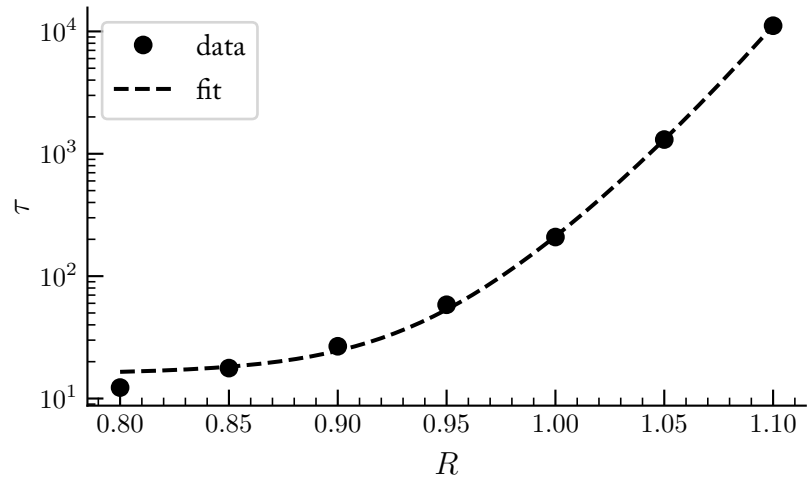

(b) Typical lifetime τ as a function of R on a semilog plot, as measured from survival probability curves. The semilog plot makes it clear that the scaling of the lifetimes is faster than exponential. Dotted line indicates a super-exponential fit of the data: $\tau \approx 0.00039 \exp(\exp(\frac{R-0.027}{0.38})) + 1.57$

Figure 2.3: Two figures showing the lifetimes of the transient turbulence. Lifetimes are exponentially distributed and scale super-exponentially with the nonlinear interaction term R.

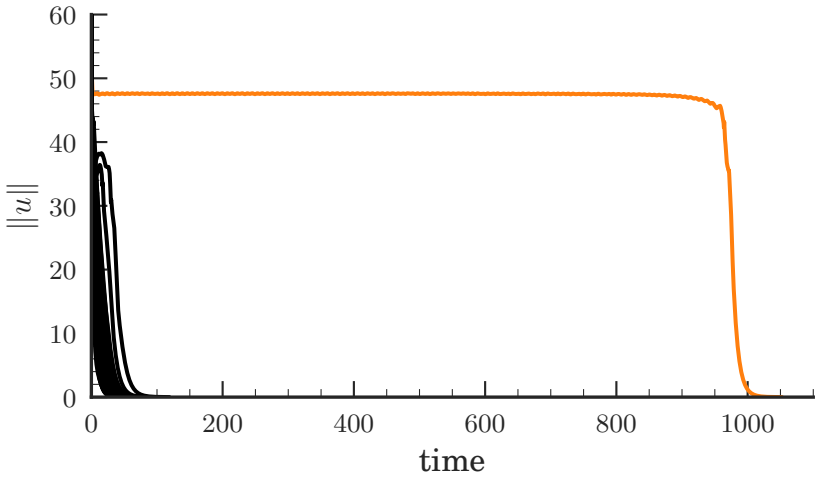

Figure 2.4: The norm of u as a function of time at $R = 0.65$, for a selection of different initial conditions. The majority of runs (plotted in black) decay almost immediately, but there occasional long lived runs, an example of which is plotted in orange.

2.6 COHERENT STRUCTURES

Coherent structures are invariant solutions the equations of motion and are known to organise the dynamics in turbulent shear flows and can either be periodic orbits or steady-state solutions. In order to find exact coherent structures for our system, a Newton method has been employed. We only looked at steady state solutions in this research - it is likely that there exists unstable periodic orbits in addition to the steady state solutions presented here.

2.6.1 NUMERICAL METHOD

A finite difference scheme can be employed to find coherent structures using a Newton method. Assume there exists some state (u_c, v_c) for which the time derivative is zero, i.e.

$$F(u_c, v_c) = G(u_c, v_c) = 0 \tag{2.12}$$

where $F(a, b)$ and $G(a, b)$ are the time derivatives of u and v evaluated at $u = a$ and $v = b$. Now assume that we do not already have (u_c, v_c) but instead we have some state which is in the neighbourhood of the fixed point such that $(u_c, v_c) \approx (u + \delta u, v + \delta v)$. We can now expand our expressions for F and G, and keep only

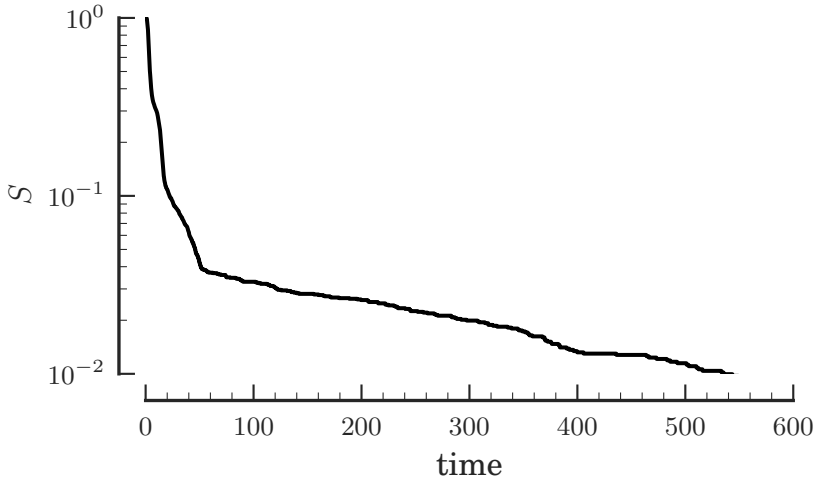

(a) Survival probability curve for $R = 0.65$ showing non-constant probability of decay.

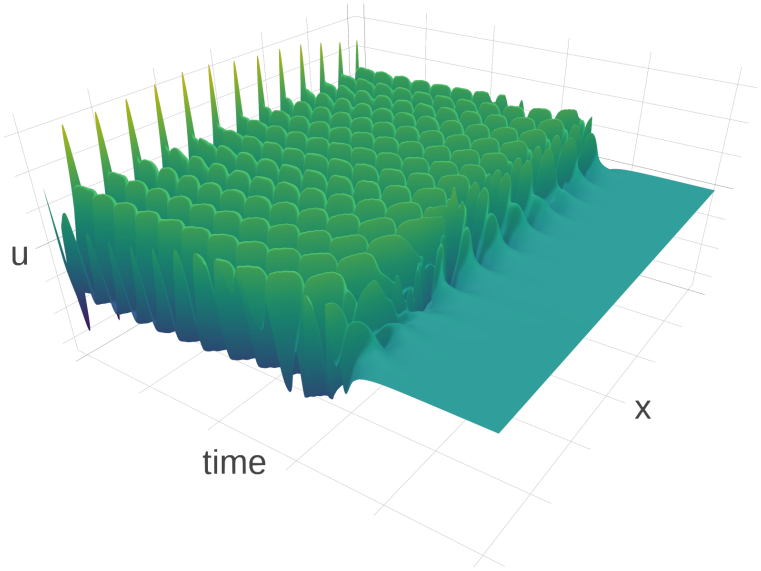

(b) Example of long-lived non-turbulent state. All long-lived states observed at this value of R are examples of this same unstable orbit.

Figure 2.5

terms which are linear in δu and δv. First, for $F(u+\delta u, v+\delta v)$ we have:

$$0 = F(u+\delta u, v+\delta v) = -\partial_x^4(u+\delta u) - 2\partial_x^2(u+\delta u) - (u+\delta u) + \epsilon(u+\delta u) \\ + (1-\epsilon)f(v+\delta v)(u+\delta u) + (u+\delta u)\partial_x(u+\delta u). \quad (2.13)$$

The procedure now is to expand all of these terms and throw away anything which has more than linear complexity in δu or δv. First we will consider the term $f(v+\delta v)(u+\delta u)$ by Taylor expansion:

$$f(v+\delta v)(u+\delta u) \approx f(v)u + \delta v u \partial_v f(v) + \delta u \partial_u f(v) u \quad (2.14)$$
$$= f(v)u + (au + 2bvu)\delta v + f(v)\delta u. \quad (2.15)$$

Now we do the same for the other nonlinearity:

$$(u+\delta u)\partial_x(u+\delta u) = u\partial_x u + u\partial_x \delta u + \delta u \partial_x u + \delta u \partial_x \delta u \quad (2.16)$$
$$\approx u\partial_x u + u\partial_x \delta u + \delta u \partial_x u \quad (2.17)$$

By combining these approximations we get the following linearisation for F:

$$F(u,v) \approx -\partial_x^4 \delta u - 2\partial_x^2 \delta u - \delta u + \epsilon \delta u \\ + (1-\epsilon)(f(v)\delta u + (au + 2bvu)\delta v) + u\partial_x \delta u + \delta u \partial_x u \quad (2.18)$$

We can then collect the δu and δv terms to get:

$$\left[\partial_x^4 + 2\partial_x^2 + 1 - \epsilon - (1-\epsilon)f(v) - u\partial_x - \partial_x u\right]\delta u \quad (2.19)$$
$$- \left[(1-\epsilon)(au + 2bvu)\right]\delta v = F(u,v). \quad (2.20)$$

We can then follow the same procedure for $G(u,v)$, which results in the following expression:

$$[-2Ru]\delta u \quad (2.21)$$
$$+ \left[D\partial_x^2 - 1\right]\delta v = G(u,v). \quad (2.22)$$

We can now use a finite difference representation of the derivative operators in

the expression above, of which there are three:

$$\partial_x^4 u_i \approx \frac{u_{i-2} - 4u_{i-1} + 6u_i - 4u_{i+1} + u_{i+2}}{\delta x^4}, \tag{2.23}$$

$$\partial_x^2 u_i \approx \frac{u_{i-1} - 2u_i + u_{i+1}}{\delta x^2}, \tag{2.24}$$

$$\partial_x u_i \approx \frac{u_{i+1} - u_{i-1}}{2\delta x}, \tag{2.25}$$

where the subscript represents the index of the lattice point of the spatial discretisation. Due to the periodic boundary conditions, all of the arithmetic in the subscripts is done modulo N. With this in place we can represent the operators implied by equations 2.20 and 2.22 as matrices, constructed in the following manner:

$$\begin{pmatrix} A & B \\ C & D \end{pmatrix} \begin{pmatrix} \delta u \\ \delta v \end{pmatrix} = \begin{pmatrix} F(u,v) \\ G(u,v) \end{pmatrix}, \tag{2.26}$$

with A, B, C, and D taking on the forms calculated above. Specifically:

$$A_{ii} = \frac{6}{\delta x^4} + \frac{-4}{\delta x^2} + 1 - \epsilon - (1-\epsilon) f(v_i) - \partial_x u_i, \tag{2.27}$$

$$A_{i\pm1} = \frac{-4}{\delta x^4} + \frac{2}{\delta x^2} \pm \frac{u_i}{2\delta x}, \tag{2.28}$$

$$A_{i\pm2} = \frac{1}{2\delta x^4}, \tag{2.29}$$

$$B_{ii} = -(1-\epsilon)(a u_i + 2b v_i u_i), \tag{2.30}$$

$$D_{ii} = \frac{2D}{\delta x^2} + 1, \tag{2.31}$$

$$D_{i\pm1} = -D\frac{1}{\delta x^2}, \tag{2.32}$$

$$C_{ii} = -2R u_i. \tag{2.33}$$

This defines a system of $2N$ equations with $2N$ unknowns, which is then solved using Scientific Python's `scipy.linalg.solve` method. These equations can then be iteratively solved to approach a solution. We define the following quantity:

$$h(u,v) \equiv \sqrt{\sum u_i^2 + \sum v_i^2}\,, \tag{2.34}$$

and stop iterating when $h(u,v) < 1\text{e}{-7}$. If we are sufficiently close to the state that our linearisation is accurate, we should expect the step to point towards the state. However, sometimes the Newton step can overshoot the actual position of the state,

so to help with the convergence I also implemented a backtracking linesearch[127]. Once the Newton step is found the new position is checked to see if it decreases the time derivative 'sufficiently', where 'sufficiently' means that it satisfies the Armijo-Goldstein condition [128]. That is, if the following inequality holds:

$$h(u + s\delta u, v + s\delta v) \leq (1 - \alpha s)h(u, v)\,, \tag{2.35}$$

for $\alpha = 1e{-}5$. The scale factor s starts at 1 and is halved until the inequality is satisfied. If the scale becomes smaller than the numerical precision the iteration is stopped.

Initial conditions were created by saving snapshots of the system as it was iterated in time in the typical lifetimes calculation outlined in the previous section - the system can be expected to spend some time in the vicinity of these structures and so snapshots should be reasonable candidates for initial guesses. The fact that spatial derivatives are done with finite differences means that a higher spatial resolution was used in the search for coherent structures - in doing the discrete Fourier transform when saving the snapshots a larger number of spatial points were used (400 each for u and v).

2.6.2 RESULTS

A number of coherent structures have been found, at a range of values of R (the lowest value of R for which a coherent structure has been found is $R \approx 0.46$). The solutions found all have a similar shape - the field u has an approximately sinusoidal shape, perhaps with an irregularity at some point. The field v has a nearly constant value (which is unsurprising considering the diffusion term in the construction of its time derivative) with an irregularity at a point matching the one in u. The equations are symmetric under a translation in x so each solution found is actually a family of solutions.

2.6.3 CONTINUATION METHOD

In order to observe the bifurcation scenario for the system we wish to follow these coherent structures as we change R. Two different continuation methods have been used, and I will briefly detail both.

Natural Parameter Continuation. The first method used is simple parameter continuation; if we wish to find out what happens to a state at some R near the value that the state has been calculated at we simply set up a new Newton iteration with the

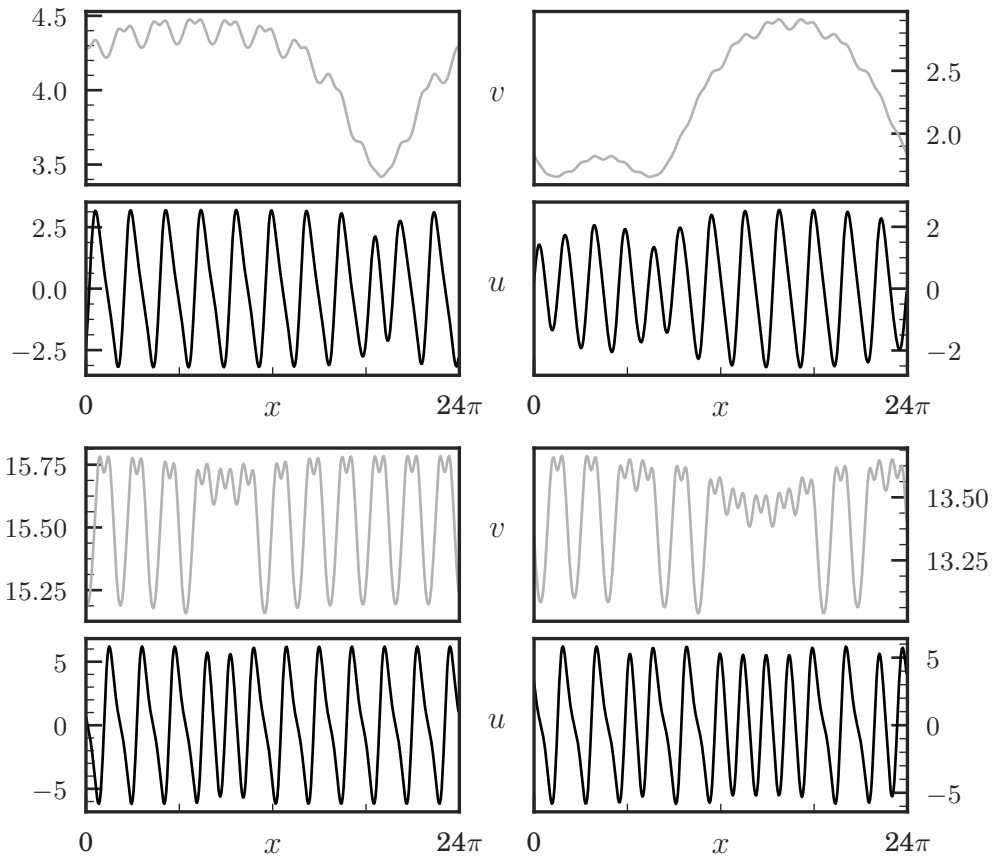

Figure 2.6: A selection of exact coherent structures found at $R = 1.0$. The top two examples are lower branch states, and the bottom two are upper branch states.

nearby R and that state. If R is sufficiently close then we can expect that the coherent structure will not change much at nearby values of R and so our linearisation should still hold and therefore there will be a high likelihood of convergence. This method works well provided the state is not near the saddle-node bifurcation point but breaks down at that point. It makes no sense to try to go 'around' the bifurcation this way and so we need some other method to follow the states. As the bifurcation point is approached the step size in R is decreased until it becomes unreasonably small; at this point we switch to another method.

Pseudo-Arclength Continuation. We proceed around the bifurcation by including the control parameter R in our definition of the state and using a pseudo-arclength continuation method [129] by parameterising the state and the control parameter by the "arclength" s.[1] We make a prediction for the values of $u(x)$, $v(x)$ and R by using the tangent of the curve around which we are following them. The tangent is just calculated numerically by using the previous positions on the curve from the natural parameter continuation step. If we have been following the state up to the bifurcation point we will have a sequence of values for $u(x)_i$, $v(x)_i$ and R_i, where the subscript i denotes the number of successful iterations. We think of the state of the system as a vector z as follows:

$$z \equiv \begin{pmatrix} u(x) \\ v(x) \\ R \end{pmatrix} \tag{2.36}$$

Then the tangent at iteration i is defined simply as:

$$T \equiv \frac{z_i - z_{i-1}}{\|z_i - z_{i-1}\|} \tag{2.37}$$

We now have basically got a explicit, Euler style integration problem, and so we predict the location of the next coherent structure to be at:

$$z_{i+1} \approx z_i + \delta s T \tag{2.38}$$

For some step size δs (the 'arclength'). Then we use a Newton method to find if we are near the structure, and converge if possible. If this step does not converge we can try again with a smaller step-size, typically found by simply halving the current step size.

[1] This method has also been used to map out the bifurcation scenario of travelling waves in a pipe [75].

2.6.4 BIFURCATION DIAGRAM

The result of these continuation methods can be summarised in bifurcation diagrams, which can be seen in figure 2.7. The y axes in the diagrams represent the norms of the fields u and v, for each coherent structure found. The diagram clearly shows the subcritical bifurcation from infinity behaviour which the equations were constructed to exhibit. Coherent structures are formed by saddle-node bifurcations and come in pairs of upper and lower branches (for some structures the situation is slightly more complicated than that, with the 'lower branches' of some pairs of states seeming to change in R in a similar way to the 'upper' branches of other pairs). The distance from the stable 'laminar' flow to the first coherent structure decreases as R is increased but does not ever reach zero - this is related to the fact that finite sized perturbations are always required to cause the system to become turbulent and is the same bifurcation structure we would expect, as the system was constructed to bifurcate in this manner. The smallest value of R for which a coherent structure was found was $R \approx 0.456$, and this value can be thought of as being analogous to the first value of the Reynolds number to have coherent structures. For pipe flow this number is $Re = 773$[90] and for plane Couette flow it is $Re = 125.7$[17]. It is analogous both in that it is the first appearance of a coherent structure, and that these structures appear at lower values of the control parameter than is needed for turbulence.

Scaling of the Lower Branches. Now that we have a bifurcation diagram we can calculate how the lowest branches scale with R, to see if it is similar to the scaling observed in pipe flow or Couette flow. To this end the distance from laminar of the lowest branch (which can be different depending on how distance is measured) is calculated as a function of R, and then this function is fitted with a power law decay as in equation 1.1. Depending on the distance measure used, the scaling is different, and three different measures have been used, the norm of u, the norm of v and the sum of those norms. It's important to note here that although we might suspect that there is a relationship between the lowest branches found in this analysis it is not the same thing as a minimal perturbation threshold, so the scaling could well be different if we were to look at the actual minimal perturbation threshold. The fitting is only done from $R = 1.1$ as the scaling we are interested in is asymptotic with large R. In order to get a better scaling ideally the continuation would be done for orders of magnitude in R. The calculation done in this way returned scaling exponents associated with the three different measures as $\gamma_u \approx 0.75$, $\gamma_v \approx 0.5$, $\gamma_{uv} \approx 0.6$.

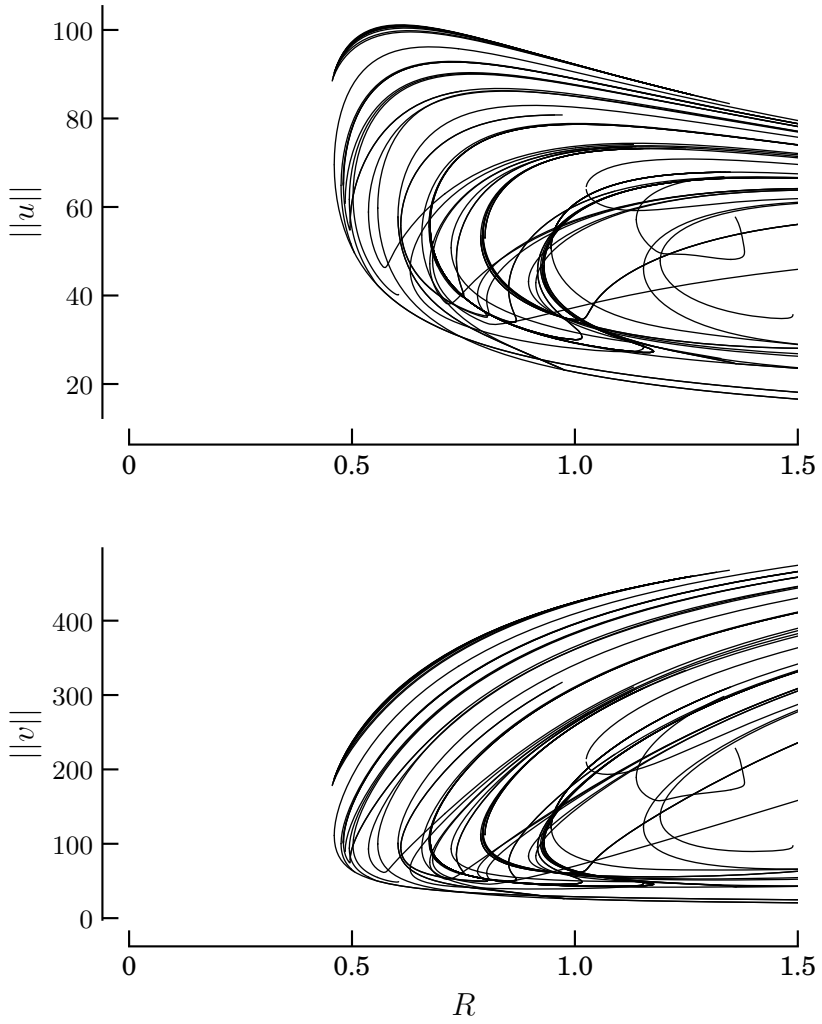

Figure 2.7: Location of the coherent structures as a function of the parameter R. The norms of the field u is plotted on the top graph and the norm of v on the lower graph (these norms were calculated using 400 spatial coordinates for both u and v). The shapes of the diagrams are in agreement with the bifurcation from infinity scenario we would expect to see given that the system of equations was constructed to have this shape. The minimum value of R for which coherent structures were found is $R \approx 0.456$. There are some interesting situations where lower branch states appear to bifurcate again and fold back on themselves.

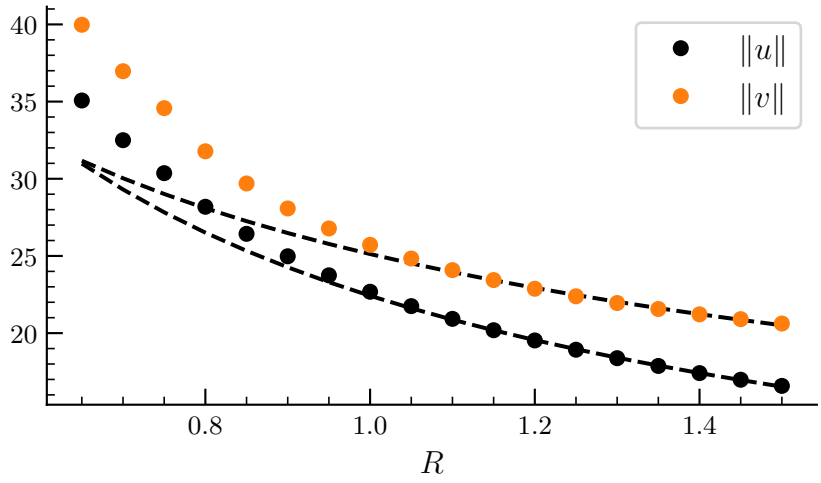

Figure 2.8: The scaling of the lowest branch as a function of R. The points represent the location of the lower branch closest to the laminar state, as defined by the the either the norm of u, v or the sum of the norms. The scalings are $\gamma_u \approx 0.75$, $\gamma_v \approx 0.5$, $\gamma_{uv} \approx 0.6$

2.6.5 LINEAR STABILITY ANALYSIS

We can find the eigenvalues of the finite-difference representation of the Jacobian for the system to conduct a linear stability analysis for the coherent structures that have been found. The analysis confirms that all of the invariant states found are unstable and examples of the eigenvalues for a selection of states is given in figure 2.9. The state which is nearest to the laminar state has three unstable eigenmodes, although it is unclear if this state corresponds to the edge state (the edge state could be a travelling wave or an unstable periodic or relative orbit, but this study has only found invariant states). We can visualise the structure of phase space by plotting the number of unstable modes as a function of the distance from the laminar state - lower branch states will be closer to the laminar state than upper branch ones. This analysis can be seen (again for $R = 1.0$) in figure 2.10 where we have defined the distance to be the sum of the norms of u and v[2]. We see that there is an interesting profile to this figure, with the most unstable states being those approximately in the middle of the diagram. The very furthest states from the laminar flow are actually less unstable than the lowest branch states, and there are two states with only 1 unstable mode. Observation of perturbations above these top branches indicate that there seems to be a region of non-turbulent behaviour; very large perturbations first decay steadily towards the turbulent region before they enter the region of the more unstable states where chaos proper occurs. These top branches could form an edge of chaos on

[2]The ordering of states changes slightly if we use the norm of u or the norm of v or the sum to measure distance, but the overall structure is the same.

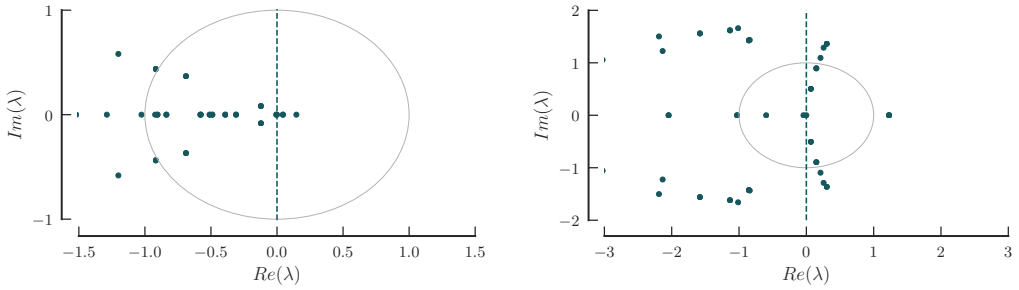

Figure 2.9: Calculated eigenvalues for two different coherent structures, both at $R = 1.0$ with real components on the x axis and imaginary components on the y axis. Circle with radius 1 and line at real part 0 drawn as a guide to the eye. The left had plot corresponds to the state which is closest to the laminar state (by norm of u and norm of v) and has three unstable eigenvalues. On the right is one of the states with highest number of unstable modes, with 20 unstable modes.

the other side from the one usually discussed, an upper bound on the distance of the chaotic region phase space from the origin. We will see an example of this large perturbation non turbulent behaviour in a moment. To my knowledge these relatively stable top branch states have not been found with regard to a subcritical fluid flow, and whether this is because they are not there or because they haven't been found is unclear.

By repeating this analysis for all values of R which we have found coherent structures for we can produce a combined bifurcation diagram, as seen in figure 2.11, which more clearly shows that there is possibly some kind of similarity between the lowest branches and the uppermost branches.

2.6.6 BOUNCING BEHAVIOUR

In order to see what dynamical role the coherent structures have in the relaminarisation process it is useful to have a way to visualise the phase space, and the trajectory of the system through the phase space. The problem is that the phase space is $N \times N$ dimensional, where N is the number of spatial points used to approximate the PDE; in the continuum limit it is infinitely dimensional in u and v. Therefore we require some way to reduce the dimensionality of the system. We do this by using the norms of u and v as coordinates, projecting the system down to a 2-dimensional one. If we iterate in time and follow the system through this reduced phase space we can create phase portraits like the one in figure 2.12a. By plotting the norms of the coherent structures found at the same value of R as the one which the trajectory was produced at, we can get an idea for the relationship between the structures and the dynamics. The coherent structures form a kind of skeleton structure upon which the

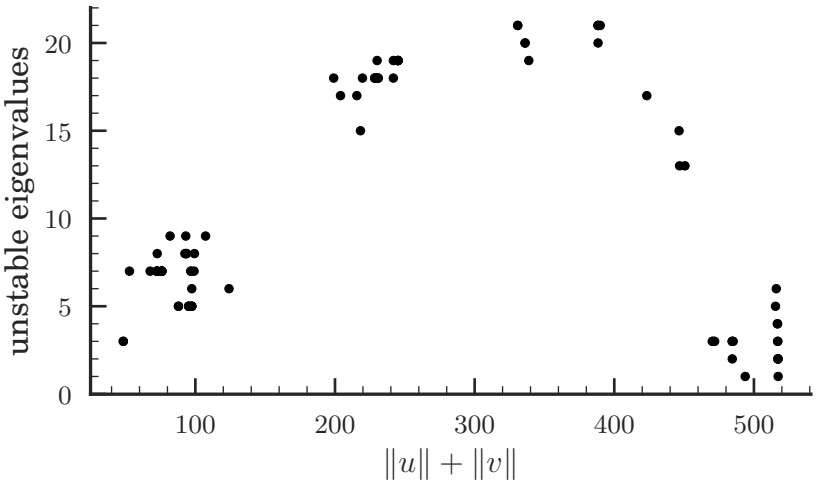

Figure 2.10: The number of unstable eigenvalues for all the coherent structures found at $R = 1.0$ plotted against the sum of the norms of the fields u and v. There are roughly three different kinds of structure, the lower branches, the upper branches and the "top" branches. The "top" branches are the group of states in the lower right hand corner of the figure, corresponding to large amplitude perturbations with very few unstable modes (as low as having only one unstable mode). These states act as some kind of upper bound on the amplitude of the system.

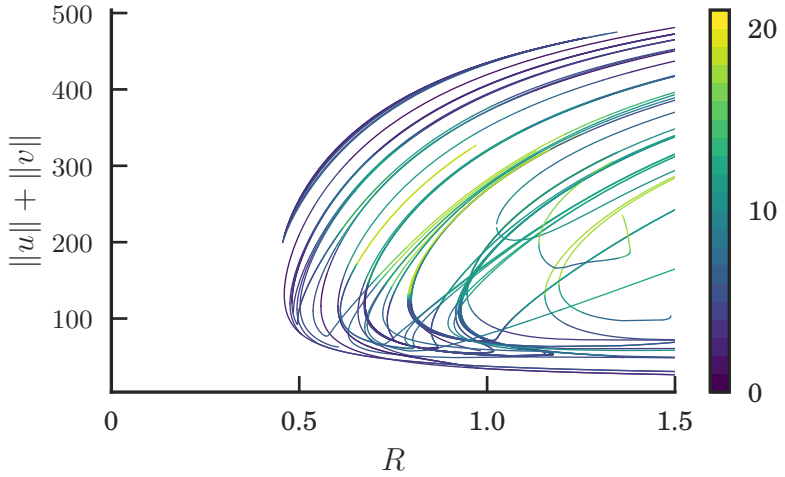

Figure 2.11: The sum of the norms of u and v for coherent structures as a function of R. The colour indicates the number of unstable modes, as per the colorbar on the side. As R increases, more coherent structures are created, and the phase space grows in complexity.

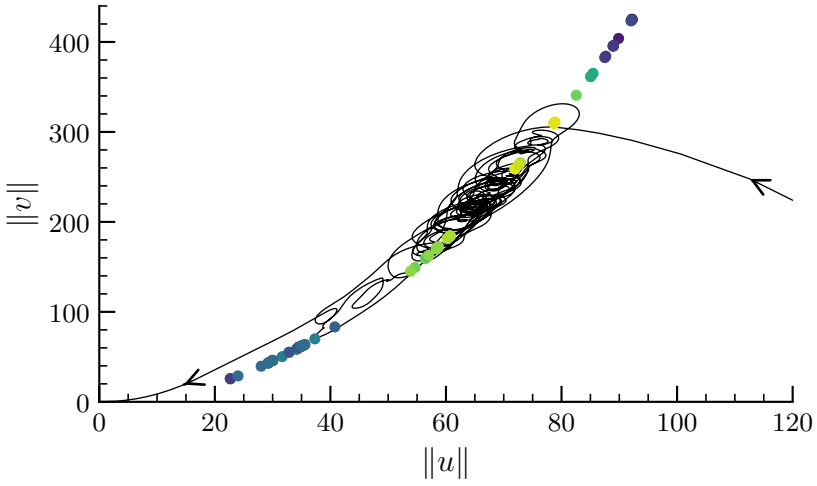

(a) Example phase portrait for the system, plotting the norm of v against the norm of u at $R = 1.0$. The location of the coherent structures are marked with colour corresponding to the number of unstable eigenvalues, as per the scale in figure 2.11. The system can be seen to bounce between the upper branch states before attempting to relaminarise. The lower branch states represent a barrier to relaminarisation. While the very uppermost branches appear to play little role in the dynamics.

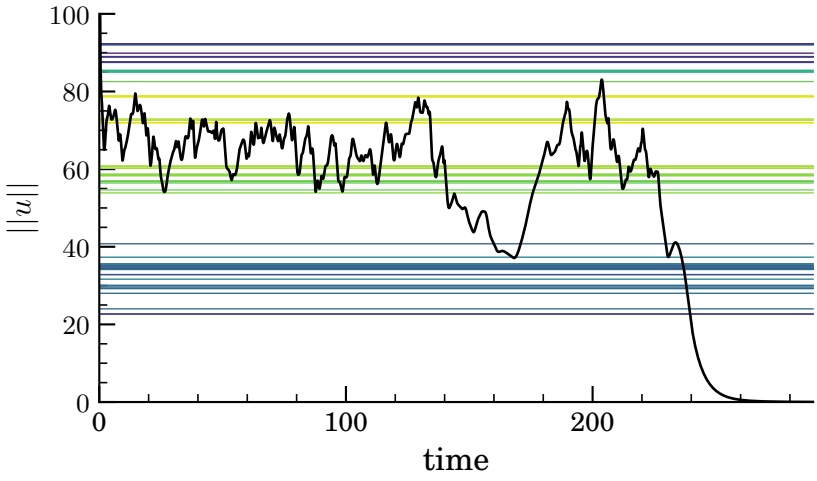

(b) The same run as above, but this time plotting the norm of u against time. The barrier role of the lower branches is even more apparent in this figure.

Figure 2.12: Two figures highlighting the different dynamical roles played by the upper and lower branch states at $R = 1.0$.

trajectories lie, and there seems to be a different dynamical role being played by the upper branches and the lower branches, as can be seen in the figure, where colour is used to represent the number of unstable modes, using the same scale as figure 2.11. The system spends the vast majority of its time in the region occupied by the upper branches, suggesting that there is a complex web of trajectories in this area of phase space, which does not easily permit the system to leave.

The role of the lower branches seems to be different; they act as a kind of barrier to relaminarisation, from which the system can 'bounce' off or which the system can 'miss' and therefore relaminarise. This behaviour is perhaps easier to see in figure 2.12b , where the norm of u has been plotted against time. There are a handful of times where the norm of u dips below the region occupied by the upper branch states in what seems to be an attempted relaminarisation - these attempts are sometimes repelled by the lower branch states, but the system does always relaminarise. It seems that the upper branch region and lower branch region have phase spaces with a different structure - the lower branch phase space has trajectories which either bounce up or decay, and very few that linger in the region, whereas the upper branch states define a region of phase space with more complexity.

This is very reminiscent of the situation in pipe flow and plane Couette flow.

2.7 DISCUSSION

Part of the Family?. We have shown that this model system of PDEs shares many characteristics with the paradigmatic subcritical flows. It exhibits transient spatiotemporal chaos, with an exponential distribution of lifeitimes. The typical lifetimes scale superexponentially. The system has coherent structures which are created via saddle-node bifurcations, and a 'laminar' state which is linearly stable. The parameter R quantifies the nonlinear interaction and behaves in all the examples above in an analogous way to the way the Reynolds number does in the real flows. It appears that this model belongs in some sense to the same 'family' of chaotic systems as pipe flow and Couette flow, and could therefore act as a toy model for exploring the dynamics of these types of systems.

Lower Branches and DP. As described above, there appears to be roughly three different kinds of states with different dynamical roles. The upper branches, lower branch, and laminar state can each be described has having different behaviour, with the lower branches playing a dynamical role somewhere between that of the upper branches and the laminar state. This is different to the picture usually imagined in directed percolation models, where the system is imagined to be split into either

active or *inactive*. The behaviour of our model is similar to that of parallel shear flows, and so the effect of this additional state on the DP transition scenario is of interest both to this model and to the larger family of related flows, and will be the focus of the next chapter.

2.8 CONCLUSION

An extended version of the Kuramoto-Sivashinsky equation first introduced by Becherer et al. in 2009 has been studied numerically. The system has been shown to share many characteristics with real subcritical flows, namely: a linearly stable laminar profile; and a subcritical transition to spatio-temporal chaos; a chaotic saddle with and 'edge'; and coherent structures embedded in the saddle which organise the chaotic behaviour. The lifetimes of the system were shown to follow a Poisson distribution for most values of the control parameter R. This indicates memoryless decay and suggests the existence of a chaotic saddle. The scaling of the typical lifetimes was found to be superexponential, the same scaling seen in the real flows.

Lastly, the system was probed for coherent structures using a Newton-Raphson method. The coherent structures dictate where in the phase space the system spends most of its time, and play a role in preventing the system from relaminarising. A bifurcation diagram was produced for the system, showing the expected subcritical transition, and increasing complexity with the control parameter R.

From these results a picture emerges of how the dynamics of the turbulence is governed. Unstable coherent structures are fixed points in phase space around which the system's behaviour is organised. The system bounces between upper branch points and makes occasional excursions to the lower branch region. The lower branches can repel the state or allow it to relaminarise.

3 A THREE STATE DIRECTED PERCOLATION MODEL

As discussed in section 1.1.3 , the transition to turbulence in pipe flow and Couette flow has been shown to belong to the Directed Percolation (DP) universality class[35, 49]. The models studied which belong to this class have an 'active' state and an 'absorbing' state which correspond to turbulent and laminar flows respectively. However, the full dynamics of the transition appears to be more complicated given that there are upper and lower branches created together in the bifurcation, and they are linearly unstable in a different manner to each, as seen in the eKSE studied in the previous chapter. A state between fully laminar and turbulent has also been observed in a simulation exploring turbulent-laminar patterns in plane Couette flow by Barkley & Tuckerman [130]. At first glance it may appear possible that the addition of a third intermediate state to the DP formulation may violate the observed universality class of the transition, and in this chapter I will explore if this is true by constructing such a model and measuring the critical exponents - we might not expect the addition of the third state to change the universality class (given the seeming robustness of the universality class), but as we will see it does in fact introduce some non-universal difference to the nature of the transition which could possibly allow an experimental check of the relevance of the third state.

I will begin the chapter with a brief theoretical introduction to DP before introducing the new model and measuring the critical exponents.

3.1 INTRODUCTION

Given that the laminar flow for parallel flows is stable at any Reynolds' number[4], and turbulent puffs can seemingly decay at any Reynolds' number[26] the question naturally arises: does turbulent flow in subcritical systems *ever* become sustained? The answer is *yes*, and the key to understanding how this happens is another behaviour of the puffs.

As well as being able to decay, turbulent puffs have a chance to 'split', producing another puff adjacent to the first[38, 45]. Both the decay and splitting are memoryless processes and the typical timescales for each process scale as a function of the Reynolds number; increasing Re causes the typical lifetime of a puff to increase and the time to split to decrease[37, 44]. Both of these processes scale super-exponentially with Re, indicating that extreme events could be the cause of both processes[33]. At a certain value of Re (around 2040 in pipe flow) these typical time scales become comparable, indicating that a puff is about as likely to split before it decays, allowing sustained turbulence.

This competition between death and the production of offspring is reminiscent of the Directed Percolation system often studied in non-equilibrium statistical physics[41]. DP models have been found numerically to capture features of the transition in pipe flow[47] and plane Couette flow[43] and in experiments in plane Couette flow[35] and channel flow[48] and numerical observation of the 2D DP transition in a planar shear flow[51].

Further evidence that the transition is analagous to a thermodynamic phase transition is the observation of scale invariance at the critical point in Couette flow[131] and the success of a predator-prey model (asymptotically equivalent to DP)[97] in reproducing the phenomenology of pipe-flow turbulence.

The success of this framework is striking, but something that is seemingly missing from this description is the differing roles played by the upper and lower branch states in the relaminarisation process. In this chapter I will introduce a DP model which attempts to capture this role, but I will first give a brief introduction to Directed Percolation and the relevant theoretical background I will use in the calculations.

3.1.1 DIRECTED PERCOLATION

Directed Percolation is a prototypical example of a non-equilibrium phase transition[132], as prominent as the Ising model is in equilibrium statistical mechanics[133] and as its name suggests can be thought of as describing the percolation of a fluid through a porous medium if that fluid is constrained in which direction it can move, for example if it is under the influence of gravity. Consider a two dimensional centred square lattice of points which can be connected by bonds. Each bond can be considered 'active' with probability p or 'inactive' with probability $1 - p$; the connection to percolation comes from the analogy that these bonds are channels which can connect pores in the medium - a fluid can move through open channels but not through closed channels. This model of DP is called bond DP (in contrast to site DP where it is the sites which are active or inactive with some probability,

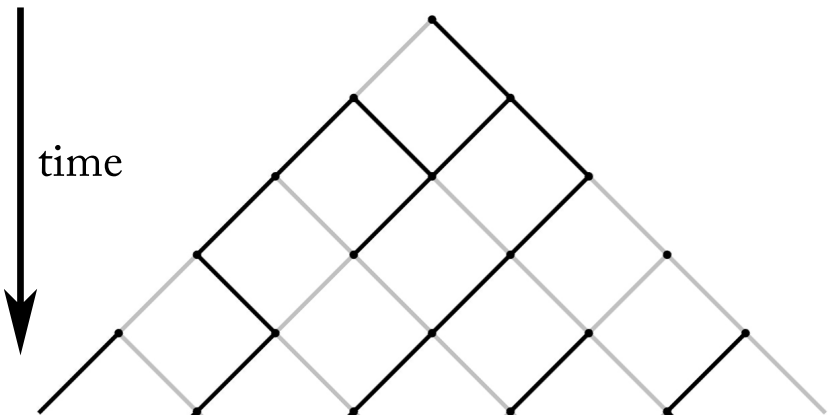

Figure 3.1: A cartoon of bond directed percolation. A lattice of sites can be connected (black lines) or disconnected (grey lines) with some probability. Progress is only allowed in one direction, which can be though of as either gravity or time. At a critical value of the bond activity probability there is a phase transition which allows for the existence of infinite progress.

and fluid can flow from active site to active site). In isotropic percolation the fluid in a pore can move through any bond connected to that pore[1] but in DP the fluid can only move in one direction, as if under the influence of gravity. A schematic of this system can be seen in Fig. 3.1.

We define an 'active cluster' to be a collection of active bonds connected to each other. Below some critical bond activation probability, p_c, active clusters of sites on the lattice always have a finite downstream extension. For probabilities above the critical point the system undergoes a phase transition which allows the existence of infinitely long clusters. For the bond DP process sketched above the critical point occurs at around $p = 0.6447$ [135].

The direction analogous to gravity entails a strict causal direction (as well as something like a light cone of causal influence) which suggests thinking of the direction as a temporal rather spatial dimension. In this way of thinking we substitute the two dimensional square lattice for a 1 dimensional lattice which can evolve stochastically in time. At each time step there is a probability that an active state will continue left or right - the system can then be updated to reflect the new configuration generated by the stochastic process and the update procedure repeated for an arbitrary number of time steps.

We can think of this update scheme of as a reaction-diffusion system with the following processes:

- *Death:* Active site $\rightarrow$ no active neighbours

[1] Isotropic percolation is exactly solvable[134]

- *Diffusion:* Active site $\rightarrow$ one active neighbour
- *Offspring:* Active site $\rightarrow$ two active neighbours
- *Coalescence:* Two neighbouring active sites $\rightarrow$ one active site between them.

This temporal, stochastic behaviour begins to make the link to spatiotemporal intermittency and the turbulence transition more apparent. Turbulent patches and puffs can behave in analagous ways to this update scheme; they can die, survive, split, and coalesce. The precise details of the behaviour should not matter when determining the universality class; in part due to scale invariance at the transition.

3.1.2 SCALE INVARIANCE AND POWER LAWS

Phase transitions in general can be identified by scale invariance which occurs at the transition point [136] and this is also true of DP.

By definition, below the critical point all clusters eventually die, so if we were to 'zoom out' sufficiently the system would seem to decrease in density. On the other side of the transition, the proportion of clusters which are infinite will appear to increase as the smaller finite clusters begin to disappear from view. In this way, a change in the scale of observation is like a movement either away or towards the critical point (for zooming out or zooming in respectively). The critical point is the exact balance point of these two competing behaviours and so at the critical point zooming either in or out does not change the appearance of the system and there are structures at all length scales. This property is known as scale invariance and has been incredibly useful in the study of phase transitions [136]. For example, it constrains the way that physical properties can scale near the transition and also is the reason that the microscopic details of the interaction are unimportant to the critical behaviour; zooming out sufficiently far will remove those interactions.

One important consequence of the scale invariance is the appearance of power law behaviour in physical properties of the system. A function of the form $f(x) = ax^b$ is trivially scale invariant. Scaling the argument by constant λ gives:

$$f(\lambda x) = \lambda^b f(x) \tag{3.1}$$

When talking about phase transitions near criticality, if x measures the distance from the critical point then b is known as a *critical exponent*. These exponents do not depend on microscopic details of the interaction and can be used to sort transitions into robust categories of related models which have the same exponents. Directed Percolation is one such category (universality class). The aim of this chapter is to

show that a novel three state DP model also belongs to the DP universality class. Therefore we must measure the critical exponents.

In order to explain the method I used to measure the critical exponents I will now introduce some notation and definitions which are based on those used in the textbook *Non-equilibrium Phase Transitions: Volume 1 - Absorbing Phase Transitions* [137] which can be consulted for a more thorough treatment of these topics.

3.1.3 ORDER PARAMETERS & CORRELATION LENGTHS

Order Parameters. The two phases in a phase transition are distinguished by an order parameter - some quantity that is zero in one phase and non-zero in the other. With that in mind there are actually two quantities we could use as order parameters:

1. The probability that a cluster generated from a single point will survive until $t = \infty$. We will denote this parameter P_{perc}

2. The *steady state* density of the system when started with homogeneously active initial conditions, i.e. the density after infinite time. Below the transition we expect the lattice to eventually become completely empty but above the transition we should see a finite density of active states. The proportion of lattice sites active after infinite time is therefore an order parameter which we shall call ρ_∞.

Each of these parameters has an associated critical exponent and we expect them to scale above the critical point as follows:

$$\rho_\infty \sim \tau^\beta \tag{3.2}$$

$$P_{perc} \sim \tau^{\beta'} , \tag{3.3}$$

for some constants β and β'. The quantity τ is analogous to the reduced temperature used in equilibrium phase transitions and is a measure of the distance of the control parameter from the critical point:

$$\tau \equiv \frac{r - r_c}{r_c} \tag{3.4}$$

As it turns out, DP has a symmetry which causes the two order parameters to be proportional to one another, the so called 'rapidity reversal symmetry' [137]. If the order parameters are proportional to each other, it follows that the two critical exponents are identical i.e. $\beta = \beta'$, reducing the number of exponents needed to

characterise the system. Later in this chapter I will show that our new system also has the rapidity reversal symmetry.

Correlation Lengths. In equilibrium phase transitions there is typically a correlation length ξ which diverges at the critical point. The differing nature of time and space in DP means that there are in fact two correlation lengths, and these correlation lengths each have an associated critical exponent:

1. The spatial correlation length $\xi_\perp$ which diverges like $\xi_\perp \sim |\tau|^{-\nu_\perp}$ and characterises the spatial length of inactive domains.

2. The temporal correlation length $\xi_\parallel$ which diverges like $\xi_\parallel \sim |\tau|^{-\nu_\parallel}$ and characterises the time over which a site will remain in the inactive state.

The three components β, $\nu_\parallel$ and $\nu_\perp$ are all that are needed to fully characterise the system - all the other exponents can be calculated from these three using scaling relations. Therefore the calculation of these three exponents is the main goal of this chapter.

3.1.4 DATA COLLAPSE

One way to think of this scale invariance is that measurable thermodynamic properties can be expressed as 'generalised homogeneous functions' [137]. These are functions (with variables x_i) where scaling the function by a positive number λ can be understood as a dilation of the coordinates by powers of the variables:

$$\lambda f(x_1, x_2, ...) = f(x_1\lambda^{s_1}, x_2\lambda^{s_2}, ...)\,, \tag{3.5}$$

for all positive values of λ. Functions of this form are useful (in part) because they permit us to cause data collapses by judicious use of scaling functions. For example, if we choose $\lambda = |x_i|^{-1/s_1}$ then we get the following relation:

$$f(x_1, x_2, ...) = |x_i|^{1/s_1}\tilde{f}(1, |x_i|^{-1/s_1}x_2, ...)\,, \tag{3.6}$$

where the function $\tilde{f}$ is known as the 'scaling function'. This means that if we plot $|x_i|^{-1/s_1}f(x_1, x_2, ...)$ for a range of values of x_1 we should see that the data all collapse, because this equation should not depend on x_1. We can therefore use this method to measure the exponent, since the collapse will only occur if we use the correct scaling exponent.

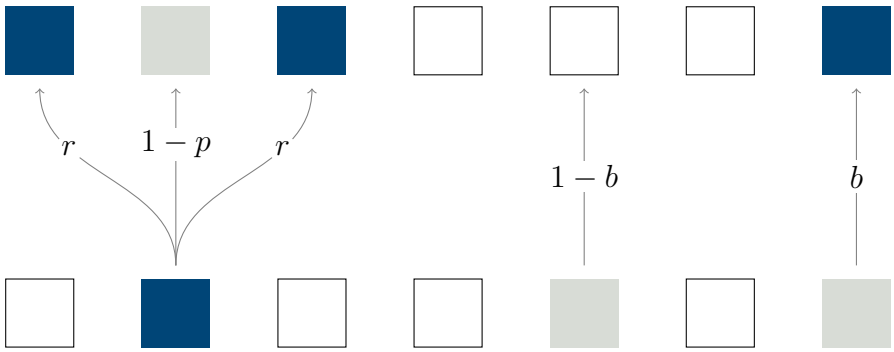

Figure 3.2: Graphical depiction of the directed percolation model used. Dark squares represent upper branch states and light squares represent lower branch states. Upper branch states can either survive (with probability p) or decay to a lower branch state (with probability $1 - p$); they can also infect neighbouring states (with probability r). Lower branch states have only two options: they can bounce back to an upper branch state (with probability b) or they can decay to the absorbing state (with probability $1 - b$).This new behaviour only adds one parameter to the traditional directed percolation.

3.2 THE THREE-STATE MODEL

The three-state DP model we introduce here is similar to the model studied in the 2012 paper *Directed Percolation Model for Turbulence Transition in Shear Flows* [96], but with the addition of a third state. This third state is intermediate between the active and absorbing states and is motivated by the apparently different dynamical roles played by the upper and lower branch states in the extended Kuramoto-Sivashinsky equation studied in the previous chapter (and in subcritical chaotic systems generally).

The lower branch states act as a separation between the fully turbulent upper branch regime and the laminar state [84] and we have seen in the previous chapter that they seem to act as a barrier to relaminarisation. Motivated by this it is prudent to ask what effect including these states in the DP description of turbulence transition would have. We observed in the eKSE that the system does not linger in the vicinity of these lower branch states, which seem to act as a repeller (a model proposed by Barkley [46] also takes the approach of having repelling lower branch states). A schematic diagram of the behaviours of the different states is shown in Fig. 3.2 while the update algorithm can be seen in Alg. 1; the behaviours of the three states can be characterised as follows:

Upper Branch. Has two different behaviours:

- *Survival.* The upper branch state can persist with probability p. If it does not survive it can decay, but only to the intermediate state. We do not allow upper branch states to decay directly to laminar states.

- *Infection.* Upper branch lattice sites can infect neighbouring lattice sites, with probability r. It can infect left and right independently, and with equal probability. An upper branch state which is going to decay can still infect neighbouring sites. (A simultaneous model, inspired by [96]). A site which is decaying and being infected at the same time will be upper branch (infection has higher priority than decay).

Lower Branch. Can only die or bounce, cannot persist in this state. The motivation for this behaviour is the observation that in the eKSE we never see the system lingering in the vicinity of these states - the system will either "bounce" back to the upper branches or else decay. We denote the probability for these cells to "bounce" as b.

Laminar. The absorbing state of the model. The state stays inactive unless it is infected by a neighbouring site. In the subcritical transitions we are attempting to model the laminar state is linearly stable and so cannot spontaneously generate turbulence without a finite-sized perturbation.

A Note on Parameters. All of the simulations follow a similar approach to varying the three parameters p, r, b. Following the lead of [96] we set the survival probability $p = 0.7$ as a fixed parameter, and it is never varied. We then allow the infection probability r to take any value between 0 and 1, depending on what is relevant to the quantity we are trying to measure. All calculations are then repeated for ten values of the bounce probability, $b \in \{0.0, 0.1, ...0.9\}$.

Parameter	Description	Values Considered
p	Survive	0.7
r	Infect	Any value between 0 and 1 as needed
b	Bounce	0.0, 0.1, 0.2,...,0.9

Table 3.1: The three parameters of the model.

Algorithm 1 Lattice Update Method

```
1:  x ← create initial conditions
2:  for each timestep do
3:      y ← fully laminar array                    ▷ Hold update without overwriting x
4:      for n ∈ {0, 1, ..., N − 1} do
5:          if x_{n−1} = 2 and rand < r then       ▷ Infected from left
6:              y_n ← 2
7:          else if x_{n+1} = 2 and rand < r then  ▷ Infected from right
8:              y_n ← 2
9:          else if x_n = 2 then                   ▷ Site is upper branch
10:             if rand < p then                   ▷ Survival
11:                 y_n ← 2
12:             else                               ▷ Decay to lower
13:                 y_n ← 1
14:         else if x_n = 1 then                   ▷ Site is lower branch
15:             if rand < b then                   ▷ Bounce
16:                 y_n ← 2
17:     x ← y
```

The algorithm for updating the lattice. Note that due to the periodic boundary conditions the subscripts are calculated modulo N. Wherever rand *is written a random number is generated from a uniform distribution between 0 and 1.*

3.3 MEAN FIELD THEORY

Before I introduce the numerical simulations I will first consider a mean field approximation of the system. We look to find the probability that a given site $x_n(t)$ is in the upper branch ($x_n = 2$) state. There are three possible reasons that this could be the case:

(A) The site $x_n(t-1)$ was in the upper branch state and survived.

(B) One of the adjacent sites $x_{n\pm1}(t-1)$ was in the upper branch and infected $x_n(t)$.

(C) The site $x_n(t-1)$ was in the lower branch state and bounced back up.

We will denote the probability of any event X occurring as $P(X)$, so we wish to find $P(x_n(t) = 2)$. We will denote the probability of two events happening at the same time as $P(X|Y)$. The total probability that the state is in the upper branch state is the sum of the probabilities $P(A)$, $P(B)$ and $P(C)$ minus the probabilities of more than one infection occurring at the same time. Therefore we are trying to calculate:

$$P(x_n(t) = 2) = P(A) + P(B) + P(C) \\ - P(A|B) - P(A|C) - P(B|C) + P(A|B|C) \quad (3.7)$$

Now, we know that it is impossible for A and C to both occur because they have incompatible requirements: A requires $x_n(t-1) = 2$ but C requires $x_n(t-1) = 1$. Therefore, $P(A|C) = P(A|B|C) = 0$. We will treat the other probabilities as being independent (in the mean field limit) so we can set $P(A|B) = P(A)P(B)$ and $P(B|C) = P(B)P(C)$. Therefore we have:

$$P(x_n(t) = 2) = P(A) + P(B) + P(C) - P(A)P(B) - P(B)P(C) \quad (3.8)$$

We will now use a mean-field approach to calculating each of the relevant probabilities. This means that $P(x_n(t) = 2)$ loses its time and position dependence, so we will replace it with the variable q.

$P(A)$ is the probability of the state being in the upper branch state due to survival. In the mean field limit this is simply the probability that the previous cell was upper

branch multiplied by the probability that it survived. In the mean field limit all cells have equal probability to be upper branch (q), therefore:

$$P(A) = pq \tag{3.9}$$

$P(B)$ is the probability of being infected from the left or the right, and is the sum of the probabilities that it is infected from each side, minus the probability that the cell is infected from both sides. The probability that a cell is infected is rq, therefore:

$$P(B) = rq + rq - (rq)(rq) = 2rq - r^2q^2 \tag{3.10}$$

$P(C)$ is the probability that the cell has bounced up from a lower branch state. In order to calculate this we will need to know the probability that a cell is in the lower branch state (again, we are in the mean field limit so we can say this is the same for all cells). In order for the cell to be in the lower branch state, there are three things that all need to be true. The cell *was* upper branch (probability q); the cell decayed (probability $1 - p$); the cell was *not* infected from either the left or the right (probability $(1 - rq)^2$. Therefore the probability of the cell being in the lower branch state is $q(1 - p)(1 - rq)^2$ and so the probability of bouncing is:

$$P(C) = bq(1 - p)(1 - rq)^2 \tag{3.11}$$

Substituting these expressions into equation 3.8:

$$\begin{aligned} q = pq + 2rq - r^2q^2 + bq(1 - p)(1 - rq)^2 \\ - (2rq - r^2q^2)(pq + bq(1 - p)(1 - rq)^2) \end{aligned} \tag{3.12}$$

This equation does in fact have an analytic solution although writing it out in full here is not particular illuminating. A plot of the predictions it makes for a range of values of the various parameters can be seen in Fig. 3.3. These curves were produced by solving for q numerically with a Newton method. It is worth noting that setting $b = 0$ recovers the mean field predictions from [96]. To compare these predictions with the true value we will now discuss the simulations starting with homogeneous initial conditions.

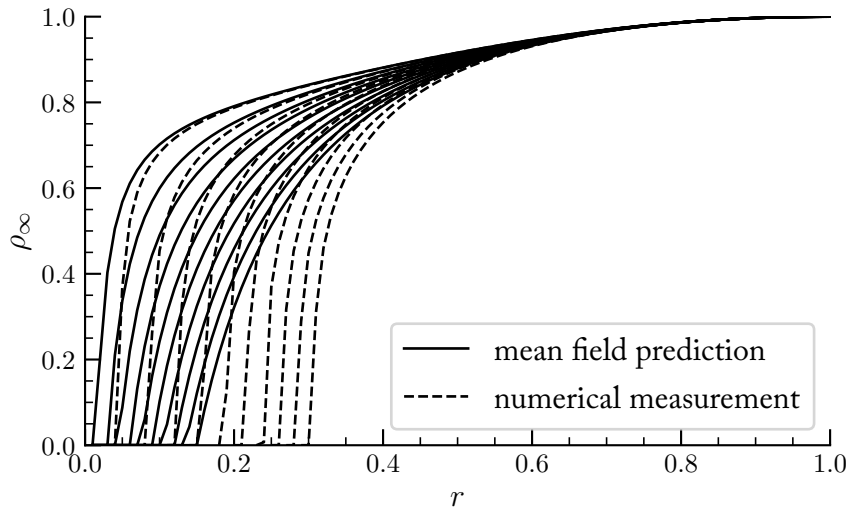

Figure 3.3: A comparison of the mean field theory prediction and the numerically measured value of the turbulent fraction (after infinite time) as a function of the infection probability, r. The measurement is made for a range of values of the bounce probability $b = 0, 0.1, ..., 0.9$, with the critical infection probability r_c moving to the left as b increases.

3.4 HOMOGENEOUS INITIAL CONDITIONS

There are several different initial conditions we may wish to study, but we will focus on the two introduced in section 3.1.3 for calculating the critical exponents. We can have the system begin in a homogeneously active state or in a state with a single active seed. I have performed simulations of the system with both types of initial condition to calculate the critical exponents and will begin by discussing the homogeneous initial conditions.

The lattice size used for these simulations needs to be large in order for the finite size effects induced by the finite size of the lattice to be small enough as to be negligible; the lattice used in these simulations had 200,000 sites.

3.4.1 FINDING THE CRITICAL POINT

The first thing to measure is the critical infection probability, r_c. This is the value at which the lifetime of the 'turbulence' diverges, and there is a transition to a persistent state. Another way to think of this is that it is the point at which the system transitions from zero to non-zero steady state density. We will call this density ρ_∞. In order to calculate this I used a two-step process, an initial sweep of all values of r to locate the approximate location of the transition, followed by a more careful analysis of the curves in the vicinity of the transition.

b	r_1	r_2	r_3	r_4	r_5	r_6	r_7	r_8	r_9	r_{10}
0.0	.30630616	.306428928	.306551696	.306674464	.306797232	.30687	.30688	.30689	.3069	.30691
0.1	.28689506	.287010048	.287125036	.287240024	.287355012	.28742	.28743	.28744	.28745	.28746
0.2	.26580732	.265913856	.266020392	.266126928	.266233464	.26629	.2663	.26631	.26632	.26633
0.3	.2427635	.2428608	.2429581	.2430554	.2431527	.24319	.2432	.24321	.24323	.24324
0.4	.2176139	.21770112	.21778834	.21787556	.21796278	.218	.21801	.21802	.21803	.21804
0.5	.18998926	.190065408	.190141556	.190217704	.190293852	.19032	.19033	.19034	.19035	.19036
0.6	.15952032	.159584256	.159648192	.159712128	.159776064	.15979	.1598	.15981	.15982	.15983
0.7	.12580788	.125858304	.125908728	.125959152	.126009576	.12601	.12602	.12603	.12604	.12605
0.8	.08838288	.088418304	.088453728	.088489152	.088524576	.088555	.088556	.088557	.088558	.088559
0.9	.0466565	.0466752	.0466939	.0467126	.0467313	.046745	.046746	.046747	.046748	.046749

r_{11}	r_{12}	r_{13}	r_{14}	r_{15}	r_{16}	r_{17}	r_{18}	r_{19}	r_{20}	r_{21}
.30692	.30693	.30694	.30695	.30696	.30697	.307042768	.307165536	.307288304	.307411072	.30753384
.28747	.28748	.28749	.2875	.28751	.28752	.287584988	.287699976	.287814964	.287929952	.28804494
.26634	.26635	.26636	.26637	.26638	.26639	.266446536	.266553072	.266659608	.266766144	.26687268
.24325	.24326	.24327	.24328	.24329	.2433	.2433473	.2434446	.2435419	.2436392	.2437365
.21805	.21806	.21807	.21808	.21809	.2181	.21813722	.21822444	.21831166	.21839888	.2184861
.19037	.19038	.19039	.1904	.19041	.19042	.190446148	.190522296	.190598444	.190674592	.19075074
.15984	.15985	.15986	.15987	.15988	.15989	.159903936	.159967872	.160031808	.160095744	.16015968
.12606	.12607	.12608	.12609	.1261	.12611	.126110424	.126160848	.126211272	.126261696	.12631212
.08856	.088561	.088562	.088563	.088564	.088565	.088595424	.088630848	.088666272	.088701696	.08873712
.04675	.046751	.046752	.046753	.046754	.046755	.0467687	.0467874	.0468061	.0468248	.0468435

Table 3.2: Table showing the values of infection probability used for each value of bounce probability. The values highlighted grey were used the find the critical point, and the dynamical exponent α as described in the text. The other values were used when measuring the data collapse and were calculated as $r_c \pm 1\%$.

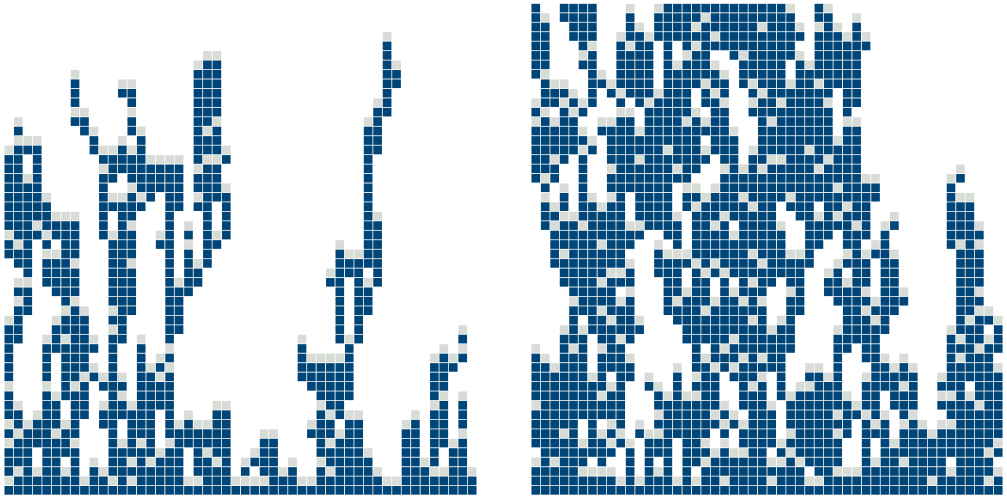

Figure 3.4: Plots of the time evolution of the system for typical runs below and above the critical point, starting from a fully occupied lattice at the bottom (direction of time is upwards). Dark blue squares represent 'upper branch' states and light grey represent 'lower branch' states. Below the critical point the system always dies within a finite time but above the critical point there is sustained 'turbulence'.

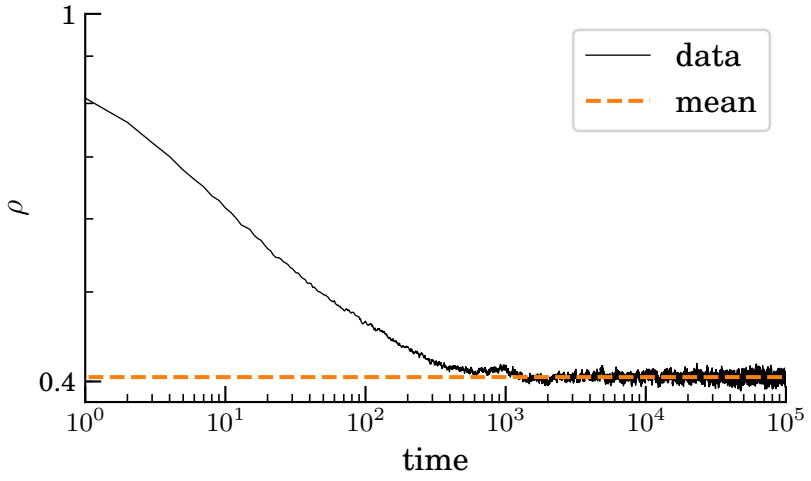

Figure 3.5: An example plot of the density as a function of time, in this case at $b = 0.5$, $r = 0.2$ on a log-log plot. Also shown is the value used for the estimation of ρ_∞. Only the final decade is considered for the fit, and the density is more or less constant here, so the mean of this quantity can be used to get at least the rough location of the transition.

Initial Sweep. In order to calculate ρ_∞ we simulated the system for maximum time of $t = 100,000$. The initial condition for each run was a fully active (upper branch) lattice. The density at timestep t is given by the number of upper branch states divided by the lattice size N. By averaging over many runs (100 for each data point) we can then calculate $\rho(t)$ for a range of values of r at each b. To get ρ_∞ from $\rho(t)$ we first calculate the mean of the points from $t = 10,000$ to $t = 100,000$.An example of one of these curves at $b = 0.5$ and $r = 0.2$ (with the associated mean) can be seen in figure 3.5. The fact that the density stabilises at a value larger than zero indicates that this is after the transition. This procedure was repeated for $r \in \{0.00, 0.01, ...0.99\}$ and the results can be seen (and compared with the mean field result) in Fig 3.3. Using this method the approximate position of the critical point is easy to see: below the critical point it is zero, and there is a fairly sharp increase in the density near the critical point. However, due to the finite size of the lattice and finite time of evolution there is a roundedness to the curves near the critical point and so there is a fuzziness to the location of the critical point. Given how important the exact location of the critical point is to the method of calculating the exponent it is worth taking some time to refine our estimation of this.

A Closer Look. This method was used to find the approximate value of r_c for each b, but in order to find it more accurately we used the fact that at criticality, scale invariance causes $\rho(t)$ to decay as a power law [137]. So we have:

$$\rho(r_c, t) \sim t^{-\alpha}\,, \tag{3.13}$$

for some dynamical exponent α (we will see later how this exponent relates to the three exponents we are aiming to measure). How can we use this fact to obtain a value for r_c? Verifying and extracting exponents from suspected power-law data is a non-trivial undertaking and the problem is confounded further by the fact that simply measuring the exponent of a given curve is not a satisfactory method because it requires us to be exactly at the critical point, which is not known a priori. If we could find some number which represents the deviation of the curve from a power-law then we could solve the problem by finding the value of r which minimises this deviation. The method I applied was to look for some function $f(r, t)$ such that:

$$\rho(r, t) \sim t^{-\alpha} f(r, t) \tag{3.14}$$

We can then find the value of r at which $f(r, t) = 1$ (for all t) which will be the location of the true power-law behaviour. This will then imply that we have found the critical infection probability and we will simultaneously have measured

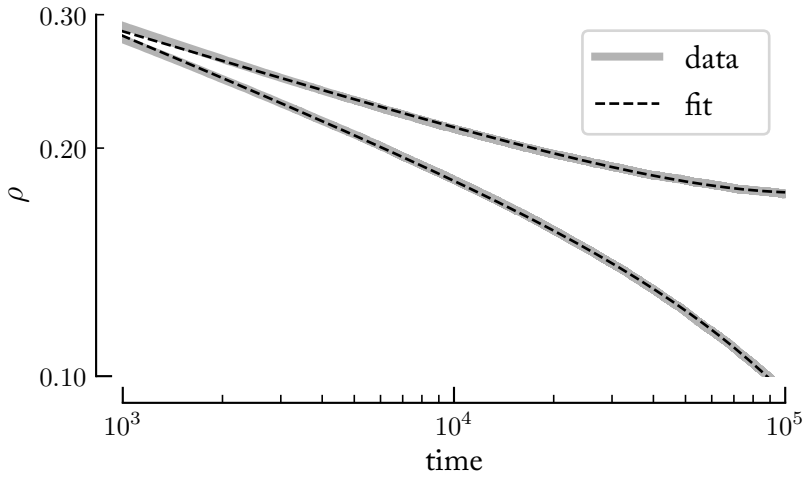

Figure 3.6: Example of density curves on a log-log plot, together with the fit obtained using equation 3.15. The two curves plotted here are both at $b = 0.5$, with the lower curve at $r \approx 0.1900$ and the upper curve at $r \approx 0.1908$. The curve above the critical point was found to have equation $\rho(t) \approx 0.7t^{-1.31}\exp(0.0000012)$ while the one below the critical point had equation $\rho(t) \approx 0.99t^{-1.8}\exp(-0.0000026)$ The fact that one curve veers up while the other veers down indicates that the critical point is somewhere between these values of r, and the fits are used in the calculation of r_c as explained in the text.

the dynamical exponent α. A candidate for the function is simply $f(r,t) = e^{A(r)t}$, which would make the equation to fit the curves:

$$\rho(r,t) \approx Kt^{-\alpha(r)}e^{A(r)t}\,, \tag{3.15}$$

for some A. By measuring $A(r)$ and noting that $f(r_c) = 1$ implies that $A(r_c) = 0$ we can therefore find r_c. It is important to note here that we allow the value of α here to vary with r but the true value of α only occurs at r_c. A starting point of $t = 1,000$ is used in all of the calculations in this chapter. In order to fit these curves the `curve_fit` procedure from Scientific Python's `optimize` package, which (when provided with bounds for the parameters) uses a trust region reflective root find algorithm [138, 139]. This function did quite a good job of fitting the curves and examples of these fits can be seen in fig. 3.6. This method of fitting the curves seems to work quite well and as far as I know is fairly novel, I will discuss the method in more detail in section 3.7.1 of this chapter. The curve fitting package returns the covariance matrix of the parameters which can be used to calculate the uncertainty in the fit and eventually in the measured exponent.

By fitting the density curves we end up with two sequences of measurements,

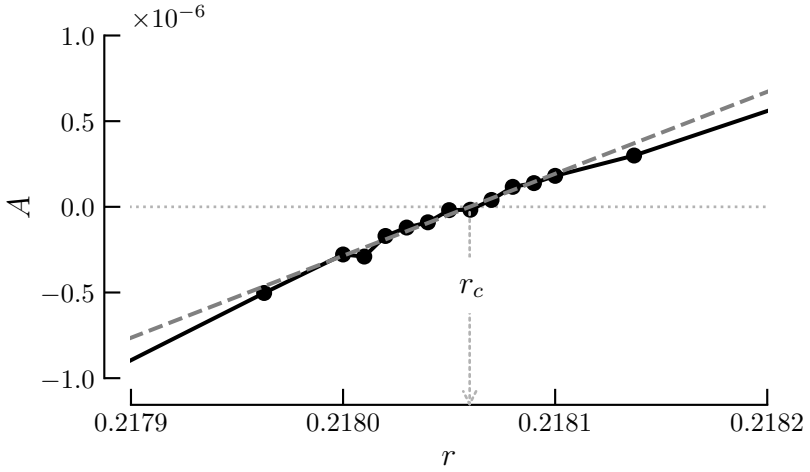

Figure 3.7: Measurement of r_c (for $b = 0.4$) by finding the zero-crossing of A. The orange line is the linear fit of the points and where this line crosses the r axis is deemed to be the critical infection probability. (Note: the first and last points seen on this graph were not included in the fitting procedure and are actually part of the wider set of points from the initial sweep, they are included for interest as it seems that this curve could in fact be quadratic rather than linear - see section 3.7.1 for further details.)

the fitted values of $\alpha(r)$ and $A(r)$. We can then fit a straight line to $A(r)$ as a function of r (appropriately weighting A by the uncertainty of that measurement). This step is done with scientific python's `polyfit` procedure which can also return the covariance matrix. An example of one of these straight lines can be seen in fig. 3.7. It is interesting to note that included density curves from further from the critical point seems to indicate that a linear fit might not be the best way to go about this, we shall come back to this question later. We now have a line of equation $A = mr + c$ and we then we simply set $A = 0$ and solve for r_c to get $r_c = -c/m$. The uncertainty of this is then calculated with the expression:

$$\sigma_{r_c} = r_c \sqrt{\left(\frac{\sigma_m}{m}\right)^2 + \left(\frac{\sigma_c}{c}\right)^2 - 2\frac{\sigma_{m,c}}{mc}}\,, \tag{3.16}$$

where σ_x is the error in variable x and $\sigma_{x,y}$ is the covariance between x and y. We now have a measure of r_c and associated uncertainty for each value of b - the next step is to find α given this critical point.

Now that we have r_c we can use the sequence of $\alpha(r)$ to find the true value of α, being just the point at which the line of $\alpha(r)$ crosses the r_c line, as shown in figure 3.8. This is done in a very similar manner to finding r_c, by fitting a straight line with

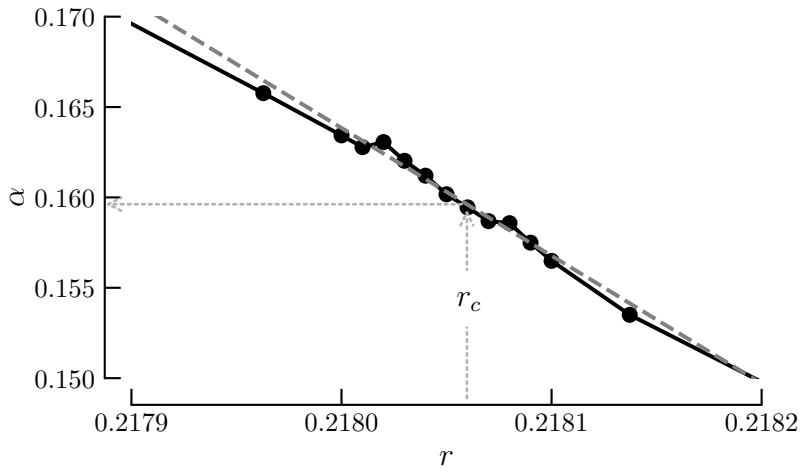

Figure 3.8: Calculation of α (for $b = 0.4$) using r_c and the fits of density curves using eq. 3.15. Again, the orange line represents the linear fit.

scientific python's `polyfit` procedure and then plugging in the value of r_c in the expression. The uncertainty in α is given by the expression (assuming all covariances are zero except $\sigma_{m,c}$):

$$\sigma_\alpha = \sqrt{m^2\sigma_{r_c}^2 + r_c^2\sigma_m^2 + \sigma_c^2 + 2r_c\sigma_{m,c}} \tag{3.17}$$

This completes the discussion of how r_c and α are calculated, a summary of which can be seen in alg. 2. The results of this analysis can be seen in figure 3.9.

Algorithm 2 Calculating r_c and α

```
for b ∈ {0.0, 0.1, ..., 0.9} do
    r_a ← approximate r_c found using data from Fig. 3.3
    for r ∈ {r_a − 0.0001, r_a − 0.00009, ..., r_a + 0.0001} do
        Simulate 100 runs at this r and average the densities
        Fit the curve (after t = 1,000) using eq. 3.15
        Save fit parameters α(r) and A(r)
    r_c ← 0-crossing of A(r) using linear fit
    α ← value of linear fit of α(r) at r_c
```

3.4.2 DATA COLLAPSE FOR β AND $\nu_\parallel$

We now have a measurement for the exponent of the decay of the density, but we have set out to calculate the three exponents β, $\nu_\parallel$, and $\nu_\perp$; how is α related

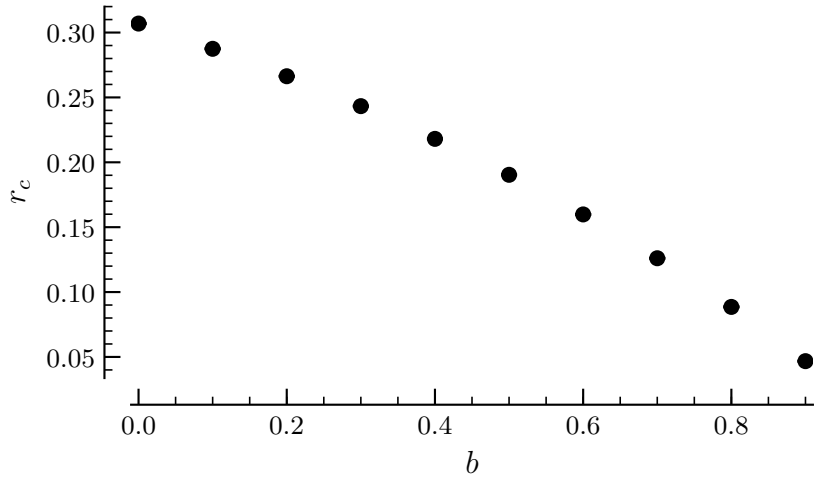

Figure 3.9: The critical infection probability as a function of the probability for a lower branch state to bounce. Errorbars are too small to be visible.

to these three exponents? To see the relationship we will now derive the scaling relationship for the density (again, we are following [137]). We will then use the scaling relationship to derive a data collapse relationship to allow us to measure the exponents β and $\nu_\parallel$.

Scaling Relation. To begin with, consider the density as a function of t and τ (in this and all other derivations we will treat b as a non-variable detail of the model). We expect that, at least asymptotically, scaling the order parameter by some λ should scale the density with exponent β and the time with exponent $-\nu_\parallel$.

$$\lambda^\beta \rho(t,\tau) \simeq \tilde{\rho}(\lambda^{-\nu_\parallel} t, \lambda\tau)\,, \tag{3.18}$$

where the symbol $\simeq$ means 'asymptotically equal'. We now set $\lambda = t^{1/\nu_\parallel}$ which causes $\lambda^{-\nu_\parallel} t = 1$. We then multiply through by $\lambda^{-\beta}$ to obtain:

$$\rho(t,\tau) \simeq t^{-\beta/\nu_\parallel} \tilde{\rho}(1, \tau t^{1/\nu_\parallel}) \tag{3.19}$$

If we measure this quantity at criticality, we have $\tau = 0$, so $\tilde{\rho}(1, \tau t^{-\nu_\parallel}) = \tilde{\rho}(1,0)$ which is a constant, therefore:

$$\rho(t) \sim t^{-\beta/\nu_\parallel}\,, \tag{3.20}$$

or in other words $\alpha = \beta/\nu_\parallel$. This means that if we can separately measure either β or $\nu_\parallel$ we will be able to use our measured value of α to get the other. To do this we will make use of the data collapse implied by eq. 3.19.

Data Collapse. We should get a collapse if we scale the density curves in the following way:

$$\rho \to \rho t^{\alpha} \tag{3.21a}$$

$$t \to t|\tau|^{\nu_{\parallel}} \tag{3.21b}$$

We can then vary the value of $\nu_{\parallel}$ until we get the best collapse. Selecting the correct value of $\nu_{\parallel}$ will cause the curves to collapse to two sets, one each for positive and negative τ. Examples of these curves showing the collapse can be seen in Fig. 3.10.

3.4.3 MEASURING THE COLLAPSE

If we are going to use this data collapse it would be useful to be able to define rigorously how well the data is collapsed. There is currently no widely used and agreed upon procedure for doing this and so I will here introduce a method which can be used to quantify the collapse. It is similar to a method proposed by Bhattacharjee & Seno [140] but differs slightly in the details. I will compare the approaches in section 3.7.2.

First we scale the density and time according to equation 3.21. For convenience we will define:

$$\rho' \equiv \rho t^{\alpha} \tag{3.22a}$$

$$t' \equiv t|\tau|^{\nu_{\parallel}} \tag{3.22b}$$

So that when we plot these we are essentially seeing some function $\rho'(t')$. We now wish to have some quantitative way to measure the degree of the collapse. A complication in this procedure is the fact that for a given time t each curve has a different scaled time t' (due to each curve corresponding to a different value of τ) so comparing the points on the curve is nontrivial. In order to circumvent this problem we can define a new scaled-time basis for all of the curves and use linear interpolation to find the value of the scaled density at each time point. The procedure is as follows:

1. Find the minimum and maximum values of t' across all curves. The minimum unscaled time here is $t = 1,000$ and the maximum is simply the end point of the runs at $t = 100,000$. Again the beginning of the curves is not used to avoid non-universal transients.

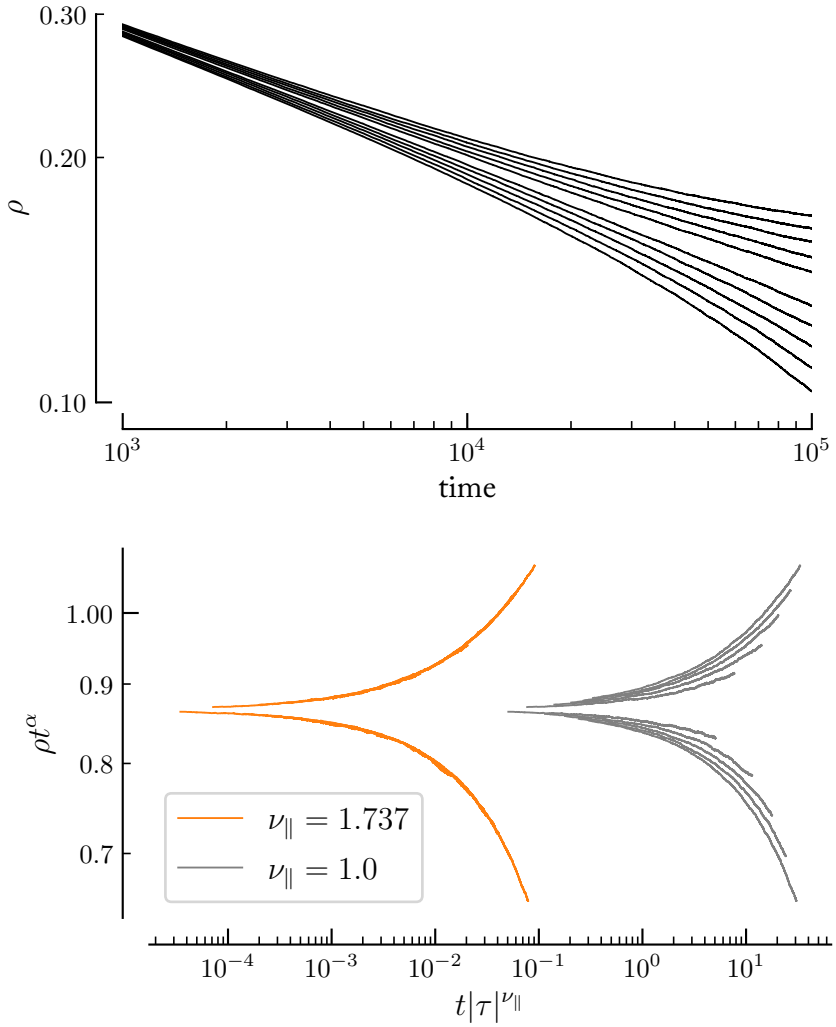

Figure 3.10: Example showing the collapse of density curves for the $\nu_{\parallel}$ calculation. Density curves calculated $\pm 1\%$ of the calculated r_c value are scaled for a range of values of $\nu_{\parallel}$ - the best collapse in this example is highlighted in orange (all curves are there but just hidden by the collapse). This example is for $b = 0.6$.

2. Generate $100,000$ points spaced evenly between these - call these new points $t'_{int.}$

3. Use linear interpolation to find the value of each ρ' at each new scaled time - call the linear interpolation function η. Note that we do not use any extrapolation beyond the end points of the curve.

Once these points are calculated then the measure used is to simply sum the squared differences of each unique pair of curves at each new t'. The following function takes as arguments the set of all density curves along with the associated values of τ which I will denote $\{\rho : \tau\}$ and a guess at $\nu_{\|}$ and return a single number which is minimised when the collapse is best.

$$\Psi(\{\rho;\tau\},\nu_{\|}) = \sum_{i}\sum_{j>i}\sum_{k=1}^{100,000} \Pi(\tau_i,\tau_j,k)\left[\eta(\rho_i,\tau_i,\nu_{\|},k) - \eta(\rho_j,\tau_j,\nu_{\|},k)\right]^2 , \tag{3.23}$$

where i and j are indices of the density curves and k is an index denoting which of the new time coordinates to use. The function $\Pi(\tau_i,\tau_j,k)$ is simply a boxcar function to ensure that only overlapping sections are compared and is zero everywhere except where τ_i, τ_j and k conspire to create an overlap of the two scaled functions in question at the scaled time t'_k. An expression for the scaled time coordinate is:

$$t'_k = t'_{min} + \frac{k(t'_{max} - t'_{min})}{100,000} , \tag{3.24}$$

where t'_{min} and t'_{max} are the minimum and maximum included values of the scaled time as discussed above. The function $\eta(\rho_x,\tau_x,\nu_{\|},k)$ returns the interpolation of the scaled density $\rho'_x = \rho_x t^{\alpha}$ at the scaled time t'_k.

By finding the value of $\nu_{\|}$ which minimises Ψ we will find the greatest degree of collapse and therefore the correct value of $\nu_{\|}$. In order to calculate the uncertainty in the exponents measured by the collapse we can use a Monte Carlo method; we already know the uncertainty in the other quantities so if we repeat the collapse many times with parameters chosen from a Gaussian distribution with the correct uncertainty we will have a distribution for the measured value of $\nu_{\|}$ from which we can extract the uncertainty. We know from equation 3.20 that $\alpha = \beta/\nu_{\|}$ and we have already found α when we found the critical point. So by combining these two procedures we can calculate two of the three independent exponents. The third exponent we need to measure is $\nu_{\perp}$, which characterises the scaling of spatial extensions in the system (unlike $\nu_{\|}$ which characterises temporal extension). The

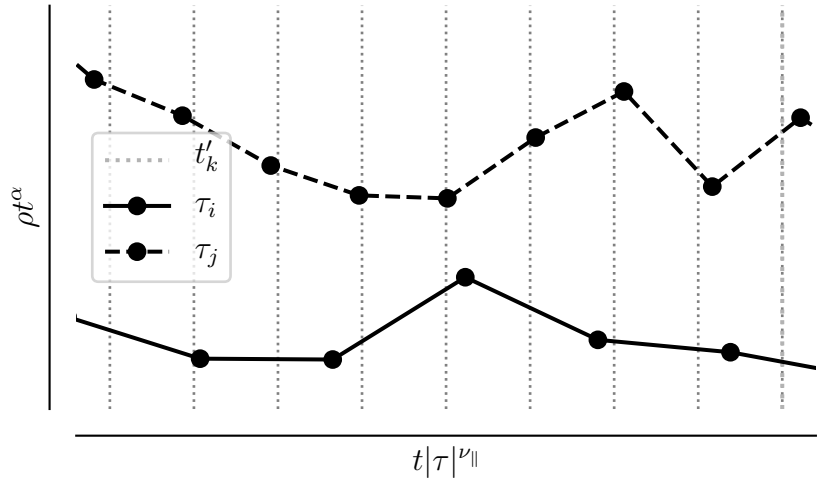

Figure 3.11: Schematic of how the resampling works in the quantification of collapse. The vertical grey lines represent the new time basis. We wish to compare how 'collapsed' the curves labelled τ_i and τ_j are, but the fact that they have different x coordinates makes the comparison difficult. The remedy is to resample both curves with a common basis t'_k represented by the grey lines. The points where the the linearly interpolated scaled density curves cross these grey lines are used to compare how close the curves are to each other. As the curves move close to each other this distance will decrease, causing Ψ to be minimised.

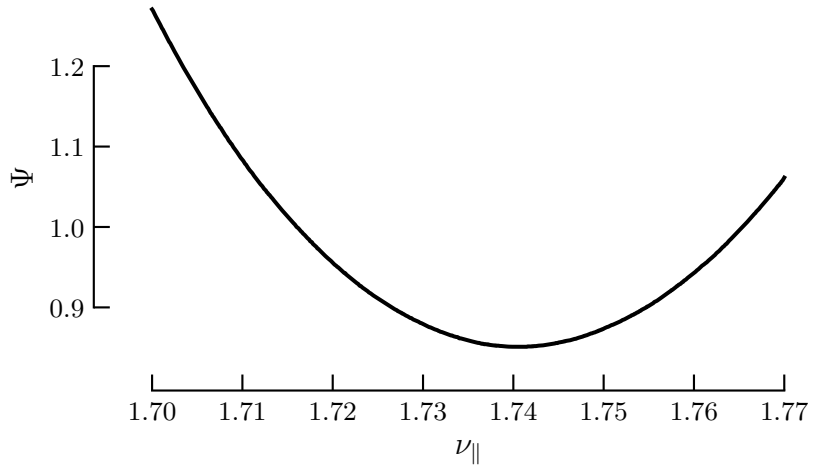

Figure 3.12: An example of Ψ as a function of $\nu_{\parallel}$ for the determination of best collapse (at $b = 0.5$). The best collapse is obtained at the minimum of Ψ.

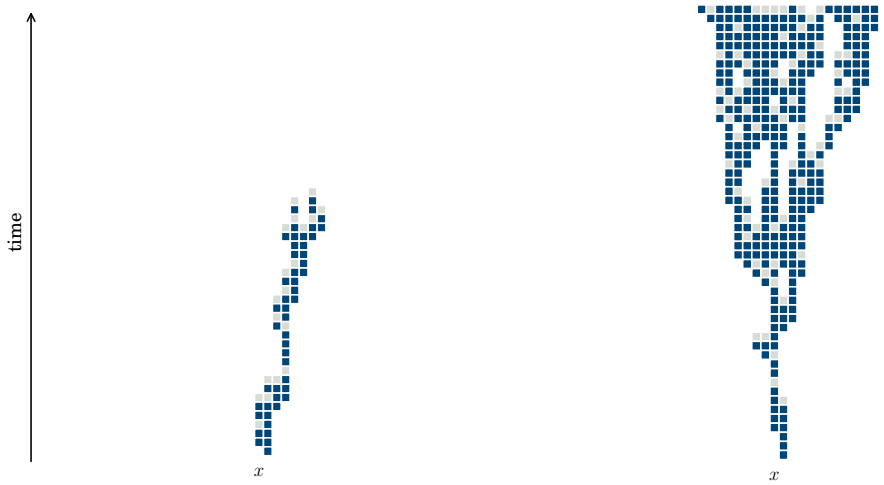

Figure 3.13: Examples of typical runs spreading from a single seed below and above the critical point. The example on the left is below the critical point, the example on the right is above the critical point.

quantities measured thus far will not allow us to do this as we do not have any which scales this way. In order to determine the third exponent I will turn my attention to calculations done with the second kind of initial condition, the spreading from a single active seed.

3.5 SINGLE SEED INITIAL CONDITIONS

As discussed in section 3.1.3 there are two different ways of thinking of the phase transition. The first way is starting with a homogeneous lattice, and is what we have discussed above. The order parameter associated with this is the density of the lattice after infinite time; after the transition we expect a non-zero steady state density. The other way of considering the transition is to observe the time evolution of a single seed; in this instance we are interested in the probability that there will still be activity on the lattice after infinite time. This encodes information about the spatial behaviour of the system in a more natural way than the homogeneous initial condition because of the spreading behaviour of the activity so we will use this configuration to calculate the associated critical exponent, $\nu_{\perp}$.

One other advantage of this initial condition is that the available system size is essentially infinite; instead of populating a lattice of a fixed size with the initial condition, we can instead use two arrays of variable size, one holding the locations of all upper branch sites and the other holding the location of all lower branch sites (there is also a computational advantage - if large parts of the lattice are going to be empty then it is computationally wasteful to iterate over them and checking their

behaviour).

There are three quantities typically measured in this type of calculation and each has an associated dynamical exponent :

- $P_{surv}(t)$ - the survival probability of the cluster. Scales as $P_{surv} \sim t^{-\delta}$
- $N_a(t)$ - the total number of active sites (in our case the upper branches). Scales as $N_a(t) \sim t^{\Theta}$
- $R^2_{surv}(t)$ - the mean square spreading from the origin (averaged only over surviving clusters). Scales as $R^2_{surv}(t) \sim t^{\tilde{z}}$

Before proceeding, it is worth checking that our system has the rapidity reversal symmetry, which is what means that Directed Percolation models have only three instead of four independent critical exponents.

3.5.1 CHECKING THE RAPIDITY REVERSAL SYMMETRY

Rapidity reversal symmetry means that the critical exponent related to the steady state density is equal to the critical exponent of the survival probability of a single seed. This is satisfied if ρ_∞ is asymptotically proportional to P_{surv}:

$$\lim_{t\to\infty} \rho(t) = \lim_{t\to\infty} \mu^2 P_{surv}(t)\,, \tag{3.25}$$

for some constant μ. The gradient of these curves are the dynamical exponents α and δ and we have seen the way that you can get from α to β via $\nu_\parallel$ and a scaling relationship - the same is true of δ and β'. So rapidity reversal symmetry is satisfied if $\alpha = \delta$. We should be able to see this relationship if we plot $\rho(t)$ and $P_{surv}(t)$ on a log-log plot and checking to see if the have the same gradient - the factor μ^2 merely shifts the curves up and down the y axis. A plot of these curves for all values of b is shown in figure 3.14 (here is only one curve of $\rho(t)$ plotted because they all were on top of each other anyway). There is an excellent agreement here and we can rest assured that our system does have the rapidity reversal symmetry, meaning that the two exponents β and β' are equal. Incidentally, these power law decay curves also verify that these processes have the same critical value of the infection probability. We could in fact calculate the critical point from these curves instead of the $\rho(t)$ to double check that that the critical points are at the same place; I will come back to this in section 3.6.1.

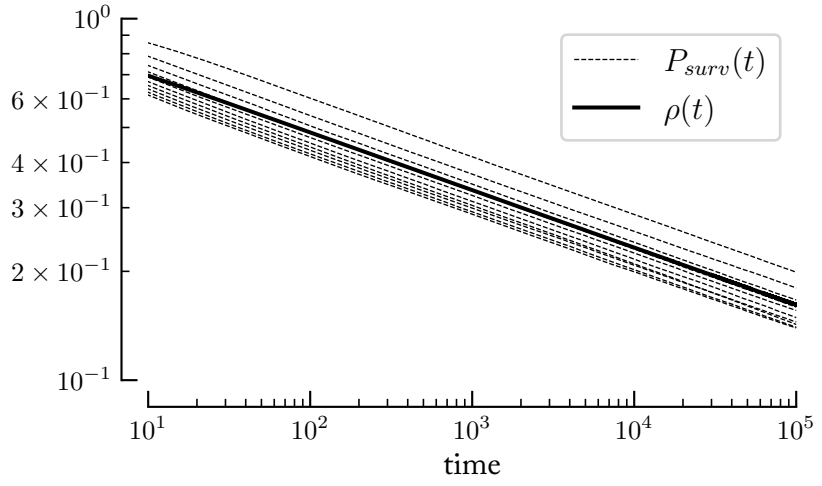

Figure 3.14: Comparison of $\rho(t)$ at $b = 0.0$ with $P_{surv}(t)$ for all values of b. All curves share the same gradient, indicating the presence of rapidity reversal symmetry.

3.5.2 MEAN SQUARE SPREADING

The Third Exponent. Of the three quantities typically measured from single seed simulations the one which most obviously captures the spatial dynamics (and therefore the exponent $\nu_\perp$) is the mean square spreading averaged over surviving runs, $R^2_{surv}(t)$, which is defined as the mean of the squared distance of active sites, averaged over surviving runs only. It has an associated dynamical exponent $\tilde{z}$ such that $R^2_{surv}(t) \sim t^{\tilde{z}}$. We will again use a scaling relationship to get an expression for $\tilde{z}$ in terms of our three independent critical exponents. We can then measure $\tilde{z}$ using the same method we used to measure α.

How should we expect this quantity to scale? The mean square spreading can be calculated by integration over the distance and averaging over the number of active sites, as follows:

$$R^2(t,\tau) = \frac{1}{N(t)} \int dr r^2 \Upsilon(t,r,\tau)\,, \tag{3.26}$$

where r is the distance, $N(t)$ is the number of active sites (note, not the same as the number of surviving clusters), and $\Upsilon(t,r,\tau)$ is the *pair-connectedness* function, i.e. the probability that a given site will be active if the origin is active. We will discuss the pair-connectedness function in greater detail in section 3.5.3. We can then utilise the fact that time scales with exponent $\nu_\parallel$ and that space (r is just a spatial coordinate) scales with exponent $\nu_\perp$ to obtain the following scaling expression:

$$R^2(t,\tau) \simeq \lambda^{2\nu_\perp} \tilde{R}^2(\lambda^{-\nu_\parallel} t, \lambda\tau)\,, \tag{3.27}$$

for some scaling function $\tilde{R}^2$. This leads to the dynamical relation:

$$R^2_{surv}(t) \sim t^{2\nu_\perp/\nu_\parallel} \tag{3.28}$$

$$= t^{2/z}. \tag{3.29}$$

For full details see [137]. So once we measure the dynamical exponent z we can use our already calculated value of $\nu_\parallel$ to get $\nu_\perp$. One slight difference in the calculation is that we do not recalculate the position of the critical point, we just use the already calculated value of r_c as the location of interest because the value found in the α calculation seems to be more accurate (see section 3.6.1 for a discussion about critical points).

Calculating the Mean Square Spreading. The calculation of $R^2_{surv}(t)$ is done in two stages. First, during the runs the following quantity is calculated:

$$R^2(t) = \frac{1}{N_{active}(t)} \sum_i x_i^2 \,, \tag{3.30}$$

where $\{x_i\}$ are the coordinates of the active, 'upper branch' sites (we define the origin as $x = 0$) and $N_{active}(t)$ is the number of active sites in the run at this time. Note that this N_{active} is not quite the same quantity as the $N_a(t)$ mentioned above, which is an averaged quantity over a number of runs whereas $N_{active}(t)$ used here is specific to each run and is for averaging the squared spreading only. The simulation is repeated a number of times and this curve is calculated each time, with all of the curves then being summed together. Secondly, the spreading is averaged over surviving runs. In order to do this we must know how many runs are alive as a function of time - this is done in a separate step once the runs have completed. The death time of each run is saved and this can be used to find the number of runs alive as a function of time. If the death times are a set D then we simply have:

$$N_{alive}(t) = n(\{d \in D : d > t\}) \,, \tag{3.31}$$

where $n(A)$ is the number of elements in some set A. We can now use this quantity to correctly average the mean square spreading:

$$R^2_{surv}(t) = \frac{1}{N_{alive}(t)} \sum R^2(t) \,, \tag{3.32}$$

where the sum is over all runs. This completes the description of how the mean square spreading was calculated. Examples of calculated $R^2_{surv}(t)$ curves (divided by a curve which allows the deviations to be more easily observed) can be seen in fig.

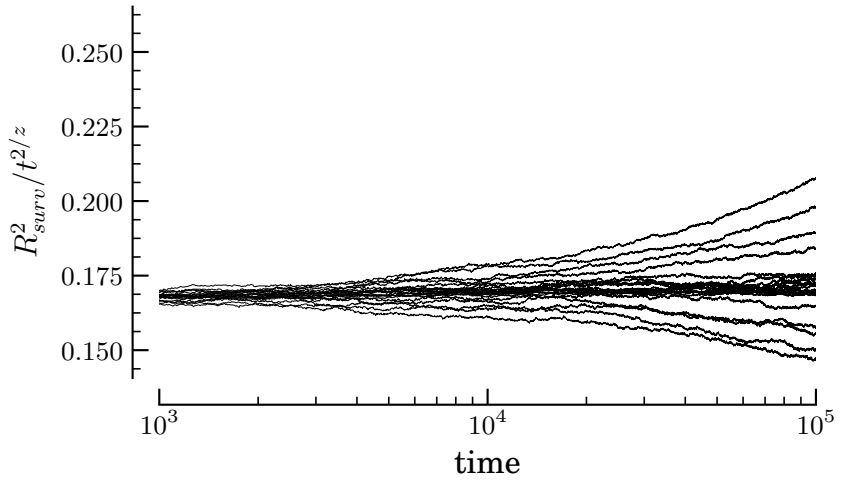

Figure 3.15: A collection of curves showing the ratio of mean square spreading averaged over surviving runs divivded by the 'expected' curve (in this case $t^{2/1.5879}$) to show the deviation.

3.15. This calculation, combined with the ones for β and $\nu_{\|}$ are enough to get all three independent critical exponents. However, there are a couple of other things it is worth looking at, including the pair connectedness function.

3.5.3 COLLAPSE OF THE PAIR CONNECTEDNESS FUNCTION

A key quantity in spreading simulations is the pair connectedness function $\Upsilon(x, t, \tau)$. This function measures the degree of causal relationship between two points and is simply the probability that site is active at a given time, given that another site (in our case the origin) was active at some other time. In this section we will verify that this quantity behaves as expected, and collapses for our measured values of the exponents - to do this we will derive the appropriate scaling form (following [137]) and check the collapse. As we have seen above, data collapses can be used to actually calculate the exponent and we can do this to check the agreement of the two methods of calculation.

To determine the scaling, note that the probability that a site is active at a given time is just the probability that the single seed generated a cluster which lasted that long ($P_{surv}(t)$), multiplied by the probability that a randomly chosen site is active ($\rho(t)$). Because of the rapidity reversal symmetry, we know that ρ and P_{surv} scale with the same exponent, β so we should expect Υ to scale as:

$$\Upsilon(x, t, \tau) \simeq \lambda^{-2\beta}\tilde{\Upsilon}(x\lambda^{\nu_\perp}, t\lambda^{\nu_\|}, \lambda\tau) \tag{3.33}$$

b	$r_c(\alpha)$	$r_c(\delta)$	$r_c(z)$	$r_c(\Theta)$
0.0	0.3069120(47)	0.3069111(21)	0.306919(26)	0.3069126(39)
0.1	0.2874636(42)	0.2874690(30)	0.28751(35)	0.2874664(36)
0.2	0.2663241(33)	0.2663301(18)	0.266339(26)	0.2663328(37)
0.3	0.2432822(33)	0.2432779(30)	0.243294(33)	0.2432866(51)
0.4	0.2180595(17)	0.2180651(51)	0.2180245(91)	0.2180581(42)
0.5	0.1903620(24)	0.1903632(47)	0.190438(66)	0.1903601(46)
0.6	0.1598276(45)	0.1598350(31)	0.15986(34)	0.1598384(44)
0.7	0.1260581(23)	0.1260591(19)	0.12615(13)	0.1260606(86)
0.8	0.0885545(22)	0.0885493(85)	0.088557(14)	0.0885537(81)
0.9	0.0467526(14)	0.0467515(16)	0.0467508(50)	0.046758(17)

Table 3.3: Measurements of the critical point by the methods described for the four dynamical exponents.

This scaling form implies a data collapse at criticality which can be used to remove the time dependence of the curves:

$$\Upsilon(x,t,\tau) \simeq t^{-2\beta/\nu_\parallel}\tilde{\Upsilon}(1, x^{-\nu_\parallel/\nu_\perp}, 0) \tag{3.34}$$

So if we plot $\Upsilon(x,t)t^{2\beta/\nu_\parallel}$ (remembering that we have already calculated β and $\nu_\parallel$ in the previous section) against $x/t^{\frac{\nu_\perp}{\nu_\parallel}}$ for a range of values of $\nu_\perp$ we should see the best data collapse for the best value of $\nu_\perp$. I did this using the same method for measuring the degree of collapse that I used in the previous calculation (although this time the resampling is done in the x coordinate, rather than the t coordinate). An example of the curves generated in this procedure can be seen in figure 3.16.

3.6 RESULTS

3.6.1 CRITICAL INFECTION PROBABILITY

The system undergoes a phase transition at a critical value of infection in probability which we call r_c; there would be a different value of r_c for different values of survival probability p, but in this analysis we held p constant at a value of 0.7. The critical point was determined using the method outline in section 3.4.1. The analysis presented there was specifically using the expected power-law behaviour of the density curves when starting with a fully active lattice - these curves were used in measuring the dynamical exponent α. The result of this specific analysis can be seen in the first column of table 3.3 along with the uncertainty as calculated as explained in the text. It is also possible to measure the critical point using the same method with the variables measured during the single-seed runs. These quantities were $P_{surv}(t)$,

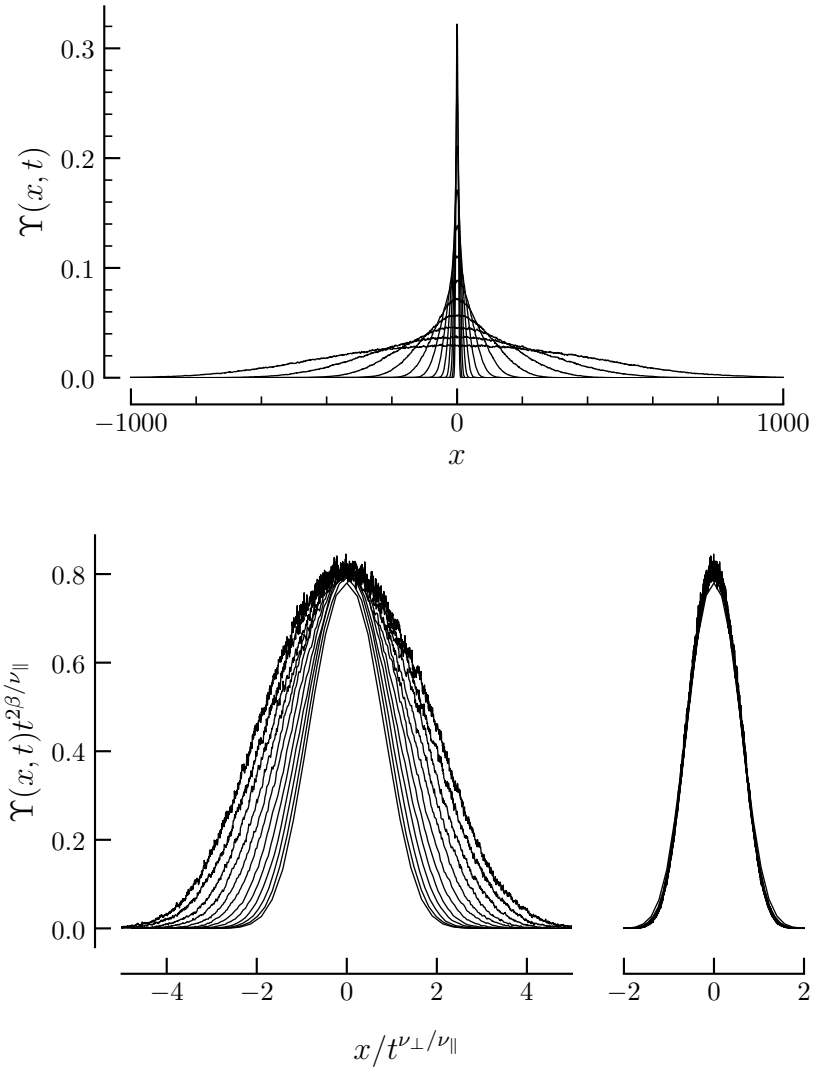

Figure 3.16: Above: Example of scaled density profiles made during $\nu_\perp$ calculation. The snapshots are taken at times $t \in \{16, 32, 64, ..., 32768\}$ and these curves are for $b = 0.2$. The value of $\nu_\perp$ which gives the best collapse is the critical value.

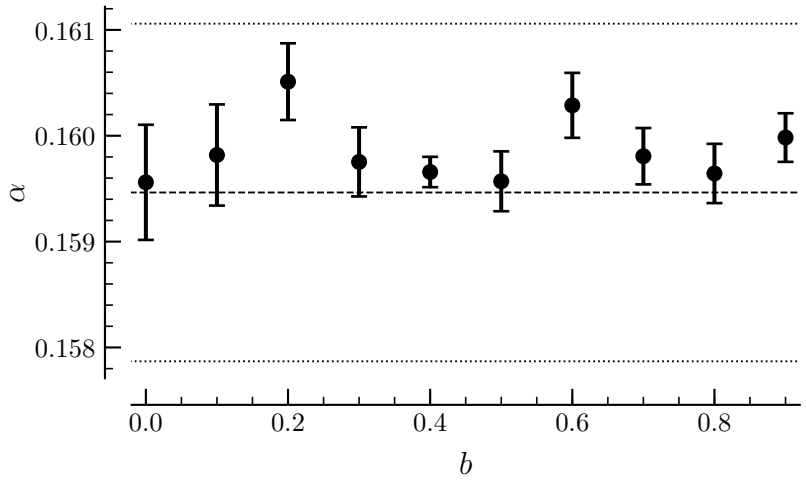

Figure 3.17: Plot of the dynamical exponent α as a function of the bounce probability b. The error bars denote one standard deviation either side, worked out as described in the text. The true value is plotted as a dashed line, for comparison. The dotted line is a guide to the eye and shows plus or minus one percent of the reference value. The measured value of $alpha$ is in good agreement for all values of b, suggesting that adding the lower branch states does not alter the universality class. Throughout this chapter graphs of critical exponents will use this same style.

$R^2_{surv}(t)$, and $N(t)$ with associated exponents δ, z, and Θ respectively. The critical point was also measured for each of these variables and these measurements are included in the table in the remaining columns. The critical points as measured by each variable are in excellent agreement with each other.

Choice of Critical Point. The fact that we have a selection of critical points leaves us with the question of which one to use. By looking at the table we can see that the uncertainties in $r_c(z)$ and $r_c(\Theta)$ are sometimes an order of magnitude larger than the uncertainties for $r_c(\alpha)$ and $r_c(\delta)$ so these critical points were not used. On balance the uncertainties in $r_c(\alpha)$ are more consistently smaller, so we choose to use $r_c = r_c(\alpha)$ from now on. It is worth noting that we should expect that with $b = 0$ we should recover the critical point from the Allhoff & Eckhardt[96] paper, which was reported as being near 0.3069 and our measurement agrees, being $0.3069120(47)$.

3.6.2 DENSITY DYNAMICAL EXPONENT

As part of the calculation to find the critical point we also calculate the dynamical exponent α which describes how the density decays at the critical point. The result of this calculation can be seen in figure 3.17. Also plotted as a dashed line is the true

value of the exponent as reported in [141][2] As a guide to the eye I have included dotted lines showing a one percent margin either side of the true value. The measured value of α is consistent with the 1D DP case to within this one percent margin, and importantly shows no appreciable trend with increasing b. This is a good indication that the addition of the bouncing behaviour does not change the universality class of the transition, as expected.

There is a noticeable bias in the results calculated here, as all of the measured values of α are above the true value, and none are below. This could be an indication of some systematic issue with the analysis thus far. A higher measured value of α would mean that my analysis predicts that at the critical point the density decays more quickly than it truly does. This could be the result of a number of systematic issues. Perhaps the measured location of the critical point is wrong, and the measurement of the exponent at this incorrect critical point is correct; if this is the case then a high value of α would suggest that the measured critical point is lower than the true value, as the density decays more quickly at lower values of r. Alternatively, the measurement of the critical point could be correct but with an incorrect measurement of α; this could perhaps be due to some systematic bias in the curves used to fit the data but it is not clear how.

Alternatively, this could be a manifestation of finite-size effects in the simulation. In this study we have selected a large lattice so that finite-size effects could be ignored, but this is still an approximation. The finite lattice size means that there is always the chance that the system could completely die, which could show up in the data has an overestimate of the decay rate. Given that the measured values are accurate to one percent it's possible that the approximation is showing its head here. If this is the case we should expect the bias to disappear for the measurements from a single seed, as the computational method for simulating these has an essentially infinite lattice size.

3.6.3 DENSITY COLLAPSE FOR β AND $\nu_{\parallel}$

In order to get $\nu_{\parallel}$ from the density curves we utilise the data collapse method as explained in section 3.4.2. The value of $\nu_{\parallel}$ found this way is shown in figure 3.19. The values of $\nu_{\parallel}$ are consistent with the expected value, and do not exhibit a noticeable trend or bias. There is a noticeably large uncertainty in the measured value at $b = 0.1$; it is unclear where this comes from as the uncertainty in α and r_c at this value of b are not noticeably larger than at other values of b.

[2] All of the reference values for one-dimensional DP are taken from this paper and I will be using them throughout the results section as a check to my results.

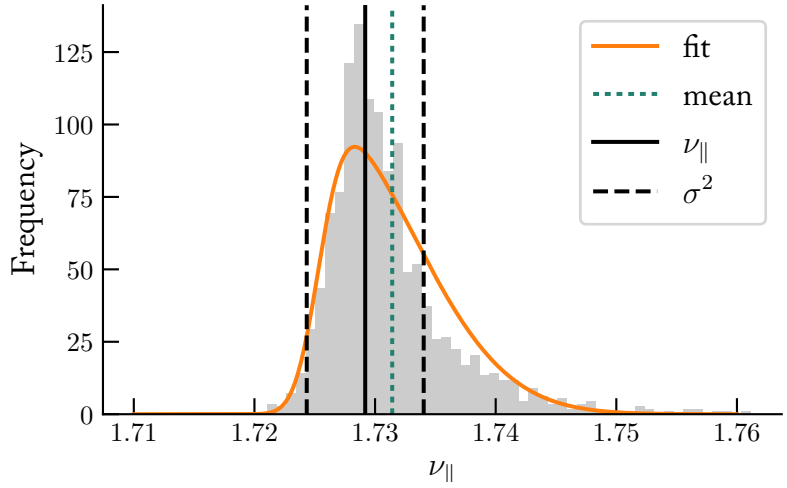

Figure 3.18: An example histogram used in the calculation of the uncertainty in the measure of $\nu_{\parallel}$, this example is for $b = 0.8$. 1,500 samples were taken of both r_c and α with standard deviations corresponding to the uncertainties calculated for those quantities. When the collapsing procedure is repeated for each combination of these values, we get the distribution shown above. As can be seen in the figure, distribution is skewed to the right which makes the mean of the distribution a questionable candidate for a measured value. Therefore, this distribution is not used to calculate the value of $\nu_{\parallel}$, only its standard deviation. The value of $\nu_{\parallel}$ used is the value of $\nu_{\parallel}$ calculated from the collapse procedure, and appears to be more like the mode of the distribution than the mean.

In order to calculate the uncertainty in $\nu_{\parallel}$ a Monte Carlo method was used. The collapsing algorithm was repeated using a range of value of r_c and α which yields a distribution of values of $\nu_{\parallel}$, the variance of which was then measured. It would be possible to use this distribution to extract the actual value of $\nu_{\parallel}$, being hopefully the centre of the distribution - however the distributions obtained this way were not symmetric normal distributions as can be seen in the case of $b = 0.8$ in figure 3.18. This means that there are multiple different ways that one could decide for what to use as the centre of the distribution, e.g. the mean, or the median, or the mode. For this reason these distributions were only used to get an estimate of the standard deviation of the actual value of $\nu_{\parallel}$, which was obtained by using Scientific Python's `skewnorm.fit` function to first fit a skew normal distribution, then finding the standard deviation of this distribution. For the absolute value of $\nu_{\parallel}$ we can use the value calculated using the collapse method at the calculated values of α and r_c.

Now that we have a value for $\nu_{\parallel}$ and α we can obtain the value of the critical exponent β via the relationship $\alpha = \beta/\nu_{\parallel}$; the values of β can be seen in table 3.4.

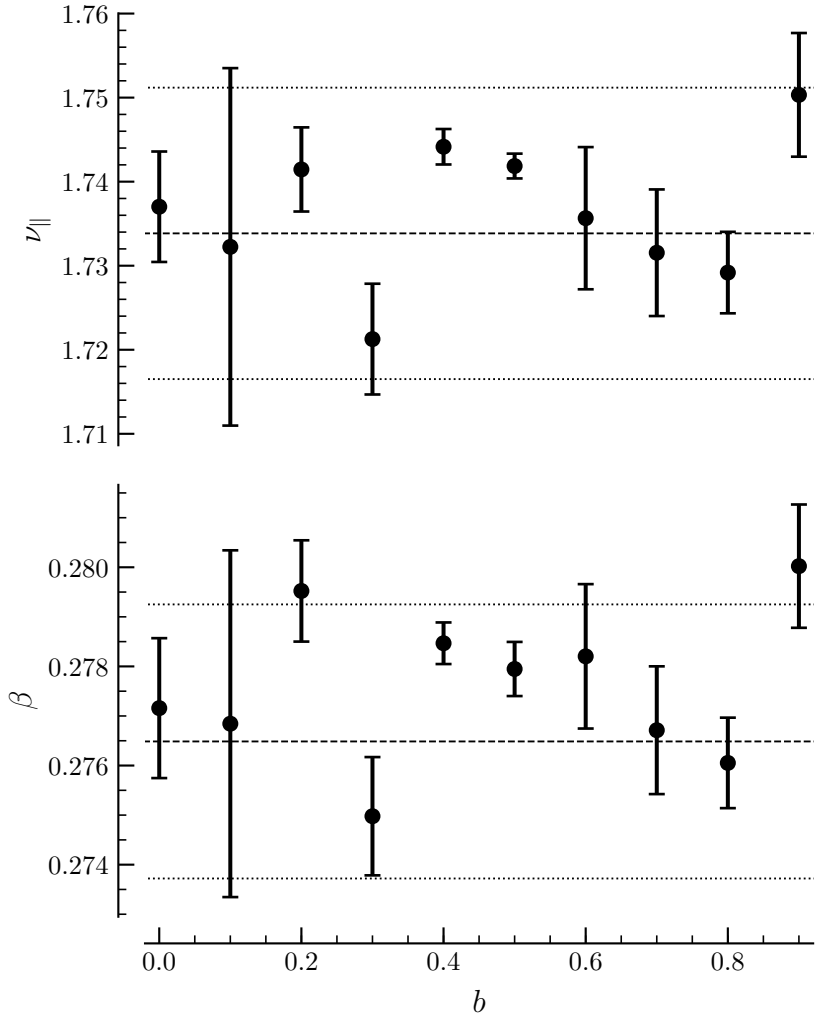

Figure 3.19: Plot of the critical exponents $\nu_\parallel$ and β as a function of b, obtained through a data collapse measure of the density curves; uncertainties are obtained using a Monte Carlo method. Values are consistent with expected value of the exponent and show not noticeable trend or bias.

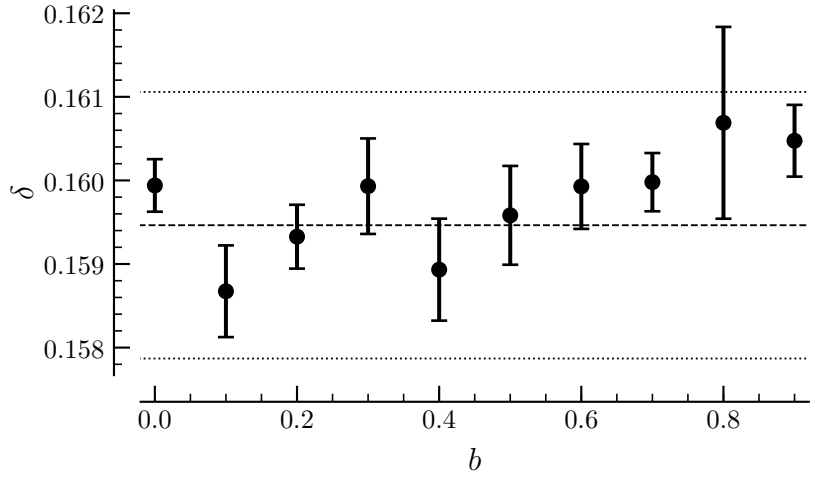

Figure 3.20: Plot of the measured value of the dynamical exponent related to the survival probability of a single seed initial condition as a function of b with reference value and plus or minus one percent indicated with dotted lines. There is a good agreement with the DP value for all values of b, which indicates that the rapidity reversal symmetry is not broken by the addition of the lower branches.

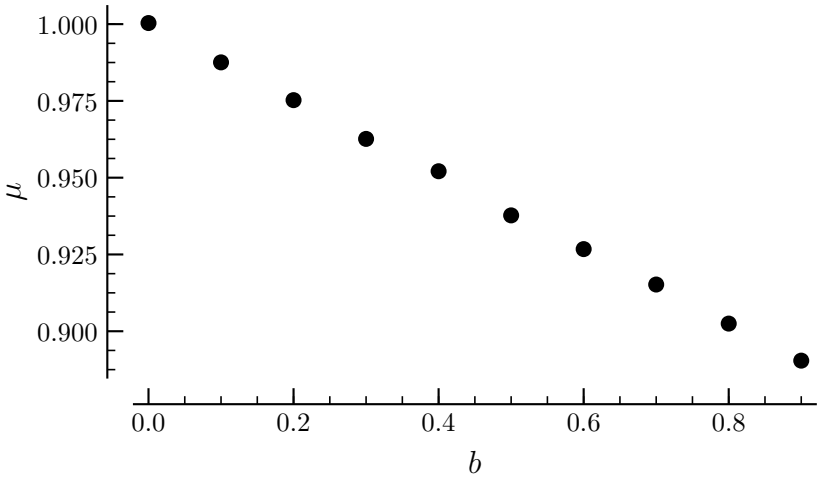

Figure 3.21: The scaling factor μ as a function of b. The scaling factor measures the relationship between the density curves and survival probability curves when discussing rapidity reversal symmetry and is the only quantity found to show a clear trend with respect to increasing bounce probability. As such it is a candidate measure for looking for bouncing in real flows.

3.6.4 RAPIDITY REVERSAL SYMMETRY

Checking the Dynamical Exponent. Rapidity reversal symmetry allows DP to be characterised by three independent critical exponents rather than the four you might expect from a naive approach to understanding the scaling. One way to check that it holds is to check if the dynamical exponent for the density, α, is the same as the dynamical exponent for the survival probability, δ. To this end δ has been calculated using the same method used to calculate α, with one change being to use the value of r_c found from the α calculations, rather than using the value we could calculate from the survival probability curves; this was done to ensure all of the measurements occur at the same value of r. The results of this measurement can be seen in figure 3.20, again with included reference value. The measured values again show a good agreement with the expected values, to within one percent for all values of b. There does not appear to be a clear trend with increasing b, which is another indication that included bouncing behaviour does not change the critical exponents. The possibility of finite-size effects in measuring α is absent from these calculations and the reduction of bias in the δ measurement compared to the α measurement is apparent in the figure: there is now a few values of b at which the measured value of δ is lower than the true value, unlike in the α. This is suggestive that the bias seen in calculating α could be due to finite-size effects.

Scaling Factor Changes with Bounce Probability. Rapidity reversal holds for our system, which means that $\lim_{t\to\infty} \rho(t) = \lim_{t\to\infty} \mu^2 P_{surv}(t)$. We know that this holds for our system because the dynamical exponents match, but what about the value of μ^2? In order to measure this a minimisation procedure was used - we want to find μ^2 which minimises the difference between the survival probability and density curves. The simplest way to measure this is to find μ which minimises the norm of $\rho(t) - \mu^2 P_{surv}(t)$ at the critical point. A slight trickiness with solving this minimisation problem is that we do not actually have curves at the critical point, we have curves near to the critical point on either side. We can construct an approximation to the critical point and use this to do the minimization by interpolating between the nearby curves. At each point in time we fit a straight line to values of the density and survival probability as a function of r, and then we can find that our estimate for the curve at r_c can be found by plugging r_c into this straight line fit. This gives us estimates of the curves actually at r_c to use to find μ, which is done using Scientific Python's `minimize_scalar` method. The results can be seen in figure 3.21 and shows a clearly decreasing trend with b; this is the first indication we have found of any difference with b. What could this trend indicate? The density curves at the critical point all lie on top of each other, which means that

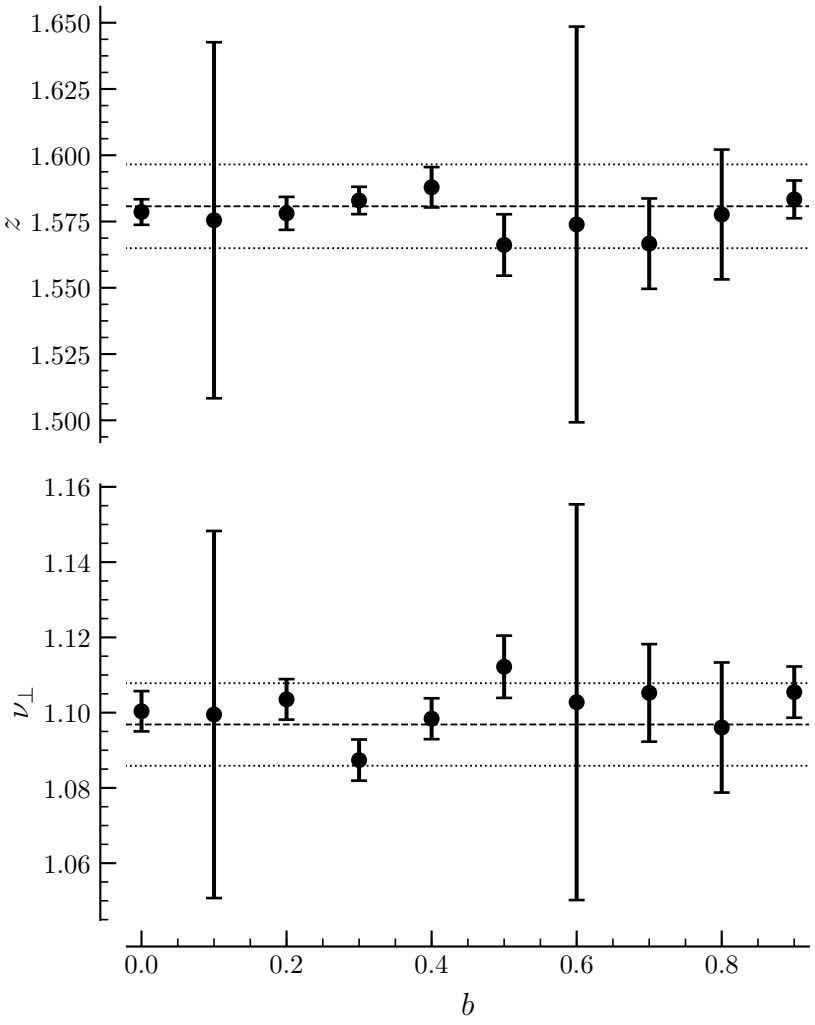

Figure 3.22: The dynamical exponent z and the critical exponent $\nu_\perp$ as a function of b. Again, there is good agreement to the reference values (plotted as dashed lines). Although there are very large uncertainties at $b = 0.1$ and $b = 0.6$ the calculated values still fall within one percent deviation for these values of b - the cause of the large uncertainty is unclear.

increasing the bounce probability does very little to the homogeneous system except move the critical point closer to zero. However, in the single seed calculations it increases the amount of time required for system to act in a truly asymptotic manner - the fact that one system is affected and the other isn't means that it might be possible to see this effect in data from a real system.

3.6.5 MEAN SQUARE SPREADING EXPONENT

In order to get the third independent critical exponent $\nu_\perp$, I first calculated the dynamical exponent related to the mean square spreading averaged over surviving runs. This used the same method as the α calculation (and used the $r_c(\alpha)$ critical

b	β	$\nu_{\parallel}$	$\nu_{\perp}$
0.0	0.2772(14)	1.7370(66)	1.1004(54)
0.1	0.2768(35)	1.732(21)	1.100(49)
0.2	0.2795(10)	1.7415(50)	1.1035(54)
0.3	0.2750(12)	1.7213(66)	1.0874(55)
0.4	0.27847(42)	1.7442(21)	1.0984(54)
0.5	0.27795(55)	1.7419(15)	1.1122(83)
0.6	0.2782(15)	1.7357(85)	1.103(53)
0.7	0.2767(13)	1.7315(75)	1.105(13)
0.8	0.27605(91)	1.7292(48)	1.096(17)
0.9	0.2800(12)	1.7503(74)	1.1055(68)

Table 3.4: Summary of the results for the three independent critical exponents. All measurements are in fairly good agreement with the expected value of 1D Directed Percolation, namely $\beta = 0.276486(8)$, $\nu_{\parallel} = 1.733847(6)$, $\nu_{\perp} = 1.096854(4)$. There is no obvious trend or bias so we can be quite confident that the model belongs to the DP universality class.

point) to find the exponent and uncertainty, and the result can be seen in figure 3.22. These data points are again in good agreement with the expected value, and unlike the α measurement seem to show no bias either above or below the critical point - again an indication that perhaps that bias was due to finite-size effects. Interesting, two of the measurements of z (at $b = 0.1$ and $b = 0.6$) have very large uncertainties, much larger than anything found so far, and much larger than any of the other z measurements. It is unclear why this should be the case, but one possibility is that the algorithm had trouble distinguishing the curves near criticality as the mean square spreading seems to be less sensitive to deviations from the critical point than the density decay. The calculation of $\nu_{\perp}$ follows from the relationship $z = \nu_{\parallel}/\nu_{\perp}$ and our already calculated value of $\nu_{\parallel}$. We therefore now have measured all three independent critical exponents, the results of which can be seen in table 3.4.

3.6.6 SUMMARY

Table 3.4 shows a summary of the results - we set out to find the three independent critical exponents β, $\nu_{\parallel}$ and $\nu_{\perp}$ and they show a fairly good agreement with the the expected value, but not to a particularly high degree of accuracy, roughly on the order of three significant figure. Importantly there is no consistent trend as the probability to bounce increases, meaning that the addition of the third parameter does not appear to change the universality class of the model.

3.7 DISCUSSION

3.7.1 FITTING METHOD

The method used in this chapter to extract the critical point and the exponent is seemingly novel, and I will now discuss some of the details of the method.

Power Law with Exponential Cutoff. In our method for extracting the exponent from a suspected power law we fit the curves with an equation of the form:

$$\rho(r,t) \approx Kt^{-\alpha(r)}e^{A(r)t} \tag{3.35}$$

an equation commonly referred to as a power-law with an exponential cutoff. This equation seems to do a fairly good job at fitting the curves but it is unclear if there is anything to be learned from this. It's possible that there is nothing particular about this form, so long as we have a parameter which somehow measures the degree of deflection from a power law, an exponential is convenient in that it has zero deflection from the power-law at the point that the exponent is zero. In fact, we know that this type of fit can not be a good for all values of t above the transition; as time tends to infinity the system will asymptotically approach a constant value, which is not possible to fit with an equation of this form. Therefore we should take with the approximation with a fairly large dose of salt, and understand that it is nothing more than an aid to calculation. It is an interesting question if there is some more robust and generally applicable form for such an approximation.

Order of Polynomial Fit. Once we have fitted our curves with equation 3.35 we then have a second fit to do, we have the parameter A as a function of r and want to extract the zero-crossing point of this parameter to determine the critical point, as well as fitting the parameter α with a polynomial so that we can use the critical point to get our critical value of α. An example of the curve shown in figure 3.7 but zoomed further out can be seen in figure A.3 and exhibits a marked curve, suggesting that a linear fit like the one used is perhaps not the best thing to do. As well as a linear fit I tried using all of the points on the curve and fitting with a quadratic function and then calculating r_c and α the same way - the result for α can be seen in figure 3.23. The quadratic fit seems to fair worse than the linear fit in two ways. Firstly, there seems to be a systematic error in the exponent, starting lower and getting higher - we might consider that this is a reflection of a true trend but notice that the worst value is obatined at $b = 0$, where we know that the model belongs to the DP class. Secondly, value of α from the quadratic case is further from the true value for most values of b (seven out of ten). For these reasons this method of fitting was rejected in

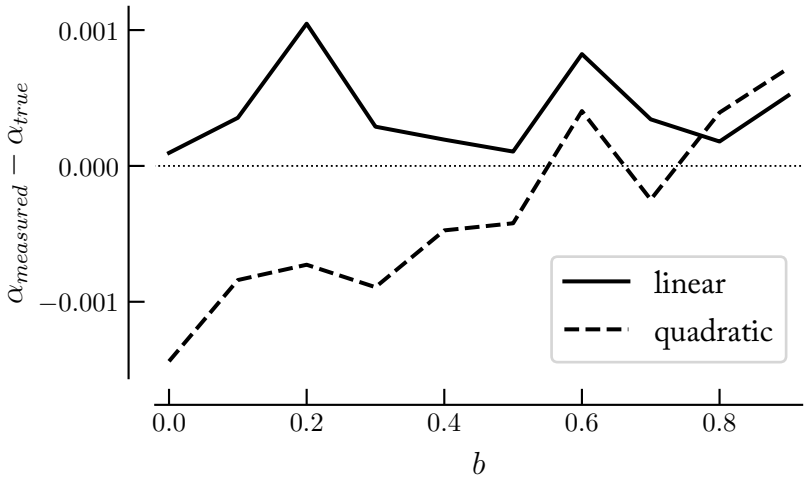

Figure 3.23: Residuals of α using either the linear fit method or a quadratic fit. The use of a quadratic fit seems to cause some systematic error and is considered less robust than the linear fit. It is unclear why this might be.

favour of the linear fit, although it is interesting to note that the quadratic fit seems to remove the bias for measuring α above its true value, this could be evidence that the finite-size effect cause of this bias is incorrect, although I am reluctant to suggest this given the fact that I do not trust these quadratic fits to be reflective of a true measurement.

3.7.2 COMPARING COLLAPSE MEASURE WITH BHATTACHARJEE & SENO

The method I used for quantifying the degree of data collapse is relatively novel, although it is similar in approach to one proposed by Bhattacharjee & Seno [140]. In their paper they also propose interpolating the curves so that they have a common basis, but they choose to do this interpolation using the coordinates of the curves themselves, rather than constructing an entirely new set of coordinates as I have done. The repeat this interpolation for each curve and then combine the distances obtained from each interpolation to get a total value for the measure. This has the advantage that it means that the distances are measured between interpolated curves and true values, where with my method there is only comparison between interpolations and interpolations (unless a scaled time coordinate happened to fall exactly on an interpolation point). I have repeated the collapse calculation outlined above but using their measure of collapse instead of mine and the results of this can be seen in figure 3.24. The figure shows the residuals of the true value from the one measured the collapse at the critical point, and there seems to be no clear winner

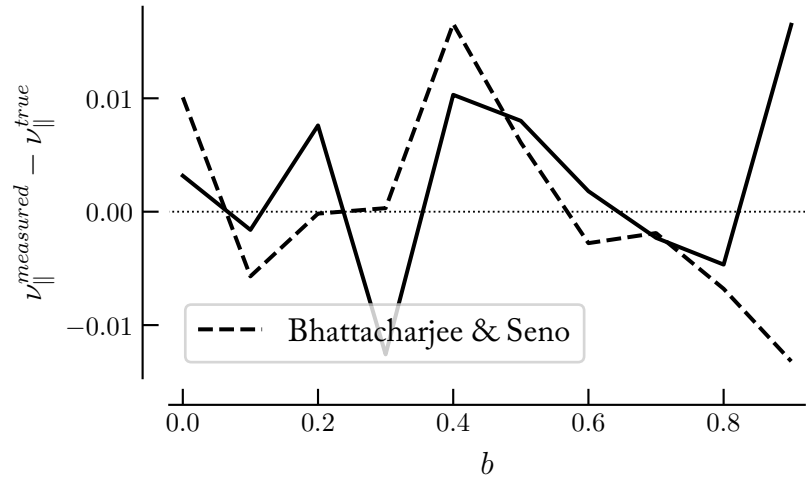

Figure 3.24: Comparison of the results of collapse quantification introduced in this chapter with the one proposed by Bhattacharjee & Seno. The methods share the idea of interpolating to find a common coordinate system for comparison but differ in the number of times this is done. There is no clear difference between the results obtained by one method over the other.

between the methods which is perhaps unsurprising given the similarity between them. Given the lower number of total interpolations in the model introduced in this chapter it may be computationally more manageable if speed is a concern.

3.7.3 LOOKING FOR THE BOUNCE IN SHEAR FLOWS

If the bouncing behaviour does not change the universality class, do we have any hope of constructing an experiment to observe it? The only measure we have calculated which has any coherent relationship to the bounce probability is μ, the parameter which measures the scaling required in the rapidity reversal symmetry. In order to measure this in an experimental setup one would need the ability to have two different kinds of initial conditions: homogeneously active turbulence and spreading from a seed of turbulence. For experiments of the first kind the 'density of active states' of DP corresponds to the turbulent fraction of a shear flow and should be measured as a function of time at the critical point. This experiment has already been conducted for Couette flow by Lemoult *et al.* in 2016 [97]. In that experiment a homogeneously active initial state was created by quenching from a higher value of Re to the critical point and the turbulent fraction (what I am calling $\rho(t)$ is called in that paper TF(t)) was measured as a function of time. If it was possible to use a similar setup but start each run with a nucleating seed of turbulence the survival probability could be calculated as a function of time and compared to the

density. To be clear here, the measured survival probability measured here is *not* the survival probability of a single puff/patch of turbulent fluid (which is known to be exponential rather than obeying a power law) but instead is the survival probability of all turbulence spawned from the initial perturbation. This would allow the rapidity reversal symmetry to be checked (as far as I am aware this has not yet been done in an experiment with shear flows, although it has been checked in a 2+1 dimensional experimental setup using liquid crystals [142]). The proportionality factor μ^2 could then be calculated by finding the asymptotic ratio of the two different measures, and my analysis in this chapter suggests that a factor of μ less than 1 could indicate the presence of this bouncing type behaviour, although of course there could be other reasons for this.

3.8 CONCLUSION

A three-state directed percolation model has been studied numerically. The third state has a 'bouncing' type dynamics motivated by the role the lower branch states play as a barrier to relaminarisation in the subcritical fluid flows. Increasing the probability for the state to exhibit the bouncing dynamics does not meaningfully change the value of the critical exponents β, $\nu_{\parallel}$ or $\nu_{\perp}$ and the system can therefore be assumed to be a member of the DP universality class. A novel method of determining the location of the critical point, as well as of quantifying the degree of data collapse have been introduced. The rapidity reversal symmetry scale factor μ has been proposed as a method of looking for the existence of the bouncing behaviour in real flows.

4 THE EXTENDED KS EQUATION IN A LARGE DOMAIN

4.1 INTRODUCTION

In the first chapter of this thesis we explored the behaviour of an extension to the damped Kuramoto-Sivashinsky equation which exhibits a subcritical transition to spatiotemporal chaos and proposed that the upper and lower branches of coherent structures play a different dynamical role in the transition. Given that for shear flows the transition belongs to the DP universality class I then investigated the possible effect that the addition of lower branch states would have on the universality class.

In the previous chapter I showed that the addition of lower branches does not change the universality class but does influence the behaviour of a non-universal feature of the transition, the proportionality factor μ which is the asymptotic ratio of the density of active states and the survival probability of the system when started with a single seed. Without any bouncing behaviour this ratio was found to be ≈ 1; as the probability to bounce was increased the ratio was found to get smaller. Therefore I proposed that this quantity could be used to probe for the existence of bouncing behaviour in shear flows. In this chapter I will show that the system of PDEs studied in chapter 2 belongs to the DP universality class and measure μ for that system.

The Need for Large Domains. The observed exponential distribution of lifetimes for the extended Kuramoto-Sivashinsky equation raises the question of why we might even consider it to be in the DP class at all, where the survival probability is known to be a power-law. This seeming discrepancy is due to the fact that in DP the survival probability decay is caused by a competition between spreading and decaying, but the system studied in chapter 2 can not display any of these dynamics. There is nowhere for the chaos to spread *to* and it does not seem to ever relaminarise locally, in essence we have studied some kind of minimal flow unit for the system. It's as if we have a DP lattice of size $N = 1$ which is not a DP system at all. Therefore, to observe any DP behaviour we need to go to larger domain sizes than the one already

studied, which was 24π. As we will see, increasing the domain size does allow for local relaminarisation and infection. In this chapter of the Thesis I will study the extended KS equation in an extended domain, and see to what extent it behaves as a directed percolation system.

4.2 FULLY ACTIVE INITIAL CONDITIONS

The first type of behaviour we will look at is that of having a fully turbulent system. This is the same kind of behaviour as that studied in Couette flow by Lemoult *et al.* [35]. We wish to ensure that the system is in a full-fledged turbulent state at the beginning of the simulation, therefore we use a similar idea to the one used by them to create an initial condition, which is to evolve the system for a time at a value of Re above the critical point to let a full turbulent flow develop, then quench the system to a value of Re near the critical point. In our model we are using the parameter R in a similar way to the way Re is used in Couette flow, so it is with this parameter we will do the quenching. The procedure is as follows:

1. Perturb the field u with a random perturbation defined by equation 2.8.
2. Evolve the system with $R = 2$ for total time $t = 10$.
3. Reduce R to desired value, this is considered the "start" of the run.

Additionally, we will only start the run if at the end of this procedure the measured turbulent fraction (as defined later) is found to be above 99 percent.

Space Discretisation. As we move to a larger domain we need to think about how we will discretise space in the numerical method. A domain size of 100 times larger than the domain previously studied was chosen, i.e. the domain size is now set at 2400π. The number of real space points and Fourier modes are both correspondingly increased by a factor of 100 from the ones used in chapter 2.

4.2.1 TURBULENT FRACTION

An example of a typical run showing both u and v (at $R = 1$) can be seen in figure 4.1. The construction of the equations means that $u(x)$ tends to have roughly equal number of positive and negative points in the turbulent parts of the flow, and many crossings of zero. This makes it slightly confusing to use u to get a measure of the turbulent fraction for the system and it is in fact easier to understand what this means with reference to the field v. As can be seen in the figure, v never takes a negative value, and there is therefore an obvious way of defining the turbulent fraction by

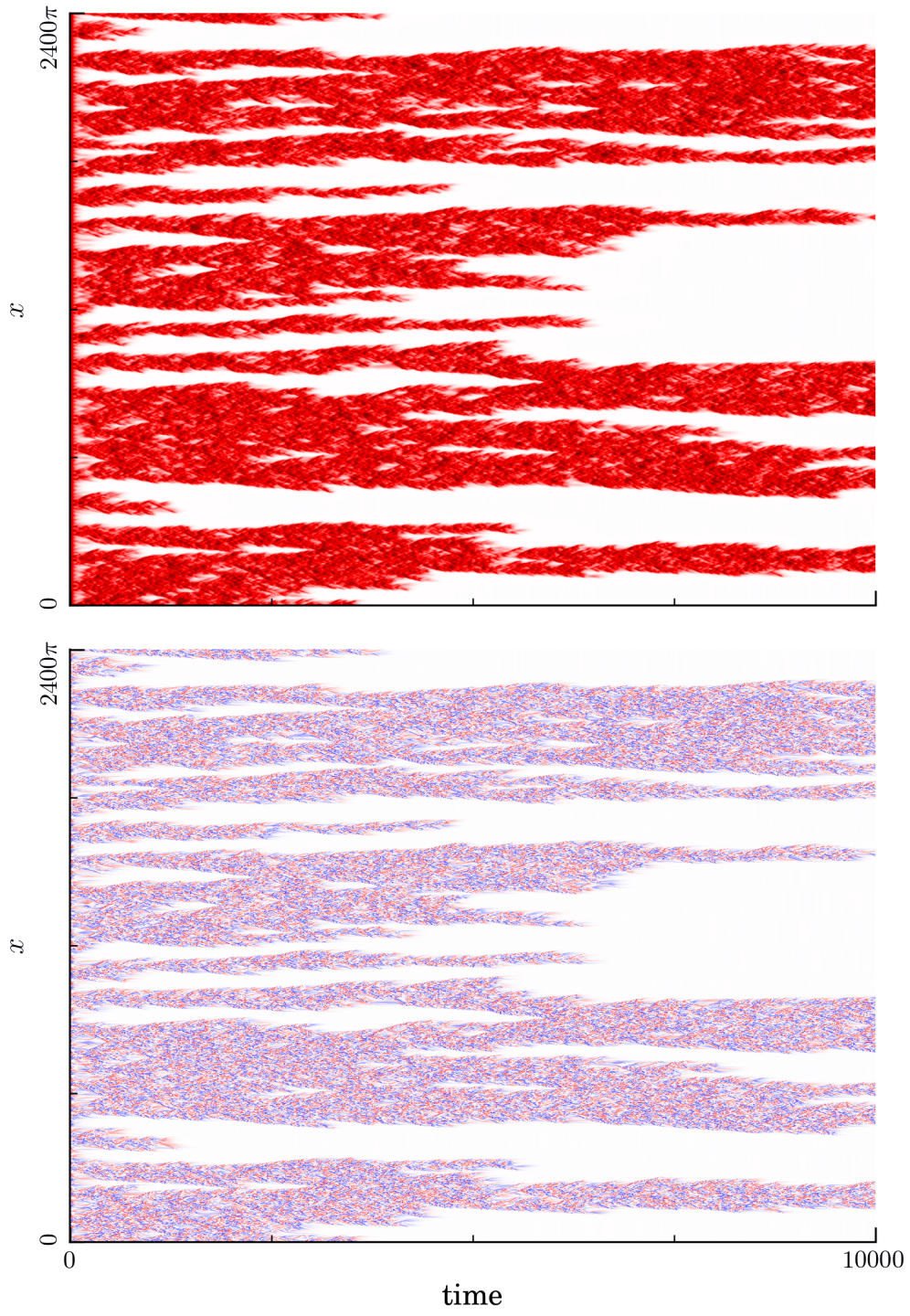

Figure 4.1: Example of the evolution of the eKSE in a large domain. The top graph is of $v(x)$ and the bottom is $u(x)$. Positive values are plotted in red and negative values are plotted in blue. The graph of u shows that positive and negative values are equally present (graph appears nearly purple) whereas we only see positive values for v which makes it a better candidate as a measure of turbulent activity due to it being easier to define what counts as turbulent. There is a strong qualitative similarity between the behaviour observed here and that of directed percolation.

looking at this field; if $v(x,t)$ is greater than some threshold value we will say that the system is turbulent at time t and position x. By checking each value of x which is present in the discretisation we can get the proportion of sites which are active as a function of time.

Choice of Threshold. How should we choose the value for this threshold? One factor of DP which might help us to decide is the existence of an absorbing state; activity should not be able to spontaneously appear from an inactive site. In chapter 2 we found that there is such a threshold for the eKSE and that it is defined by the threshold of the lower branches - therefore perhaps we could use the mean size of the v component of the lowest lower branch state as the threshold for activity. This would correspond to the situation of including the lower branch states of the three state DP model studied in the previous chapter. An alternative would be to choose the threshold such that it is between the approximate values of the upper and lower branch states; this would the equivalent of only including upper branch states in our definition of 'activity', which is the definition used in the majority of the previous chapter. The problem with trying to do this is evident in figure 4.2. Increasing the threshold causes a more or less constant decay in the density, such that there is seemingly no sensible place to put the threshold to only measure the upper branches. There is a slight shoulder to the curve at approximately 10, but it was decided that we would use the lower branch threshold condition instead (at least for calculations pertaining to the density). Thus the threshold was set at $v(x,t) = 1$.

Dynamical Decay of the Density. As in the previous chapter, we expect that at criticality we will see an asymptotic power-law decay when we are at the critical point, and the critical point has been found to be at approximately $R = 1.0169$. The density as a function of time at this value of R can be seen in figure 4.3. We then fit a power law to the tail of this curve to get a value for the dynamical exponent α, which was found to be equal to $0.1596(2)$ where the bracketed number represents the standard deviation. This is very close to the value we would expect for one dimensional DP, being $\alpha \approx 0.1595$.

Recall from the previous chapter that $\alpha = \beta/\nu_{\|}$, therefore if we can calculate either one of β and $\nu_{\|}$ we can use this together with α to find the other; to that end, we can calculate the turbulent fraction as a function of R as a means to calculate β, remembering that we expect the turbulent fraction to increase above the critical point as $(R - R_c)^{\beta}$. This is the method used by Lemoult *et al.* to calculate β in their experiments [35]. The values of the turbulent fraction are found by letting the system evolve for a time of 250,000, and then average the density of the final 10,000 time steps. Figure 4.4 shows the result of this calculation, and the exponent is again

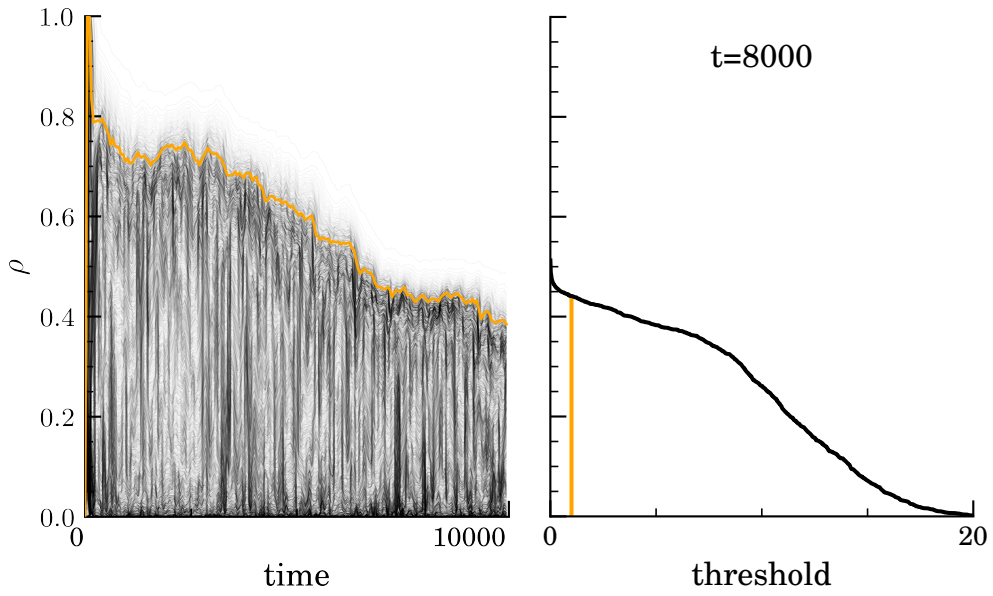

Figure 4.2: Plots used to help in determining a sensible place to put the threshold for what is thought of as 'activity. On the left is a plot of density as a function of time, for a range of thresholds between 0 and 20 - if there was a clear clustering of these curves it might suggest a good place to place the threshold. However there is a fairly smooth variation in the density as the threshold increases, as can be more clearly seen in the graph on the right. This makes it difficult to choose a place for the threshold which would only include the upper branch states using this method. In both cases the threshold value of 1 is marked in orange.

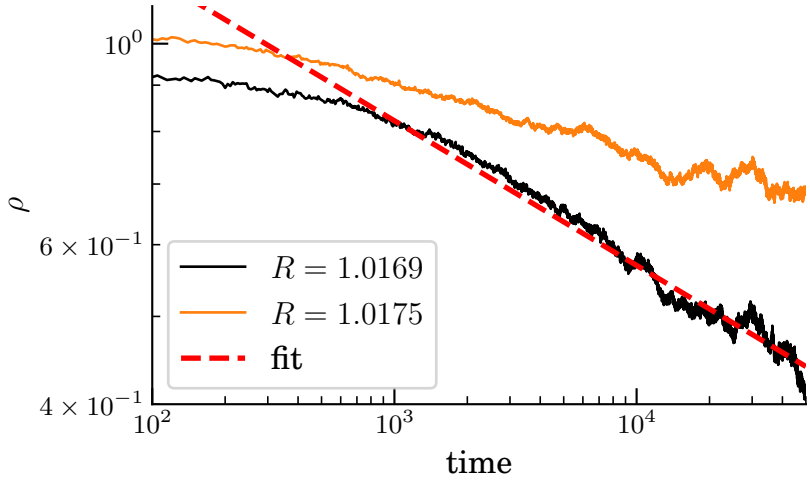

Figure 4.3: The decay of the turbulent fraction can be used to find the critical point. We expect to see asymptotic power-law behaviour at criticality (due to scale invariance at the transition). The calculated value of the critical point is $R = 1.0169$, and a power law fit to the tail of this curve has also been calculated, to give a value of the exponent α.

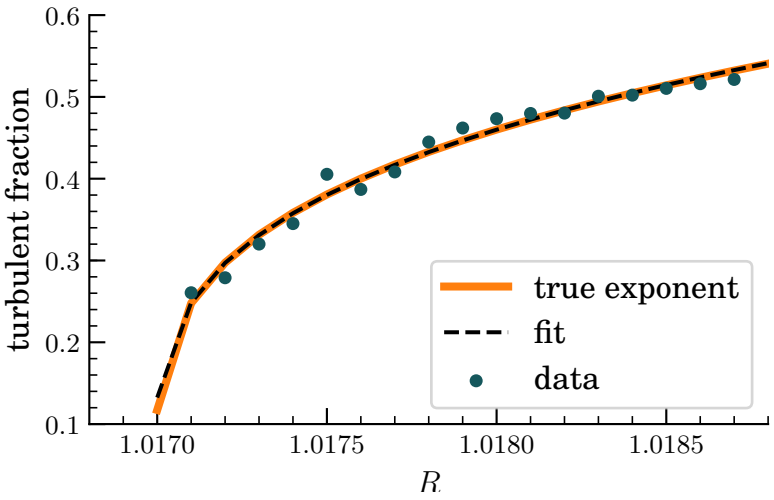

Figure 4.4: The long-time turbulent fraction as a function of R, showing the fit to obtain the β as well as a fit using the reference value of β for directed percolation.

in very close agreement with the DP value, which is also plotted for comparison. The reference DP value is $\beta \approx 0.276$ and the exponent as measured in these calculations in $0.270(3)$, where again the bracketed number represents the standard deviation of the fit. We can therefore simply divide our value for β by our value for α to get $\nu_{\parallel}$, which turns out to be $1.69(1)$, again being close to the DP value $\nu_{\parallel} \approx 1.733$.

We now have one more independent critical exponent to measure, for which we are going to require spatial information. For this we will introduce the *empty interval exponents*.

4.2.2 EMPTY INTERVAL EXPONENTS

These exponents are related to the distribution of laminar domains at criticality, which are expected to follow a power-law distribution. There is an exponent for the distribution of the *spatial* extent of laminar domains, and another one for the distribution of the *temporal* extent of those domains. We only require the spatial exponent to verify the universality class, but both distributions have been calculated. I will now give an overview for what these exponents are, and how they have been calculated.

Laminar Regions - Spatial. In order to calculate the distribution of the spatial extent of laminar domains we can use the same saved runs as were used to calculate the turbulent fraction, with each site at each time labelled as inactive or active according to if the value of the field v is above the threshold value, as described above. One thing was changed however - to increase the absolute number of laminar

domains we chose a higher threshold value, being $v = 10$ which is the approximate location of the 'shoulder' seen in figure 4.2. This was done to allow more data points to be found from the same information, because we expect to see more laminar regions. We then take slices of the run in time, this being a list of values of ones and zeros, representing active and inactive respectively. As there are periodic boundary conditions we 'roll' the slices until we have a 1 at the start of the slice - if there is no active site anywhere in the slice then we do not report any values for that slice as this means the run has died. We then find the length of all unbroken sequences of inactive sites and count how many sequences there are of each length, and repeat this for ten thousand slices near the end of each run, with the runs being allowed to evolve for $\approx$ 250,000 time units each. This gives us a distribution for the spatial extent of laminar domains, as depicted in figure 4.5

Laminar Regions - Temporal. The method for calculating the distribution of the temporal extents of laminar regions is very similar to that of the spatial extent, except the slices are taken at for a range of values of the time for each spatial point on the lattice. This calculation is done on the same section of lattice as that for the spatial distribution. One slight difference in the calculations is that there is of course no equivalent of the periodic boundary conditions seen for the spatial distribution, so instead of rolling the slice we simply remove any trailing inactive sites. The distribution from this analysis can be seen in figure 4.6.

Extracting Exponents. Correctly fitting a power-law to a distribution is a non-trivial action, and some of the methods traditionally used are not sensible ways to extract the exponents, as outlined by Clauset *et al.* in [143]. Therefore, to extract coefficients from the distributions I have used a python package `powerlaw` [144] which implements the algorithm of Clauset *et al.*.

4.2.3 RESULTS

Figures 4.5 and 4.6 show respectively the distributions of the spatial and temporal extent of the laminar regions, measured at $R = 1.0169$, the nearest value of R to the critical value for which data was collected. Also included in the figures are the fit using the `powerlaw` package. The spatial empty interval exponent, $\mu_\perp$, is found to have a value of $1.749(4)$, in excellent agreement with the directed percolation value of 1.748. The relationship between this empty interval exponent and the more usual DP exponent $\nu_\perp$ is given by the expression $\nu_\perp = (2 - \beta)/\mu_\perp$ [35] and using this expression we find that $\nu_\perp = 0.99(1)$ close to the DP value of $\nu_\perp \approx 1.097$. We have now calculated the three independent critical exponents of the DP transition and seemingly verified the universality class. The results for the three exponents are

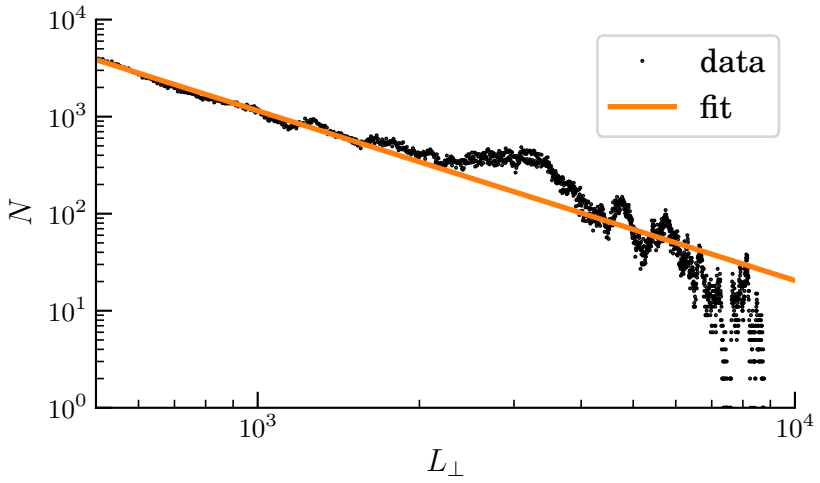

Figure 4.5: The distribution of the spatial extent of laminar domains, at the critical value of $R = 1.0169$. The power-law exponent as found by the `powerlaw` package is also plotted. This distribution is in excellent agreement with the empty interval exponent for directed percolation.

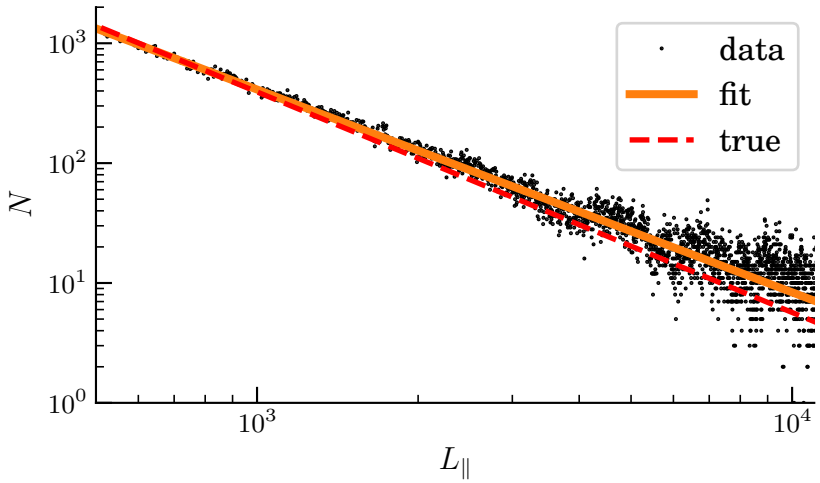

Figure 4.6: The distribution of the temporal extent of laminar domains, at the critical value of $R = 1.0169$. Also shown are the distribution from the measured value of the exponent and the reference value of the exponent, shown a non-negligible deviation. The source of this deviation is unclear.

Exponent	Measured	True
β	0.270(3)	0.2765
$\nu_{\parallel}$	1.69(1)	1.734
$\nu_{\perp}$	0.99(1)	1.097

Table 4.1: The three independent critical exponents as calculated for the extended Kuramoto-Sivashinsky equation in a large domain. The good agreement between the measured and reference values suggests that the eKSE belongs to the DP universality class.

summarised in table 4.1 and show quite good agreement with the DP values.

However, the situation for the temporal exponent, $\mu_{\parallel}$, is not so good. The measured value is $1.705(1)$, which is compared to the DP value for this exponent, approximately 1.84. The reason for this disparity is not immediately clear - as can be seen in figure 4.6 the deviation from the expected fit seems to indicate that the distribution we are seeing is skewed towards long times compared to what we would expect to see from the DP exponent. It is not clear to me why this would be the case, given the details of the simulations as outlined. This is especially strange given that we have already calculated β and $\nu_{\parallel}$, and these should be related to the temporal empty interval exponent by a simple expression: $\nu_{\parallel} = (2 - \beta)/\mu_{\parallel}$. The reason for this measured discrepancy remains unexplained but is possibly due to not letting the system equilibriate for a sufficient length of time, and therefore the slices through time reach back far enough that there is behaviour related to non-universal transients encoded in the distribution. However, this same limitation would presumably hold for the spatial empty interval exponent, which was found to have a value very close to the one expected.

4.3 SINGLE SEED SPREADING

As we have seen in the previous chapter, there is another method by which we can probe the universal behaviour of a DP transition, by using localised initial conditions and observing the spreading behaviour. In this section I will report some surprising observations about this type of initial condition.

4.3.1 INITIAL CONDITIONS

Unlike the situation for DP, it is more unclear when using a PDE what to use as an initial condition for this type of analysis. To answer this question it may be instructive to look at the approximate size of clusters found when evolving the system in time. Figure 4.7 shows a close up of the example shown in figure 4.1, overlaid with a grid of lines separated in space by a distance of 24π. This was the

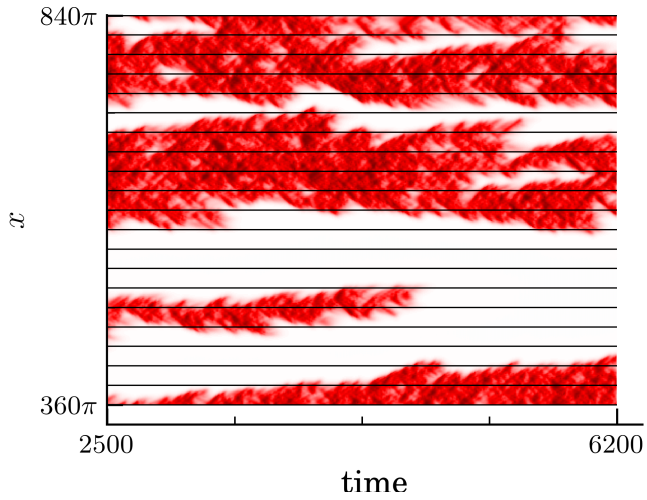

Figure 4.7: A closer look at a section from the example shown in figure 4.1 with gridlines spaced 24π apart. It seems that 24π is a reasonable size to take for the size of an active region to use as a single seed initial condition.

size of the domain used in chapter 2, the behaviour of which suggested it might be approximately a minimal flow unit for this system. The fact that the approximate size of single 'fingers' of chaos is roughly matched by this grid suggests that 24π may be a reasonable choice of size for our initial chaotic perturbation. Initial conditions are then formed in a similar manner to those for the homogeneous initial conditions, but with the addition of one extra step. The system is again started with a fully active initial condition at $R = 2.0$, then evolved for time t before being quenched to the desired value of R. However, before time evolution continues all of the sites not within the 24π centre of the lattice are set to zero. This is now the initial condition (note that the time iteration method has to be restarted with an explicit Euler step rather than the Adams-Bashforth step). Evolving in time we see spreading behaviour very reminiscent of directed percolation, as shown in figure 4.8.

Recall from the previous chapter that at criticality the survival probability of spreading DP decays as a power-law with exponent δ, where δ is equal to $\beta/\nu_{\parallel}$. Therefore, given that we have already calculated β for this system we could use this decay to calculate $\nu_{\parallel}$, which is related to the empty interval exponent $\mu_{\parallel}$ by the expression $(2 - \beta/)\nu_{\parallel}$.

4.3.2 SURVIVAL PROBABILITY

In order to calculate the survival probability of these spreading runs we require a method to determine the time of death of the run. The method used in chapter 2 (looking for the last increase in the norm of u) will no longer work here, because

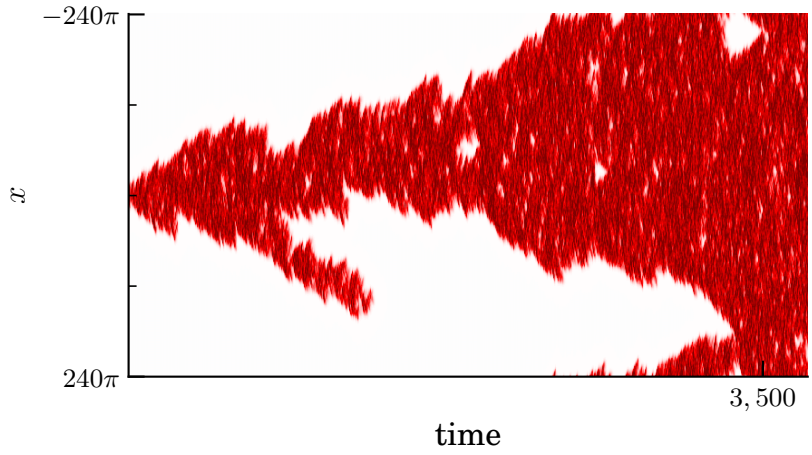

Figure 4.8: An example of a run started from a single seed in a domain of size 240π, at $R = 1.02$ (above the critical point). The chaos spreads and eventually covers the whole domain.

there are large sections of the lattice which are dead, so the norm can just decay gradually, even if there is still activity somewhere in the domain. Therefore a new strategy was devised - death is defined as the last time at which there is an increase at any of the lattice points. For similar reasons as those described for the turbulent fraction calculations the field v is used instead of the field u. The death times can then be used to construct a survival probability curve, as shown in figure 4.9.

We would expect this curve to obey a power-law behaviour with the same dynamical exponent as the decay of the density, if the rapidity reversal symmetry holds true here, as we would expect it to for a DP transition. However, the observed survival probability curve hugely from what we would expect to see if rapidity reversal is to hold. The reason for this discrepancy is again unclear; the large decay exponent indicates that the runs are dying more quickly than we would expect - this is perhaps caused by the relatively small size of the lattice, being roughly 100 minimal flow units in diameter. Having less space to move into means that the system has fewer opportunities to split and birth more chaos. A finite-size scaling analysis could be performed to check if this is the cause, and would be a natural place to continue this analysis in further work.

The fact that rapidity reversal symmetry is not observed makes it impossible to calculate the non-universal proportionality factor μ^2 as was discussed in the previous chapter. This quantity is related to how far you have to scale one curve until the tail is close to the tail of the other, and the fact is that the tails of the survival probability and the decaying density will never line up with each other.

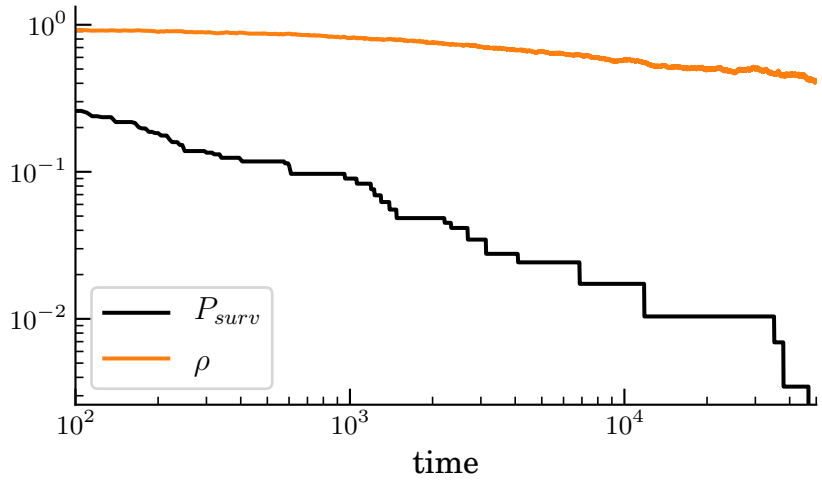

Figure 4.9: Survival probability curve, P_{surv}, for spreading runs at $R = 1.0169$ plotted alongside the decay of the turbulent fraction, ρ. Given rapidity reversal symmetry we would expect these two curves to asymptotically share a dynamical exponent, which would look on this plot as if the straight lines were parallel. However, this is clearly not what is observed, and the dynamical exponent related to the survival probability is approximately ten times larger than the DP value.

4.4 CONCLUSION

The extended Kuramoto-Sivashinsky equation studied in chapter 2 has been numerically simulated in a spatially extended domain. Critical exponents have been calculated in order to determine if the system belongs to the Directed Percolation universality class, with mixed success. Calculating the exponent β and $\mu_\perp$ worked as planned, and show good agreement with the reference values for $1 + 1D$ directed percolation. The value of $\mu_\parallel$ measured by finding the distribution of the temporal extension of laminar domains was further from the reference value, although measuring this exponent by first calculating the dynamical exponent related to the decay of the density at criticality gave a good agreement. From these analyses we can conclude that the system does indeed belong to the directed percolation universality class.

An attempt was made to calculate the non-universal proportionality factor μ as discussed in the previous chapter. However, this proved unsuccessful due to the surprisingly observed behaviour of the survival probability at criticality. The dynamical exponent related to this behaviour was found to be significantly different to the DP value, which made the prospect of measuring μ impossible. It is unclear why the survival probability curves are so different to the ones we might expect to see.

5 THESIS CONCLUSION

This thesis began with an investigation into an extension of the damped Kuramoto-Sivashinsky equation which was constructed by Becherer *et al.* [120] to exhibit a subcritical transition to spatiotemporal chaos. This system of partial differential equations was found to exhibit transient chaos with an exponential distribution of lifetimes. These lifetimes scale super-exponentially with a control parameter R, which quantifies the degree of nonlinear interaction. Coherent structures were found using a Newton method, and pseudo-arclength continuation allowed these structures to be followed around the saddle-node where they are created. This produced a bifurcation diagram for the system showing a bifurcation from infinity scenario (as expected by construction). The linear stability of the coherent structures was tested and the lowest branches were found to have a small number of unstable eigenvalues, although no lower branch state was found with only one unstable eigenvalue. The upper branches have more unstable eigenvalues and seem to organise the majority of the dynamics when turbulent. There were upper branches very far from the laminar region which had few unstable eigenvalues (as low as having only one unstable eigenvalue) which seems to bound the system from above. The differing dynamical roles played by the upper and lower branches motivated the second investigation.

A three state directed percolation model was introduced, adding a state between active and inactive through which a site must pass to 'relaminarise' to the absorbing state. Its behaviour was constructed to mimic the observed behaviour of the lower branches. The universality class of this model was then checked for a range of values of a control parameter which controls the strength of the 'bouncing' behaviour. No deviation was observed in any of the critical exponents, indicating that the universality class remains unchanged by the addition of the third state. Given that the parallel shear flows discussed are known to belong to the DP class this is reassuring that the bouncing dynamics could be present, but just undetectable by DP-style analyses. One non-universal quantity was found to deviate as the bounce probability was increased: the proportionality factor relating to the rapidity reversal symmetry was found to change as b was increased. However, due to the non-

universal nature of this quantity it is difficult to know how to measure it in any sensible manner for a real hydrodynamic flow. Its dependence on the absolute value of the turbulent fraction means it will change depending on how the threshold value used for determining 'activity'.

Finally, the extended KS equation explored in the first investigation was simulated in an extended spatial domain, to verify its belonging to the DP class. The three independent critical exponents were measured and found to be in agreement with the DP values, but some of the calculations yielded surprising results - particular the survival probability from a single seed. The measured dynamical exponent was found to be radically different than is expected from DP, indicating a break in rapidity reversal symmetry. However, it is unclear if this is a true deviation from DP or an error in calculation. Given the qualitative similarities with the DP dynamics (and the robustness of the DP class) it seems likely that an error has been made in calculation.

The evidence points towards the extended Kuramoto-Sivashinsky equation belonging to the same family of flows as pressure driven pipe flow and plane Couette flow. Given the fact that it is based of the Kuramoto-Sivashinsky equation, which is known to be possibly the simplest chaotic partial differential equation [119] it is possible that it represents one of the simpler members of this family.

A SUPPLEMENTARY DP FIGURES

Repeating the calculations outlined in chapter 3 for each value of b creates many graphs, and so to streamline the chapter I have placed them in this appendix.

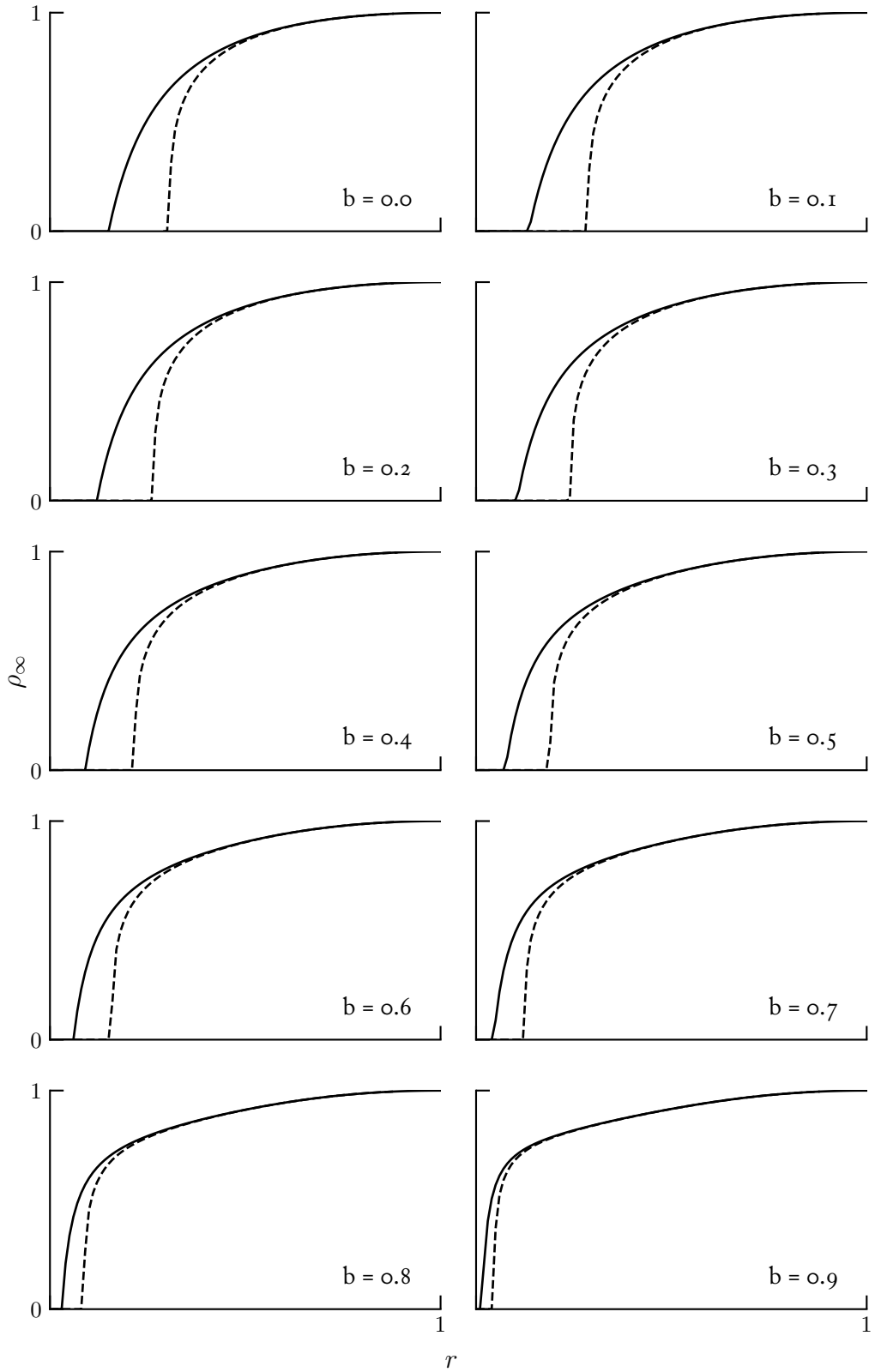

Figure A.1: Grid of graphs comparing the mean field theory prediction for the steady state density compared to the numerical measurement. The mean field theory prediction is the solid line and the numerical measurement is the dashed line.

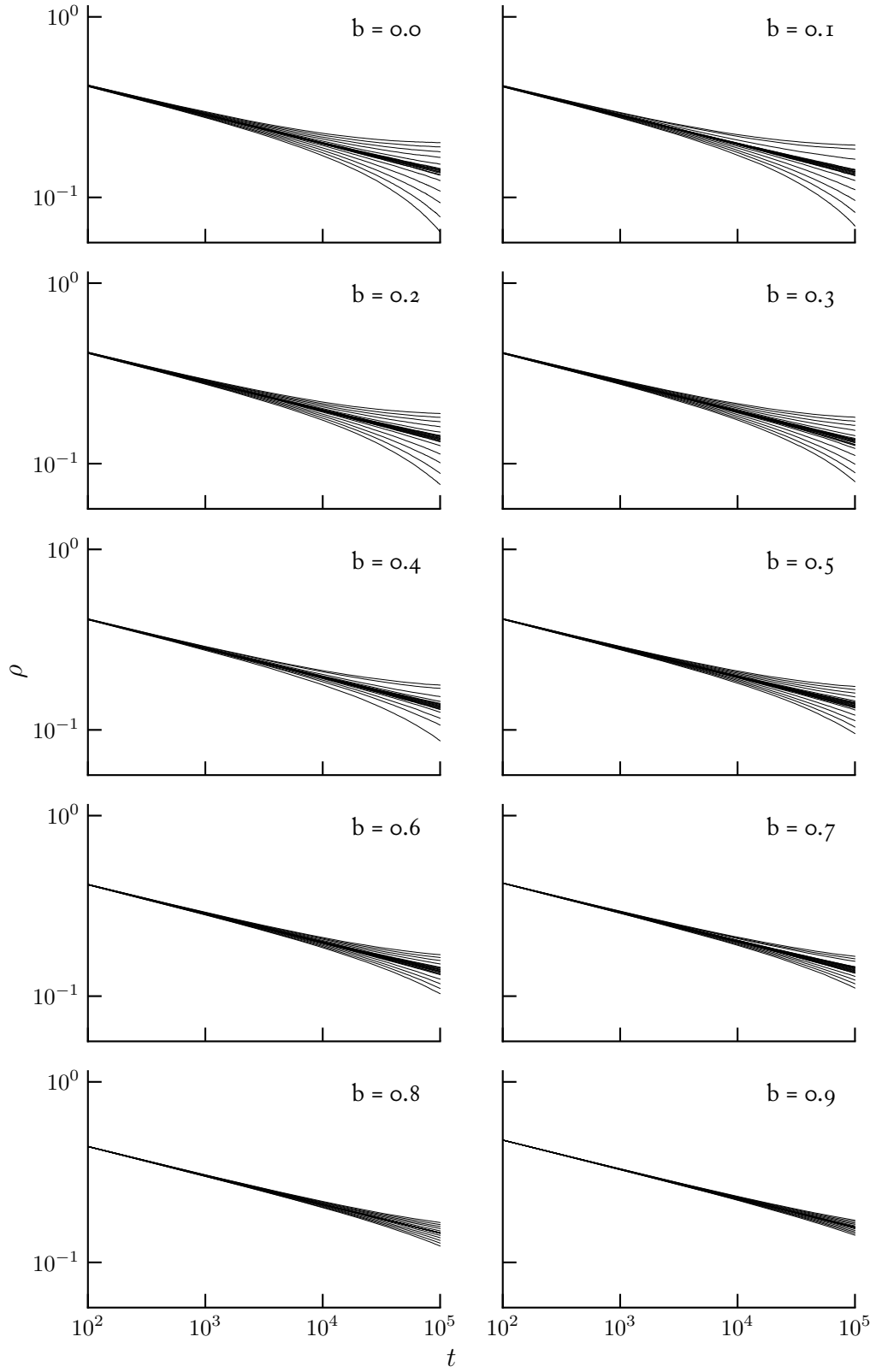

Figure A.2: Density curves for all values of b for a range of values of r near the critical point. The values of r get closer together as b increases because they are calculated as a percentage distance to the approximate critical point.

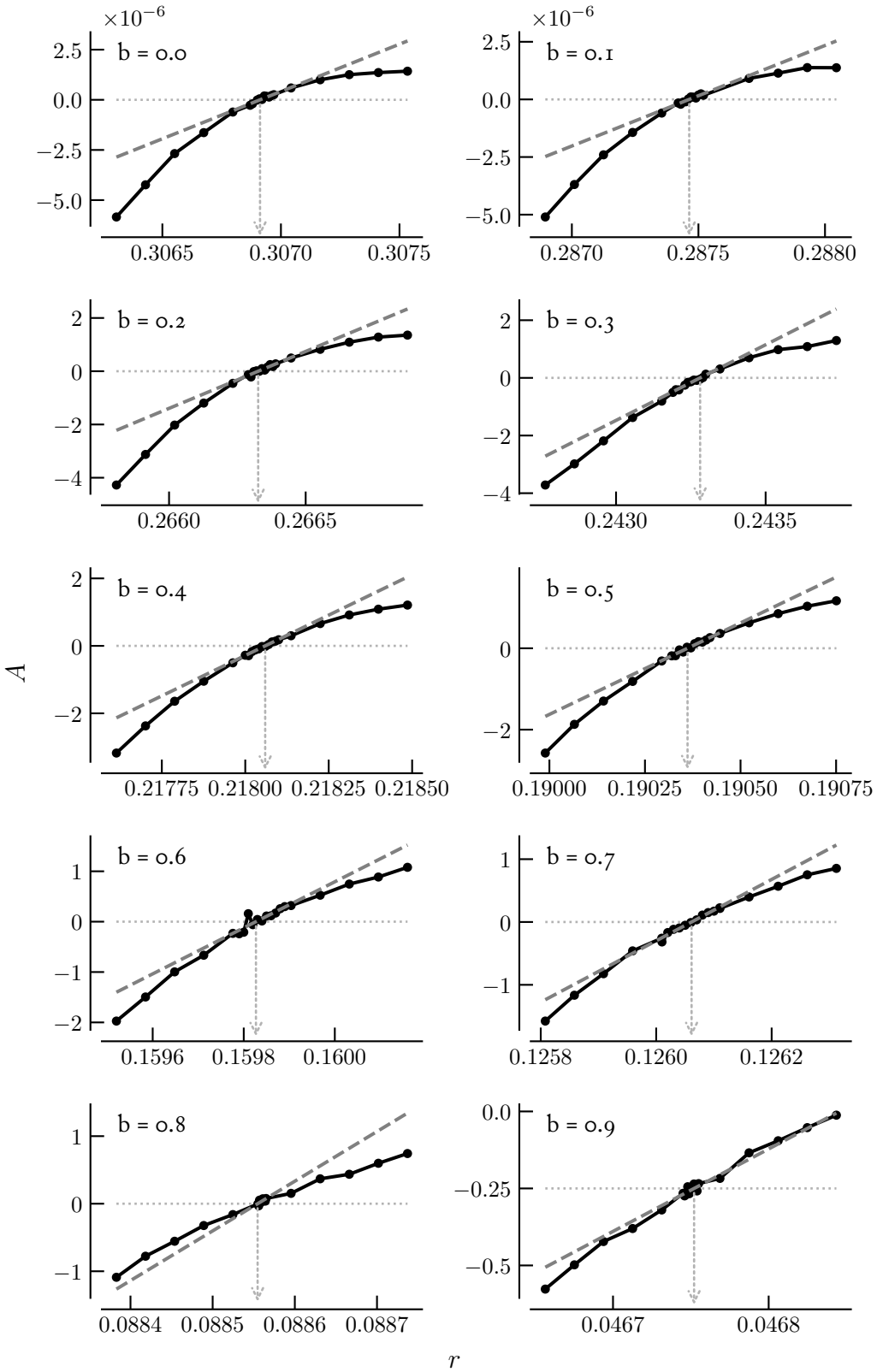

Figure A.3: Grid of graphs of A for all values of b, with linear fits of the critical region, used in finding the location of the critical point. Note that the y axis in each figure is in scientific notation with exponent 10^{-6}

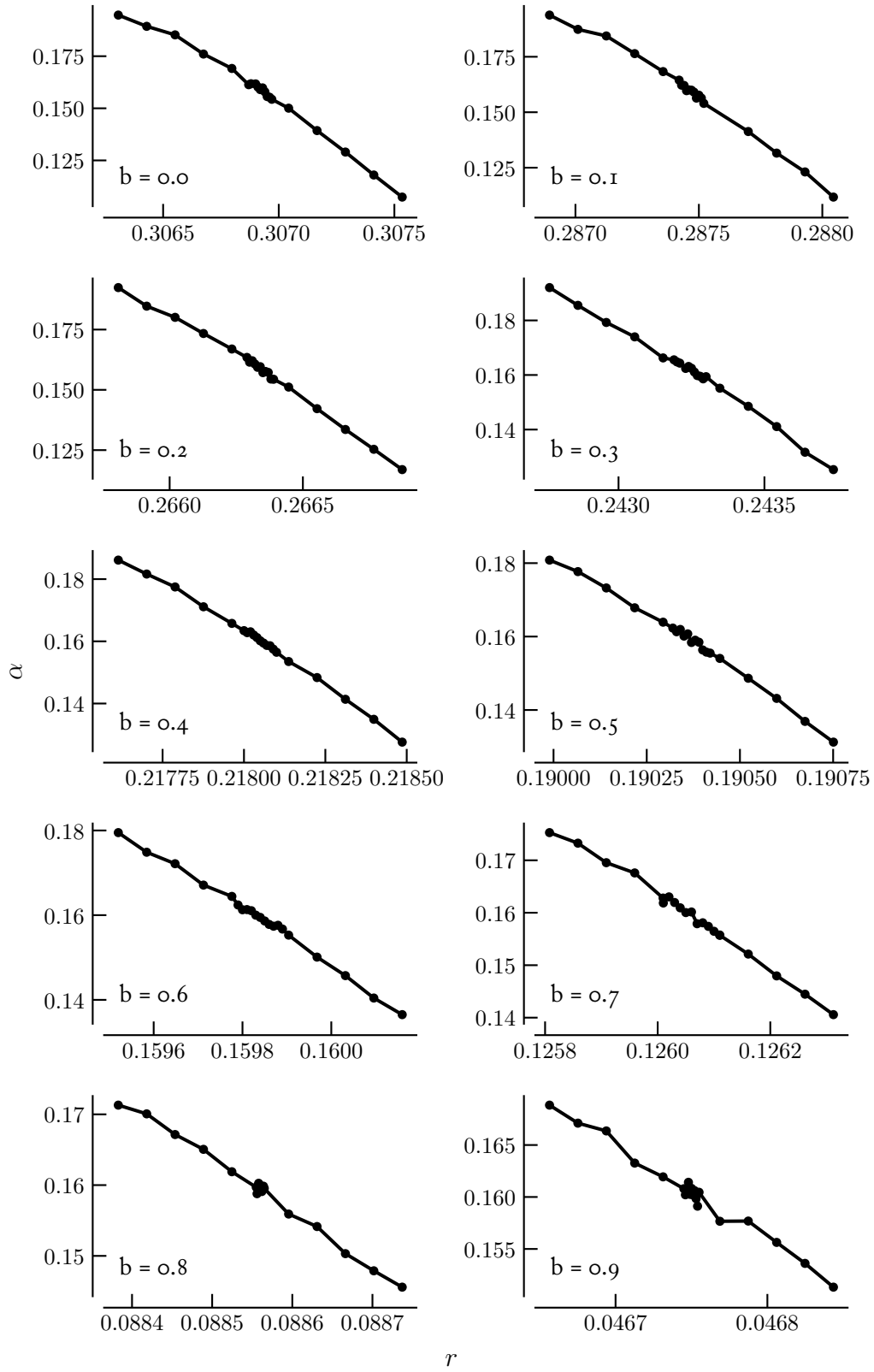

Figure A.4: Grid of graphs of α for all values of b. Linear fits of the central points are used (along with the measured value of r_c) to find the value of α at the critical point.

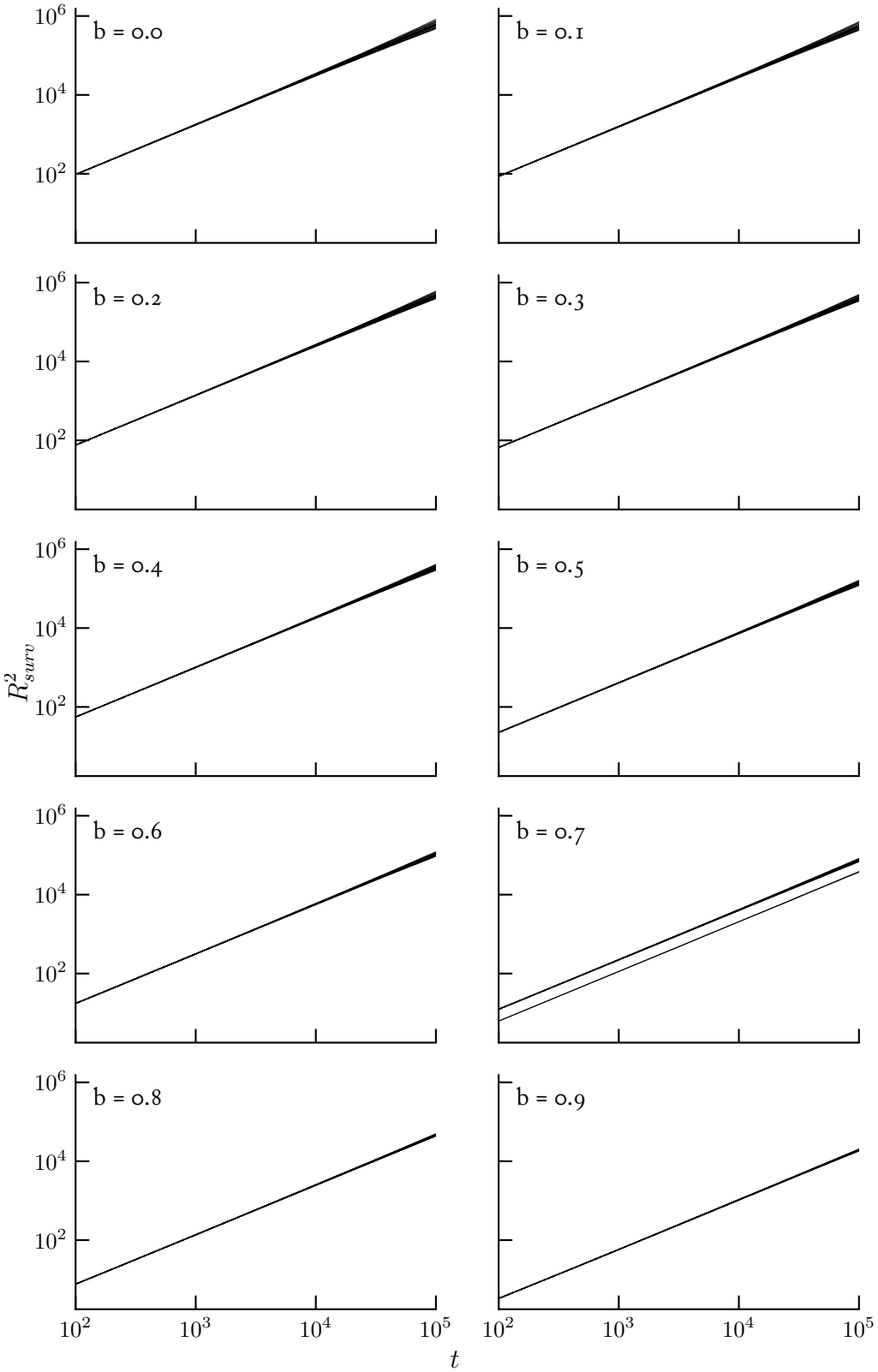

Figure A.5: Grid of graphs of R^2_{surv} for all values of b. These curves are used to extract a value of the dynamical exponent z and the fact that there is not much spread between them could explain part of why there is a larger uncertainty in the z measurement.

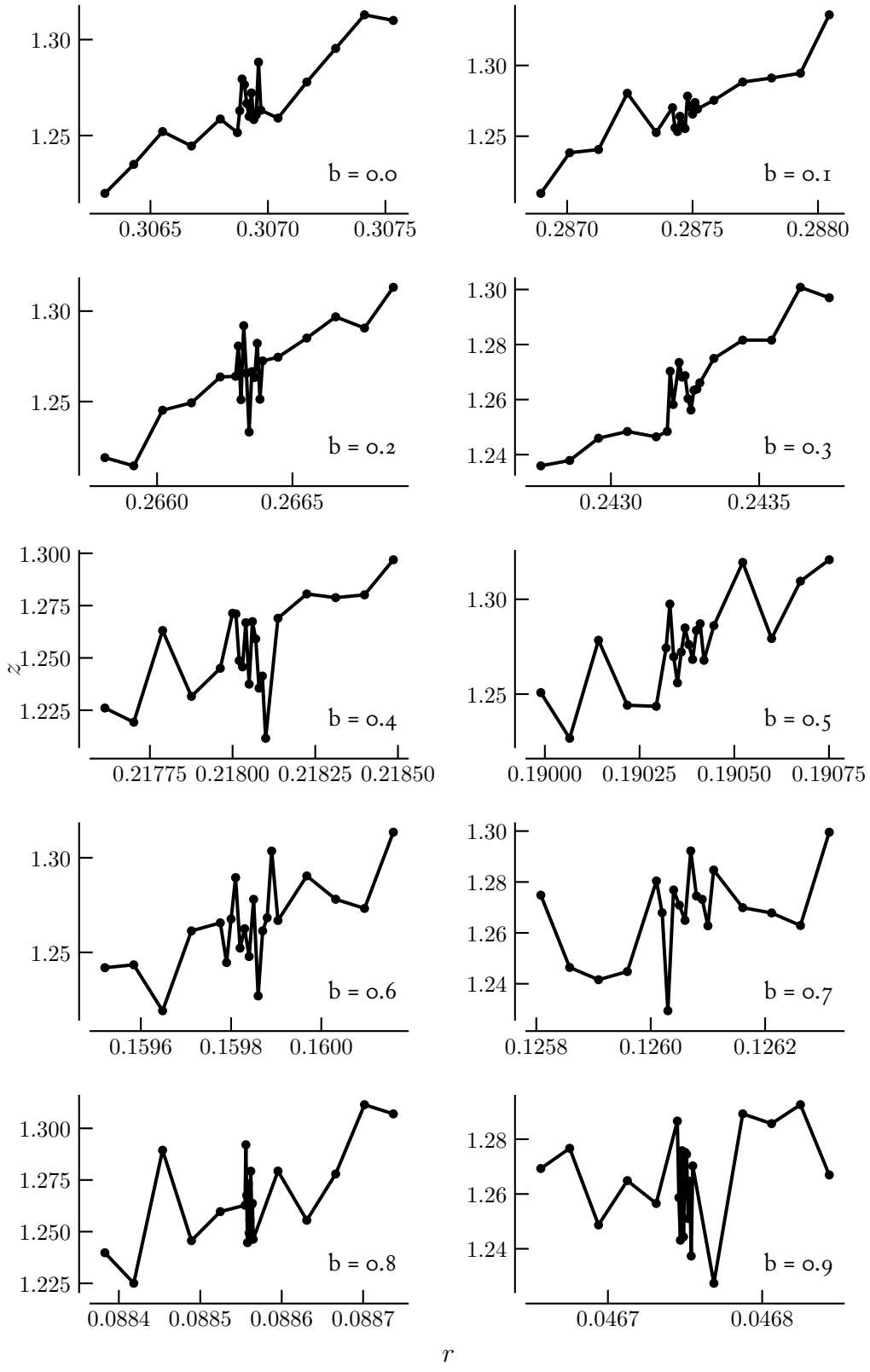

Figure A.6: Grid of graphs of z for all values of b. This dynamical exponent is much less consistent than α, perhaps due to the fact that the mean square spreading seems to be less sensitive to deviation from the critical point than $\rho(t)$ does.

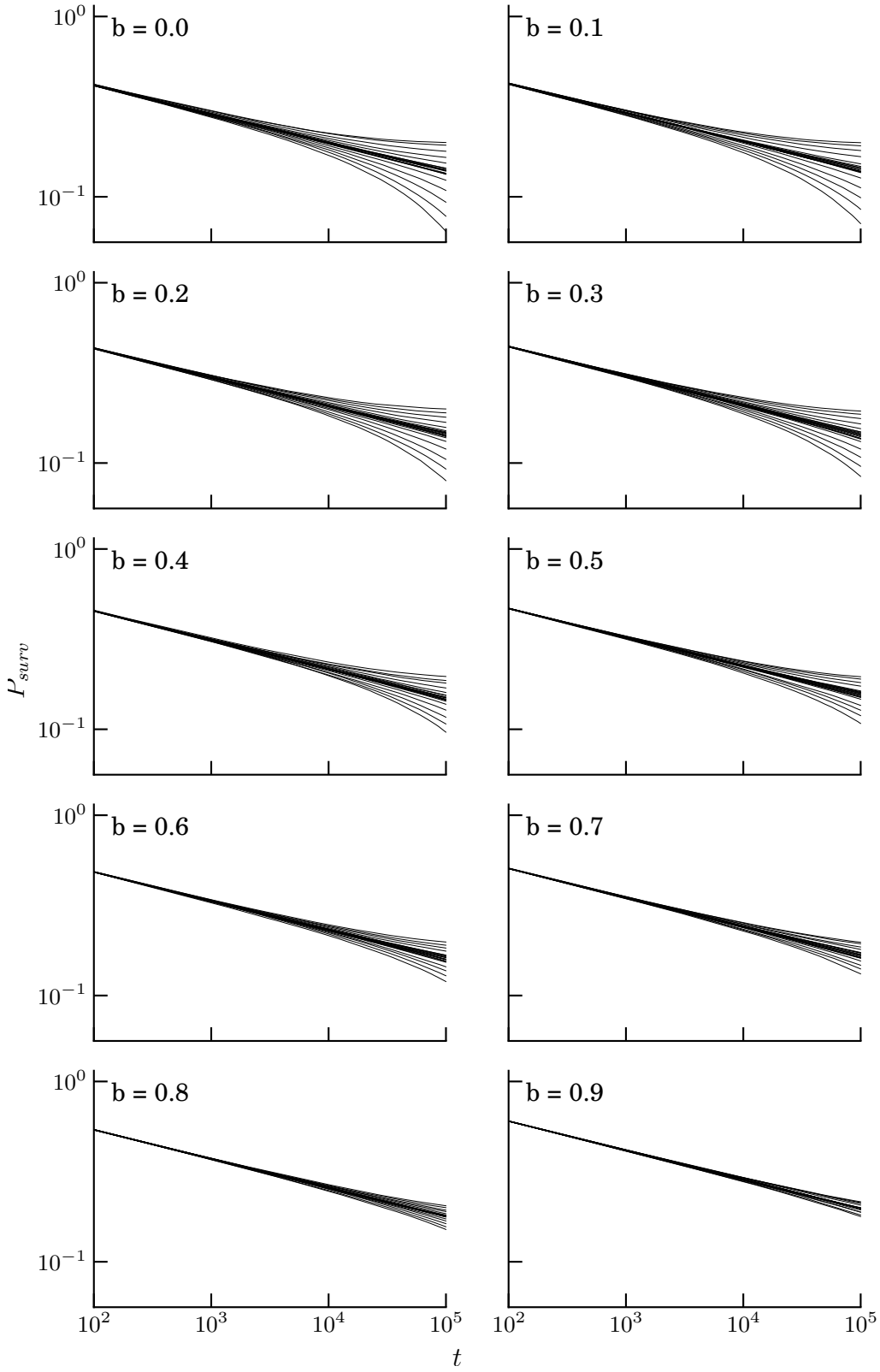

Figure A.7: Grid of graphs of the survival probability of a single seed for all values of b. These can be used to verify the rapidity reversal symmetry, and also to calculate the factor μ.

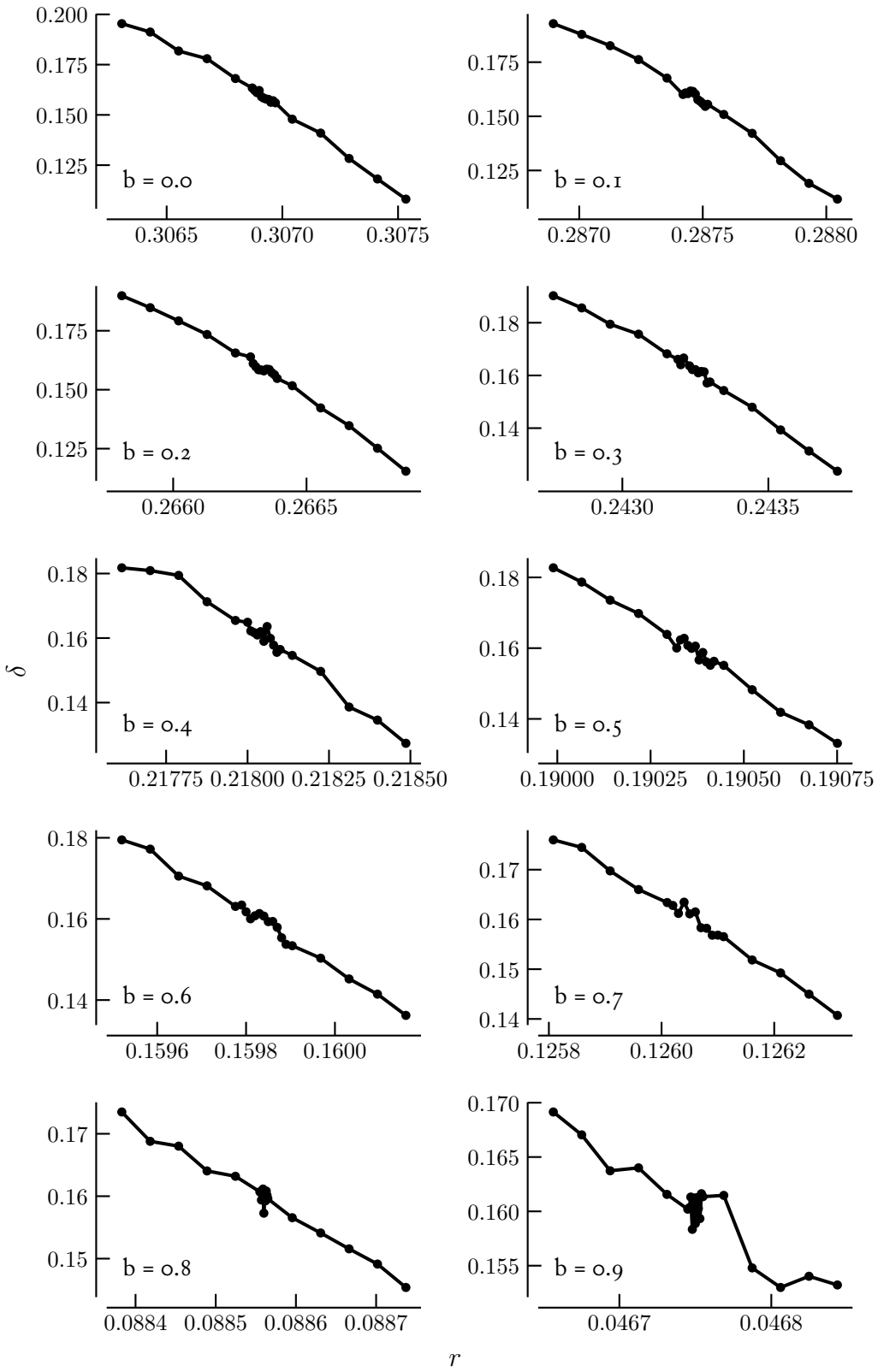

Figure A.8: Grid of graphs of δ for all values of b, the exponent δ can be used to check the rapidity reversal symmetry, where we expect it should be the same as α.

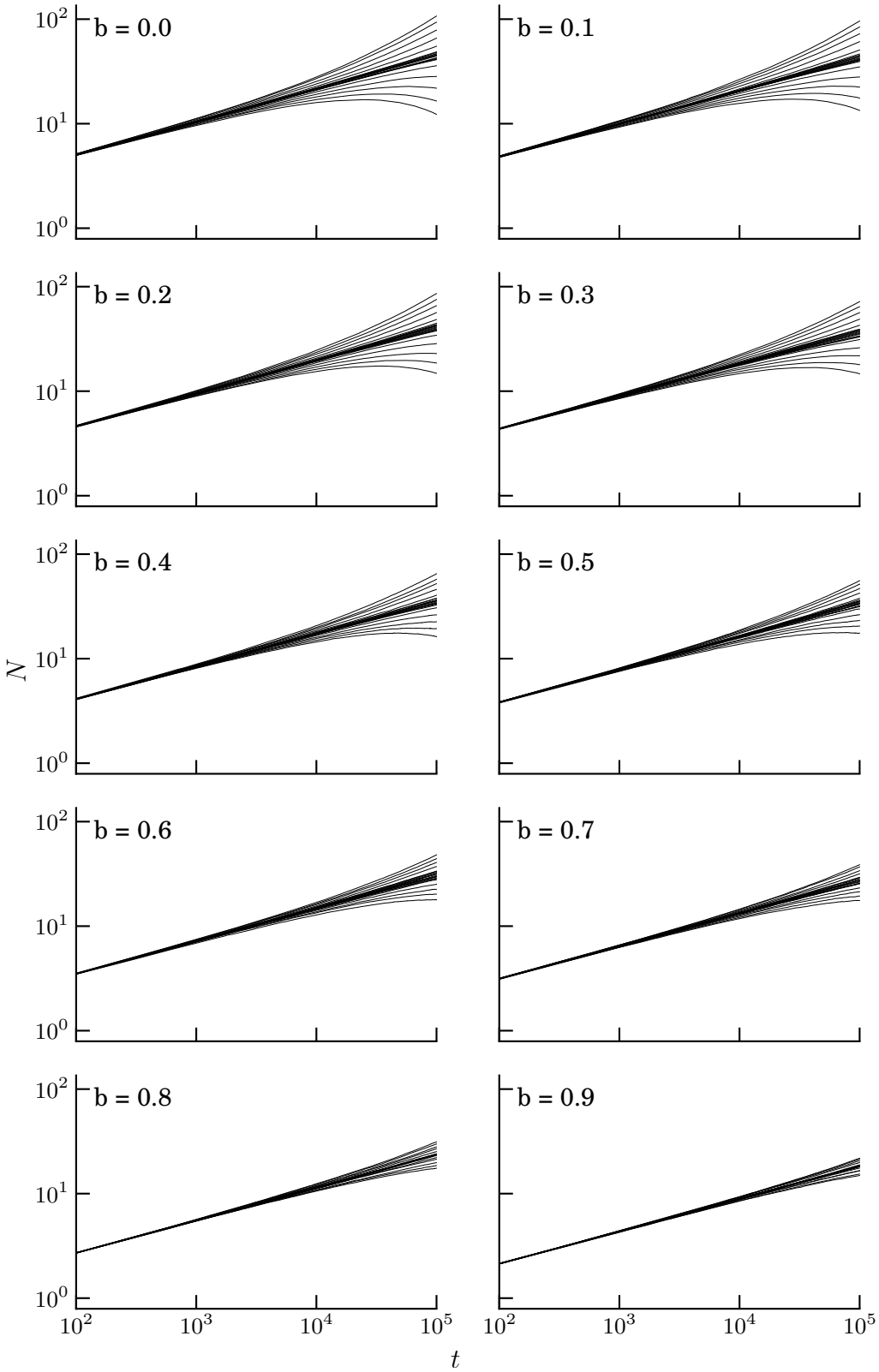

Figure A.9: Grid of graphs of N for all values of b. These graphs (of N and of Θ are included mostly for interest, as the value of Θ is not used in the calculation of the independent critical exponents.

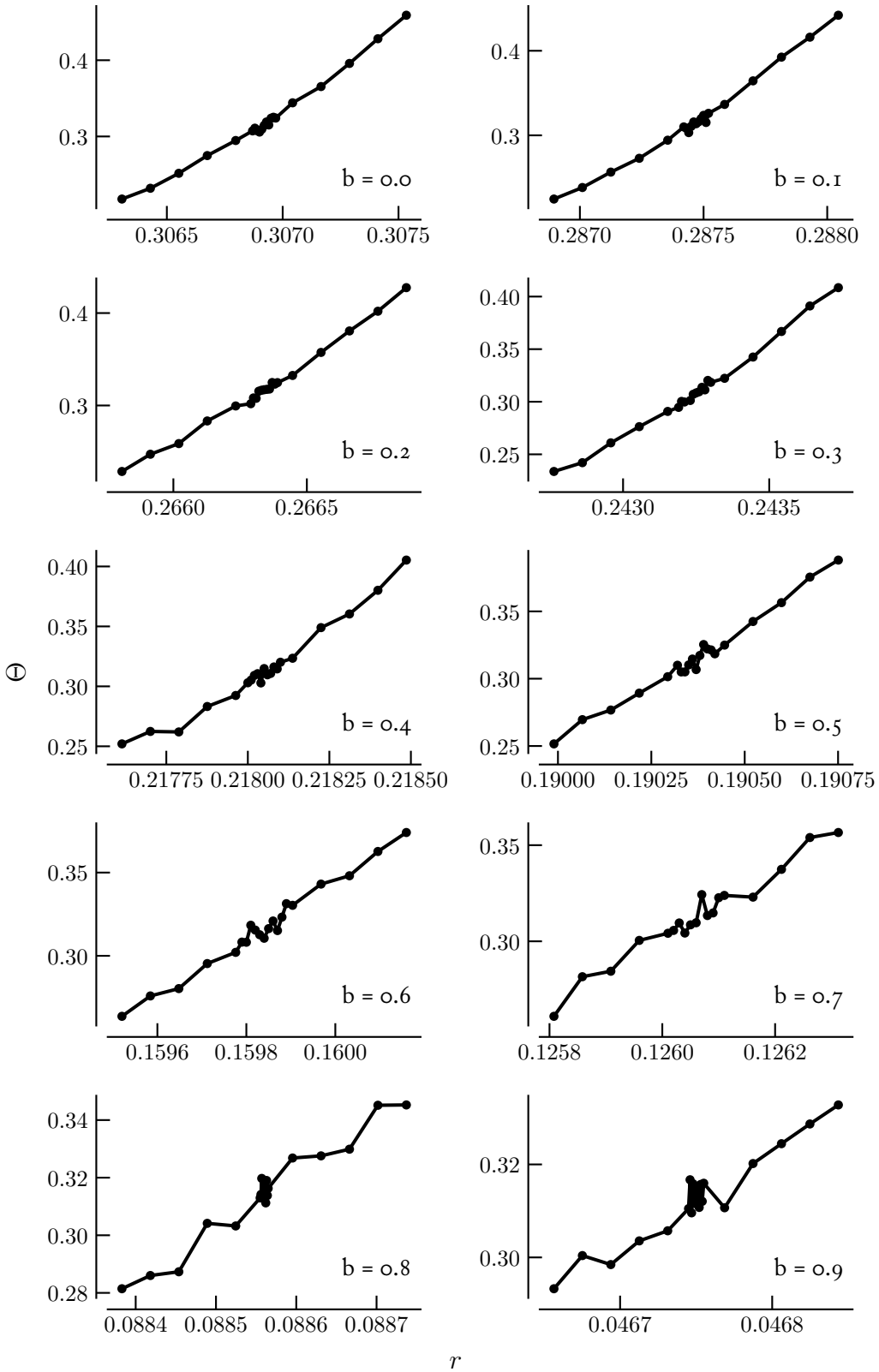

Figure A.10: Grid of graphs of Θ fits as a function of r.

BIBLIOGRAPHY

[1] Osborne Reynolds. An Experimental Investigation of the Circumstances Which Determine Whether the Motion of Water Shall Be Direct or Sinuous, and of the Law of Resistance in Parallel Channels. *Philosophical Transactions of the Royal Society of London*, 174:935–982, 1883.

[2] Stephen M. Stigler. Stigler's Law of Eponymy. *Transactions of the New York Academy of Sciences*, 39(1 Series II):147–157, 1980.

[3] Harold Salwen, Fredrick W. Cotton, and Chester E. Grosch. Linear stability of Poiseuille flow in a circular pipe. *Journal of Fluid Mechanics*, 98(02):273, 1980.

[4] Á. Meseguer and Lloyd N. Trefethen. Linearized pipe flow to Reynolds number 10^7. *Journal of Computational Physics*, 186(1):178–197, 2003.

[5] V. A. Romanov. Stability of plane-parallel Couette flow. *Functional Analysis and Its Applications*, 7(2):137–146, 1973.

[6] A. Riols, F. Rincon, C. Cossu, G. Lesur, P.-Y. Longaretti, G. I. Ogilvie, and J. Herault. Global bifurcations to subcritical magnetorotational dynamo action in Keplerian shear flow. *Journal of Fluid Mechanics*, 731:1–45, 2013.

[7] V. Dallas and A. Alexakis. Self-organisation and non-linear dynamics in driven magnetohydrodynamic turbulent flows. *Physics of Fluids*, 27(4):045105, 2015.

[8] Moritz F. Linkmann and Alexander Morozov. Sudden relaminarization and lifetimes in forced isotropic turbulence. *Physical Review Letters*, 115(13):6, 2015.

[9] F. Van Wyk, E. G. Highcock, A. A. Schekochihin, C. M. Roach, A. R. Field, and W. Dorland. Transition to subcritical turbulence in a tokamak plasma. *Journal of Plasma Physics*, 82(6):905820609, 2016.

[10] Lennaert van Veen and Susumu Goto. Sub critical transition to turbulence in three-dimensional Kolmogorov flow. *Fluid Dynamics Research*, 48(6):061425, 2016.

[11] H. Sohanian Haghighi and A. H. D. Markazi. A new description of epileptic seizures based on dynamic analysis of a thalamocortical model. *Scientific Reports*, 7(1):13615, 2017.

[12] Olivier Dauchot and Eric Bertin. Subcritical transition to turbulence: What we can learn from the physics of glasses. *Physical Review E - Statistical, Nonlinear, and Soft Matter Physics*, 86(3):036312, 2012.

[13] Lloyd N. Trefethen, Anne E. Trefethen, Satish C. Reddy, and Tobin A. Driscoll. Hydrodynamic Stability Without Eigenvalues. *Science*, 261(5121):578–584, 1993.

[14] F. Mellibovsky and A. Meseguer. Critical threshold in pipe flow transition. *Philosophical Transactions of the Royal Society A: Mathematical, Physical and Engineering Sciences*, 367(1888):545–560, 2009.

[15] Björn Hof, A. Juel, and T. Mullin. Scaling of the Turbulence Transition Threshold in a Pipe. *Physical Review Letters*, 91(24):244502, 2003.

[16] J. Peixinho and T. Mullin. Finite-amplitude thresholds for transition in pipe flow. *Journal of Fluid Mechanics*, 582:169, 2007.

[17] Paul Manneville. On the transition to turbulence of wall-bounded flows in general, and plane Couette flow in particular. *European Journal of Mechanics, B/Fluids*, 49(PB):345–362, 2015.

[18] Yohann Duguet, Antonios Monokrousos, Luca Brandt, and Dan S. Henningson. Minimal transition thresholds in plane Couette flow. *Physics of Fluids*, 25(8):084103, 2013.

[19] Ashley P. Willis and Rich R. Kerswell. Critical behavior in the relaminarization of localized turbulence in pipe flow. *Physical Review Letters*, 98(1):014501, 2007.

[20] Ulrich Brosa. Turbulence without strange attractor. *Journal of Statistical Physics*, 55(5-6):1303–1312, 1989.

[21] Holger Faisst and Bruno Eckhardt. Sensitive dependence on initial conditions in transition to turbulence in pipe flow. *Journal of Fluid Mechanics*, 504:343–352, 2004.

[22] Tobias M. Schneider, Bruno Eckhardt, and Jürgen Vollmer. Statistical analysis of coherent structures in transitional pipe flow. *Physical Review E - Statistical, Nonlinear, and Soft Matter Physics*, 75(6):066313, 2007.

[23] M. Avila, A. P. Willis, and B. Hof. On the transient nature of localized pipe flow turbulence. *Journal of Fluid Mechanics*, 646:127–136, 2009.

[24] Tobias M. Schneider and Bruno Eckhardt. Lifetime statistics in transitional pipe flow. *Physical Review E - Statistical, Nonlinear, and Soft Matter Physics*, 78(4):046310, 2008.

[25] T. Mullin and J. Peixinho. Transition to Turbulence in Pipe Flow. *Journal of Low Temperature Physics*, 145(1-4):75–88, 2006.

[26] Björn Hof, Jerry Westerweel, Tobias M. Schneider, and Bruno Eckhardt. Finite lifetime of turbulence in shear flows. *Nature*, 443(7107):59–62, 2006.

[27] Björn Hof, Alberto De Lozar, Dirk Jan Kuik, and Jerry Westerweel. Repeller or attractor? selecting the dynamical model for the onset of turbulence in pipe flow. *Physical Review Letters*, 101(21):214501, 2008.

[28] T. Mullin. Experimental Studies of Transition to Turbulence in a Pipe. *Annual Review of Fluid Mechanics*, 43(1):1–24, 2011.

[29] S Bottin, F Daviaud, P Manneville, and O Dauchot. Discontinuous transition to spatiotemporal intermittency in plane Couette flow. *Europhysics Letters (EPL)*, 43(2):171–176, 1998.

[30] Tobias M. Schneider, Filippo De Lillo, Juergen Buehrle, Bruno Eckhardt, Tim Dörnemann, Kay Dörnemann, and Bernd Freisleben. Transient turbulence in plane Couette flow. *Physical Review E - Statistical, Nonlinear, and Soft Matter Physics*, 81(1):015301, 2010.

[31] Dirk Jan Kuik, C. Poelma, and Jerry Westerweel. Quantitative measurement of the lifetime of localized turbulence in pipe flow. *Journal of Fluid Mechanics*, 645:529, 2010.

[32] M. Avila, A. P. Willis, and B. Hof. On the transient nature of localized pipe flow turbulence. 2009.

[33] Nigel Goldenfeld, Nicholas Guttenberg, and Gustavo Gioia. Extreme fluctuations and the finite lifetime of the turbulent state. *Physical Review E - Statistical, Nonlinear, and Soft Matter Physics*, 81(3):035304, 2010.

[34] A. Prigent and Olivier Dauchot. Transition to versus from turbulence in subcritical Couette flows. *IUTAM Symposium on Laminar-Turbulent Transition and Finite Amplitude Solutions*, pages 1–25, 2005.

[35] Grégoire Lemoult, Liang Shi, Kerstin Avila, Shreyas V. Jalikop, Marc Avila, and Björn Hof. Directed percolation phase transition to sustained turbulence in Couette flow. *Nature Physics*, 12(3):254–258, 2016.

[36] I. J. Wygnanski and F. H. Champagne. On transition in a pipe. Part 1. The origin of puffs and slugs and the flow in a turbulent slug. *Journal of Fluid Mechanics*, 59(2):281–335, 1973.

[37] Mina Nishi, Bülent Ünsal, Franz Durst, and Gautam Biswas. Laminar-to-turbulent transition of pipe flows through puffs and slugs. *Journal of Fluid Mechanics*, 614:425, 2008.

[38] Masaki Shimizu, Paul Manneville, Yohann Duguet, and Genta Kawahara. Splitting of a turbulent puff in pipe flow. *Fluid Dynamics Research*, 46(6):061403, 2014.

[39] K. Kaneko. Spatiotemporal Intermittency in Coupled Map Lattices. *Progress of Theoretical Physics*, 74(5):1033–1044, 1985.

[40] Hugues Chaté and Paul Manneville. Transition to turbulence via spatio-temporal intermittency. *Physical Review Letters*, 58(2):112–115, 1987.

[41] Y. Pomeau. Front motion, metastability and subcritical bifurcations in hydrodynamics. *Physica D: Nonlinear Phenomena*, 23(1-3):3–11, 1986.

[42] S Bottin and H. Chaté. Statistical analysis of the transition to turbulence in plane Couette flow. *European Physical Journal B*, 6:143–155, 1998.

[43] Paul Manneville. Spatiotemporal perspective on the decay of turbulence in wall-bounded flows. *Physical Review E - Statistical, Nonlinear, and Soft Matter Physics*, 79(2):025301, 2009.

[44] D. Moxey and D. Barkley. Distinct large-scale turbulent-laminar states in transitional pipe flow. *Proceedings of the National Academy of Sciences of the United States of America*, 107(18):8091–8096, 2010.

[45] K. Avila, D. Moxey, A. de Lozar, Marc Avila, D. Barkley, and B. Hof. The Onset of Turbulence in Pipe Flow. *Science*, 333(6039):192–196, 2011.

[46] Dwight Barkley. Simplifying the complexity of pipe flow. *Physical Review E - Statistical, Nonlinear, and Soft Matter Physics*, 84(1):016309, 2011.

[47] Maksim Sipos and Nigel Goldenfeld. Directed percolation describes lifetime and growth of turbulent puffs and slugs. *Physical Review E - Statistical, Nonlinear, and Soft Matter Physics*, 84(3):035304, 2011.

[48] Masaki Sano and Keiichi Tamai. A universal transition to turbulence in channel flow. *Nature Physics*, 12(3):249–253, 2016.

[49] Vasudevan Mukund and Björn Hof. The critical point of the transition to turbulence in pipe flow. *Journal of Fluid Mechanics*, 839:76–94, 2018.

[50] M. Couliou and R. Monchaux. Large-scale flows in transitional plane Couette flow: A key ingredient of the spot growth mechanism. *Physics of Fluids*, 27(3), 2015.

[51] Matthew Chantry, Laurette S. Tuckerman, and Dwight Barkley. Universal Continuous Transition to Turbulence in a Planar Shear Flow. *Journal of Fluid Mechanics*, 824:R1, 2017.

[52] Dwight Barkley, Baofang Song, Vasudevan Mukund, Grégoire Lemoult, Marc Avila, and Björn Hof. The rise of fully turbulent flow. *Nature*, 526(7574):550–553, 2015.

[53] Bruno Eckhardt, Holger Faisst, Armin Schmiegel, and Tobias M. Schneider. Dynamical systems and the transition to turbulence in linearly stable shear flows. *Philosophical Transactions of the Royal Society A: Mathematical, Physical and Engineering Sciences*, 366(1868):1297–1315, 2008.

[54] Siegfried Grossmann. The onset of shear flow turbulence. *Reviews of Modern Physics*, 72(2):603–618, 2000.

[55] P Cvitanovic and B Eckhardt. Periodic orbit expansions for classical smooth flows. *Journal of Physics A: Mathematical and General*, 24(5):L237–L241, 1991.

[56] Björn Hof, Casimir W.H. Van Doorne, Jerry Westerweel, Frans T.M. Nieuwstadt, Holger Faisst, Bruno Eckhardt, Hakan Wedin, Richard R. Kersweli, and Fabian Waleffe. Experimental Observation of Nonlinear Traveling Waves in Turbulent Pipe Flow. *Science*, 305(5690):1594–1598, 2004.

[57] Fabian Waleffe. Exact Coherent Structures in Turbulent Shear Flows. *Turbulence and Interactions*, pages 139–158, 2009.

[58] Fabian Waleffe. On a self-sustaining process in shear flows. *Physics of Fluids*, 9(4):883–900, 1997.

[59] M. Nagata. Three-dimensional finite-amplitude solutions in plane Couette flow: bifurcation from infinity. *Journal of Fluid Mechanics*, 217:519, 1990.

[60] Fabian Waleffe. Homotopy of exact coherent structures in plane shear flows. *Physics of Fluids*, 15(6):1517–1534, 2003.

[61] Fabian Waleffe. Exact coherent structures in channel flow. *Journal of Fluid Mechanics*, 435:93–102, 2001.

[62] R. M. Clever and F. H. Busse. Tertiary and quaternary solutions for plane Couette flow. *Journal of Fluid Mechanics*, 344:137–153, 1997.

[63] D. Viswanath. Recurrent motions within plane Couette turbulence. *Journal of Fluid Mechanics*, 580:339, 2007.

[64] Tobias Kreilos and Bruno Eckhardt. Periodic orbits near onset of chaos in plane Couette flow. *Chaos*, 22(4):047505, 2012.

[65] J. F. Gibson, J. Halcrow, and P. Cvitanović. Visualizing the geometry of state space in plane Couette flow. *Journal of Fluid Mechanics*, 611:107–130, 2008.

[66] J. F. Gibson. Channelflow: A spectral Navier-Stokes simulator in C++, 2014.

[67] Paul Manneville. Coherent structures in transitional plane Couette flow. *IMA Journal of Applied Mathematics*, 77(3):391–398, 2012.

[68] Holger Faisst and Bruno Eckhardt. Traveling Waves in Pipe Flow. *Physical Review Letters*, 91(22):224502, 2003.

[69] H. Wedin and Rich R. Kerswell. Exact coherent structures in pipe flow: travelling wave solutions. *Journal of Fluid Mechanics*, 508:333–371, 2004.

[70] Ozge Ozcakir, Saleh Tanveer, Philip Hall, and Edward A. Overman. Travelling wave states in pipe flow. *Journal of Fluid Mechanics*, 791:284–328, 2016.

[71] R R Kerswell and O R Tutty. Recurrence of travelling waves in transitional pipe flow. *Journal of Fluid Mechanics*, 584:69–102, 2007.

[72] Yohann Duguet, Chris C. T. Pringle, and Rich R. Kerswell. Relative periodic orbits in transitional pipe flow. *Physics of Fluids*, 20(11):114102, 2008.

[73] D Viswanath. The critical layer in pipe flow at high Reynolds number. *Philosophical Transactions of the Royal Society A: Mathematical, Physical and Engineering Sciences*, 367(1888):561–576, 2009.

[74] N. B. Budanur, K. Y. Short, M. Farazmand, A. P. Willis, and P. Cvitanović. Relative periodic orbits form the backbone of turbulent pipe flow. *Journal of Fluid Mechanics*, 833:274–301, 2017.

[75] F. Mellibovsky and Bruno Eckhardt. Takens-Bogdanov bifurcation of travelling-wave solutions in pipe flow. *Journal of Fluid Mechanics*, 670(2011):96–129, 2011.

[76] C Beaume, Gregory P. Chini, Keith Julien, and Edgar Knobloch. Reduced description of exact coherent states in parallel shear flows. *Physical Review E - Statistical, Nonlinear, and Soft Matter Physics*, 91(4):043010, 2015.

[77] J. Halcrow, J. F. Gibson, P. Cvitanović, and D. Viswanath. Heteroclinic connections in plane Couette flow. *Journal of Fluid Mechanics*, 621:365–376, 2009.

[78] N. B. Budanur and B. Hof. Heteroclinic path to spatially localized chaos in pipe flow. *Journal of Fluid Mechanics*, 827:R1, 2017.

[79] Predrag Cvitanović. Recurrent flows: the clockwork behind turbulence. *Journal of Fluid Mechanics*, 726:1–4, 2013.

[80] Predrag Cvitanović, R Artuso, R Mainieri, G Tanner, and G Vattay. *Chaos: Classical and Quantum*. Niels Bohr Institute, Copenhagen, 2016.

[81] Gary J. Chandler and Rich R. Kerswell. Invariant recurrent solutions embedded in a turbulent two-dimensional Kolmogorov flow. *Journal of Fluid Mechanics*, 722:554–595, 2013.

[82] Jue Wang, John Gibson, and Fabian Waleffe. Lower branch coherent states in shear flows: Transition and control. *Physical Review Letters*, 98(20):204501, 2007.

[83] D. Viswanath. The dynamics of transition to turbulence in plane couette flow. In *Mathematics and Computation, a Contemporary View: The Abel Symposium 2006 - Proceedings of the 3rd Abel Symposium*, pages 109–127, Berlin, Heidelberg, 2008. Springer Berlin Heidelberg.

[84] D. Viswanath and P. Cvitanovic. Stable manifolds and the transition to turbulence in pipe flow. *Journal of Fluid Mechanics*, 627:215, 2009.

[85] Joseph D. Skufca, James A. Yorke, and Bruno Eckhardt. Edge of chaos in a parallel shear flow. *Physical Review Letters*, 96(17):174101, 2006.

[86] Tobias M. Schneider, Bruno Eckhardt, and James A. Yorke. Turbulence transition and the edge of chaos in pipe flow. *Physical Review Letters*, 99(3):034502, 2007.

[87] Tobias M. Schneider, John F. Gibson, Maher Lagha, Filippo De Lillo, and Bruno Eckhardt. Laminar-turbulent boundary in plane Couette flow. *Physical Review E - Statistical, Nonlinear, and Soft Matter Physics*, 78(3):037301, 2008.

[88] Tobias M Schneider and Bruno Eckhardt. Edge states intermediate between laminar and turbulent dynamics in pipe flow. *Philosophical transactions. Series A, Mathematical, physical, and engineering sciences*, 367(1888):577–87, 2009.

[89] Chris C. T. Pringle, Ashley P. Willis, and Rich R. Kerswell. Minimal seeds for shear flow turbulence: using nonlinear transient growth to touch the edge of chaos. *Journal of Fluid Mechanics*, 702:415–443, 2012.

[90] Bruno Eckhardt. Transition to turbulence in shear flows. *Physica A: Statistical Mechanics and its Applications*, 504:121–129, 2018.

[91] Jeffrey S. Baggett and Lioyd N. Trefethen. Low-dimensional models of subcritical transition to turbulence. *Physics of Fluids*, 9(4):1043–1053, 1997.

[92] Bruno Eckhardt and A Mersmann. Transition to turbulence in a shear flow. *Physical review. E*, 60(1):509–17, 1999.

[93] Maher Lagha and Paul Manneville. Modeling of plane Couette flow. I. Large scale flow around turbulent spots. *Physics of Fluids*, 19(9):094105, 2007.

[94] Ashley P. Willis and Rich R. Kerswell. Turbulent dynamics of pipe flow captured in a reduced model: Puff relaminarization and localized 'edge' states. *Journal of Fluid Mechanics*, 619:213–233, 2009.

[95] K Seshasayanan and Paul Manneville. Laminar-turbulent patterning in wall-bounded shear flows: a Galerkin model. *Fluid Dynamics Research*, 47(3):035512, 2015.

[96] Korinna T Allhoff and Bruno Eckhardt. Directed percolation model for turbulence transition in shear flows. *Fluid Dynamics Research*, 44(3):031201, 2012.

[97] Hong-Yan Shih, Tsung-Lin Hsieh, and Nigel Goldenfeld. Ecological collapse and the emergence of travelling waves at the onset of shear turbulence. *Nature Physics*, 12(3):245–248, 2016.

[98] D. Barkley. Theoretical perspective on the route to turbulence in a pipe. *Journal of Fluid Mechanics*, 803:P1, 2016.

[99] Yoshiki Kuramoto and T. Yamada. Turbulent State in Chemical Reactions. *Progress of Theoretical Physics*, 56(2):679–681, 1976.

[100] Y. Kuramoto and T. Tsuzuki. Persistent Propagation of Concentration Waves in Dissipative Media Far from Thermal Equilibrium. *Progress of Theoretical Physics*, 55(2):356–369, 1976.

[101] G.I. Sivashinsky. Nonlinear analysis of hydrodynamic instability in laminar flames—I. Derivation of basic equations. *Acta Astronautica*, 4(11-12):1177–1206, 1977.

[102] Scott M. Zoldi and Henry S. Greenside. Spatially localized unstable periodic orbits of a high-dimensional chaotic system. *Physical Review E - Statistical Physics, Plasmas, Fluids, and Related Interdisciplinary Topics*, 57(3):R2511–R2514, 1998.

[103] Boris I. Shraiman. Order, Disorder, and Phase Turbulence. *Physical Review Letters*, 57(3):325–328, 1986.

[104] Erico L. Rempel, Abraham C L Chian, and Rodrigo A. Miranda. Chaotic saddles at the onset of intermittent spatiotemporal chaos. *Physical Review E - Statistical, Nonlinear, and Soft Matter Physics*, 76(5):056217, 2007.

[105] James M. Hyman and Basil Nicolaenko. The Kuramoto-Sivashinsky equation: A bridge between PDE'S and dynamical systems. *Physica D: Nonlinear Phenomena*, 18(1-3):113–126, 1986.

[106] J M Greene and J. S. Kim. The steady states of the Kuramoto-Sivashinsky equation. *Physica D: Nonlinear Phenomena*, 33(1-3):99–120, 1988.

[107] Harry S Brown and Ioannis G Kevrekidis. Modulated Traveling Waves for the Kuramoto-Sivashinskv Equation. *Fields Institute Communications*, 6, 1996.

[108] Daniel Michelson. Radial asymptotically periodic solutions of the Kuramoto-Sivashinsky equation. *Physica D: Nonlinear Phenomena*, 237(3):351–358, 2008.

[109] F. Christiansen, P. Cvitanovic, and V. Putkaradze. Spatiotemporal chaos in terms of unstable recurrent patterns. *Nonlinearity*, 10(1):55–70, 1997.

[110] A. C.-L. Chian, E. L. Rempel, E. E. Macau, R. R. Rosa, and F. Christiansen. High-dimensional interior crisis in the Kuramoto-Sivashinsky equation. *Physical Review E - Statistical Physics, Plasmas, Fluids, and Related Interdisciplinary Topics*, 65(3):035203, 2002.

[111] Erico L. Rempel and Abraham C. L. Chian. High-dimensional chaotic saddles in the Kuramoto-Sivashinsky equation. 2003.

[112] Erico L. Rempel, Abraham C. L. Chian, Elbert E. N. Macau, and Reinaldo R. Rosa. Analysis of chaotic saddles in high-dimensional dynamical systems: The Kuramoto-Sivashinsky equation. *Chaos*, 14(3):545–556, 2004.

[113] Ioannis G. Kevrekidis, Basil Nicolaenko, and James C. Scovel. Back in the Saddle Again: A Computer Assisted Study of the Kuramoto–Sivashinsky Equation. *SIAM Journal on Applied Mathematics*, 50(3):760–790, 1990.

[114] M E Johnson, M S Jolly, and I G Kevrekidis. The Oseberg transition: visualization of global bifurcations for the Kuramoto-Sivashinsky equation. *International Journal of Bifurcation and Chaos*, 11(01):1–18, 2001.

[115] J. Swift and P. C. Hohenberg. Hydrodynamic fluctuations at the convective instability. *Physical Review A*, 15(1):319–328, 1977.

[116] K. R. Elder, J. D. Gunton, and Nigel Goldenfeld. Transition to spatiotemporal chaos in the damped Kuramoto-Sivashinsky equation. *Physical Review E*, 56(2):1631–1634, 1997.

[117] Yuncherl Choi and Jongmin Han. Dynamical bifurcation of the damped Kuramoto–Sivashinsky equation. *Journal of Mathematical Analysis and Applications*, 421(1):383–398, 2015.

[118] Hector Gomez and José París. Numerical simulation of asymptotic states of the damped Kuramoto-Sivashinsky equation. *Physical Review E - Statistical, Nonlinear, and Soft Matter Physics*, 83(4):046702, 2011.

[119] Charles D Brummitt and J C Sprott. A search for the simplest chaotic partial differential equation. *Physics Letters A*, 373:2717–2721, 2009.

[120] Paul Becherer, Alexander N. Morozov, and Wim van Saarloos. Probing a subcritical instability with an amplitude expansion: An exploration of how far one can get. *Physica D: Nonlinear Phenomena*, 238(18):1827–1840, 2009.

[121] Bengt Fornberg. *A practical guide to pseudospectral methods*. Cambridge Univ. Press, 1996.

[122] Claudio. Canuto, M. Yousuff. Hussaini, Alfio. Quarteroni, and Thomas A. Zang. *Spectral Methods in Fluid Dynamics*. Springer Berlin Heidelberg, 1988.

[123] Matteo Frigo. A Fast Fourier Transform Compiler. Technical report, 1999.

[124] L P Kadanoff and C Tang. Escape from strange repellers. *Proceedings of the National Academy of Sciences of the United States of America*, 81(4):1276–1279, 1984.

[125] John W. Harris and Horst Stöcker. *Handbook of mathematics and computational science*. Springer, 1998.

[126] Paul Ritter, Fernando Mellibovsky, and Marc Avila. Emergence of spatio-temporal dynamics from exact coherent solutions in pipe flow. *New Journal of Physics*, 18(8):083031, 2016.

[127] J. E. Dennis, Robert B. Schnabel, John E Dennis Jr., and Robert B. Schnabel. *Numerical methods for unconstrained optimization and nonlinear equations*. SIAM, 1983.

[128] Jorge Nocedal and Stephen J. Wright. Line Search Methods. In *Numerical optimization*, Springer Series in Operations Research and Financial Engineering, pages 30–65. Springer New York, 2006.

[129] Eugene L. Allgower and Kurt Georg. *Introduction to Numerical Continuation Methods*. SIAM, 2003.

[130] Dwight Barkley and Laurette S. Tuckerman. Mean flow of turbulent-laminar patterns in plane Couette flow. *Journal of Fluid Mechanics*, 576:109–137, 2007.

[131] Liang Shi, Marc Avila, and Bjorn Hof. Scale invariance at the onset of turbulence in couette flow. *Physical Review Letters*, 110(20), 2013.

[132] Roberto Livi and Paolo Politi. *Nonequilibrium Statistical Physics. A Modern Perspective*. 2017.

[133] Haye Hinrichsen. Observation of directed percolation—a class of nonequilibrium phase transitions. *Physics*, 2:96, 2009.

[134] Dietrich. Stauffer and Ammon. Aharony. *Introduction to Percolation Theory*, volume 1. Taylor & Francis Group, 1994.

[135] Iwan Jensen. Low-density series expansions for directed percolation: III. Some two-dimensional lattices. *Journal of Physics A: Mathematical and General*, 37(27):6899–6915, 2004.

[136] Annick. Lesne and Michel Lagues. *Scale Invariance: from phase transitions ot turbulence*. Springer, 2012.

[137] Malte Henkel, Haye Hinrichsen, and Sven Lübeck. *Non-equilibrium phase transitions. Volume 1: Absorbing phase transitions*. Springer, 2008.

[138] Eric Jones, Travis Oliphant, Pearu Peterson, and Others. SciPy: Open source scientific tools for Python, 2001.

[139] Mary Ann Branch, Thomas F. Coleman, and Yuying Li. A Subspace, Interior, and Conjugate Gradient Method for Large-Scale Bound-Constrained Minimization Problems. *SIAM Journal on Scientific Computing*, 21(1):1–23, 1999.

[140] Somendra M Bhattacharjee and Flavio Seno. A measure of data collapse for scaling. *Journal of Physics A: Mathematical and General*, 34(33):6375–6380, 2001.

[141] Iwan Jensen. Low-density series expansions for directed percolation: I. A new efficient algorithm with applications to the square lattice. *Journal of Physics A: Mathematical and General*, 32(28):5233–5249, 1999.

[142] Kazumasa A. Takeuchi, Masafumi Kuroda, Hugues Chaté, and Masaki Sano. Experimental realization of directed percolation criticality in turbulent liquid crystals. *Physical Review E - Statistical, Nonlinear, and Soft Matter Physics*, 80(5):051116, 2009.

[143] Aaron Clauset, Cosma Rohilla Shalizi, and M. E. J. Newman. Power-Law Distributions in Empirical Data. *SIAM Review*, 51(4):661–703, 2009.

[144] Jeff Alstott, Ed Bullmore, and Dietmar Plenz. powerlaw: A Python Package for Analysis of Heavy-Tailed Distributions. *PLoS ONE*, 9(1):e85777, 2014.